Adhesion of thin structures : frictional peeling and adhesive shells

Suomi Ponce Heredia

To cite this version:

Suomi Ponce Heredia. Adhesion of thin structures : frictional peeling and adhesive shells. Physics [physics]. Université Pierre et Marie Curie - Paris VI, 2015. English. NNT : 2015PA066550 . tel-01327267

HAL Id: tel-01327267
https://theses.hal.science/tel-01327267

Submitted on 6 Jun 2016

THÈSE DE DOCTORAT
DE L'UNIVERSITÉ PIERRE ET MARIE CURIE

Spécialité : Physique

École doctorale : «Physique en Île-de-France »

réalisée

Au Laboratoire de Physique et Mécanique des Milieux Hétérogènes

présentée par

Suomi PONCE HEREDIA

pour obtenir le grade de :

DOCTEUR DE L'UNIVERSITÉ PIERRE ET MARIE CURIE

Sujet de la thèse :

Adhesion of thin structures

Frictional peeling and adhesive shells

soutenue le 30 Novembre, 2015

devant le jury composé de :

M.	Etienne Barthel	Examinateur
M.	José Bico	Directeur de thèse
M.	Axel Buguin	Examinateur
Mme.	Liliane Léger	Rapporteure
M.	Benoît Roman	Invité
M.	Loïc Vanel	Rapporteur

Suomi PONCE HEREDIA **30 Novembre, 2015**

Sujet : Adhesion of thin structures

Frictional peeling and adhesive shells

Résumé : Dans cette thèse, nous nous intéressons à l'adhésion d'élastomères sur des substrats rigides (interactions de van der Waals). Nous revisitons ainsi, en nous appuyant sur une approche expérimentale, deux situations classiques qui permettent la mesure de l'énergie d'adhésion. Dans une première partie dédiée à l'étude du pelage, nous montrons que le frottement peut modifier le processus de détachement d'une bande d'élastomère. Ceci est tout d'abord mis en évidence lors du pelage parallèlement à l'interface, où nous montrons qu'il conduit à la progression d'une zone de frottement jusqu'au détachement de la bande pour une force proportionnelle à l'aire de contact. Nous généralisons par la suite nos résultats au pelage selon un angle quelconque. En particulier, nous montrons comment la dissipation par frottement peut augmenter de façon significative la force de pelage pour des angles faibles. Dans une deuxième partie, nous nous tournons vers la mesure d'adhésion dans une géométrie JKR, c'est à dire lors de l'indentation d'une sphère élastique adhésive avec un substrat rigide. Nous utilisons des coques élastiques dont la réponse mécanique est beaucoup plus souple bien que plus complexe. Nous montrons qu'il est néanmoins possible d'obtenir une mesure de l'adhésion par une méthode très simple et très robuste, puisqu'elle ne suppose pas de connaissance a priori de la mécanique du système. Nous espérons que cette technique permettra dans le futur d'accéder à des énergies d'adhésion très faibles ou mettant en jeu des tissus biologiques particulièrement mous.

Subject : Adhesion of thin structures

Frictional peeling and adhesive shells

Résumé : In this thesis, we are devoted to study the adhesion of elastomers to rigid substrates through van der Waals interactions. We review, from an experimental point of view, two classical methods to measure the adhesion energy. A first part is dedicated to the study of the peeling system, we show that friction can modify the detachment process of an elastomer strip. This is firstly observed in the lap-test configuration, where a sliding front propagates on the interface up until the end of the strip, for a pulling force proportional to the initial contact area. We generalize this results for the finite peeling angle case. In particular, we show how the friction dissipation significantly increases for small peeling angles. In the second part, we study the adhesion measure in the JKR geometry, i.e. for the indentation of an adhesive elastic sphere into a rigid plate. We use elastic thin shells, which elastic response is much softer, as well it is much more complex. However, it is possible to measure the adhesion energy through a very simple and robust method with no need of much details of the mechanical response of the system. We hope this technique will allow to measure the effect of very weak and sensitive adhesive systems such us biological tissues which are particularly soft.

Contents

1. Introduction

The interaction of thin films with liquid interfaces, has been a crucial topic of interest in the PMMH laboratory in recent years. The main focus was to study the possibly large macroscopic deformation of soft solids due to interfacial forces. One example is the capillarity rise of a liquid on a brush of thin flexible fibers, which leads to the formation of self-organized bundles (fig. 1.1a). This type of interaction is particularly relevant at small scales as capillary forces become dominant over elastic resistance. Disastrous deflection of micro-structures are frequently observed in micro-fabrication processes involving lithography. However, domesticated capillary forces can also be viewed as a useful tool to fold planar templates into a 3D desired shape [1, 2] (in fig. 1.1b, a soap bubble performs origami on a flower-shaped thin sheet). And its inverted version, where a wet sphere is wrapped with an elastic sheet (fig. 1.1c) [3]. More recently, the group became interested also in solid adhesion: the tearing and peeling of an adhesive tape from a rigid substrate (fig. 1.1d) [4], or the formation of blisters [5] on a thin film deposited on a very soft substrate (fig. 1.1e).

From an energy point of view, capillary and adhesion or even fracture energies may sound similar. They indeed correspond to the energy required to create an interface. Are these three

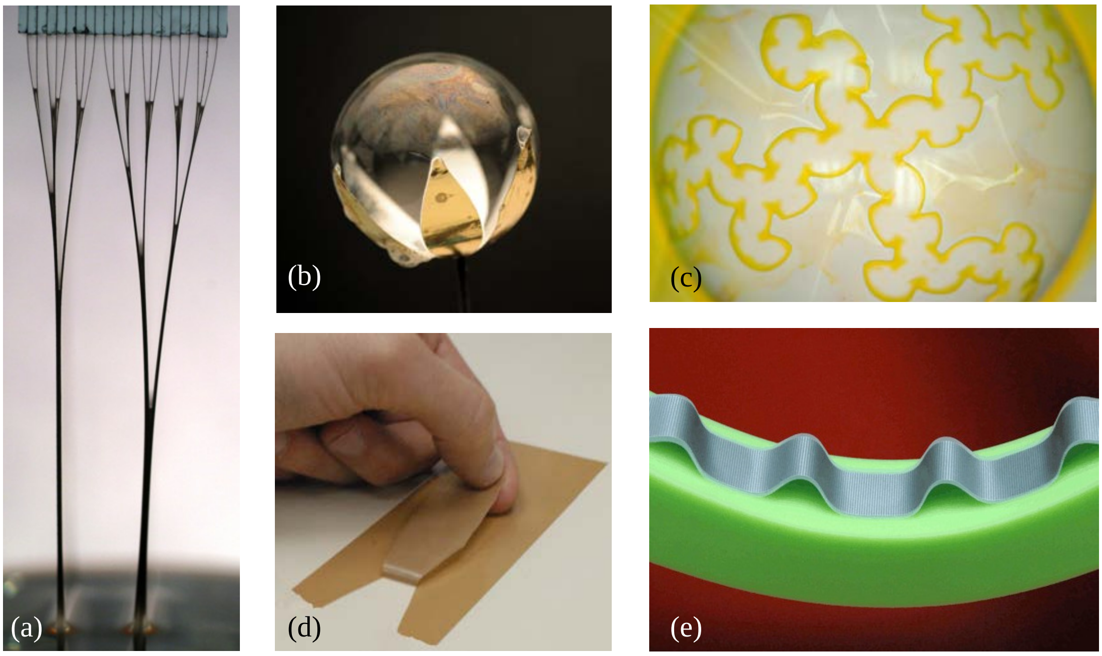

Figure 1.1.: *Examples of elasto-adhesive interaction studied in the group: (a) bundling of wet brushes, (b) capillary induced folding of a thin sheet, (c) wrapping of an adhesive sphere, (d) tearing of an adhesive tape, (e) formation of delamination blisters on a soft substrate.*

concepts really equivalent? This PhD thesis is dedicated to the *study of dry (Van der Waals) adhesion* between a soft elastomer and a rigid substrate. This situation is interesting as it lays between capillarity and standard fracture mechanics. Van der Waals adhesion is indeed reversible as capillary bridges, but it involves solids as in classical fracture. One aim of our work is thus to explore these intermediate situations while keeping an eye on the liquid and solid limits as references.

Figure 1.2.: *Examples of van der Waals adhesion/friction: (a) Amazing adhesive properties of gecko feet promoted by the adhesion of millions of compliant setae (images credits Guardian Liberty Voice and Kellar Autumn), (b) Protective tapes or decorating gels sticker (Images credits Aliexpress.com, lifehacker.com, forum.cockos.com).*

In terms of applications, van der Waals adhesion provides the adhesion of protective layers commonly used to protect the screens our electronic equipment or of repositionable decorations for windows (figure 1.2b). It has also been recently found that the amazing adhesion of geckos lizards in any type of substrates relies on van der Waals interactions [6]. The tiny setae that cover their feet are indeed compliant enough to adapt their shape to the local roughness of the substrate, which provides a good contact area (figure 1.2a). This discovery triggered a large scientific activity with the aim of mimicking the remarkable universal and reversible adhesion of gecko feet. Without pretending to solve the technical issues encountered in the different attempts to develop biomimetic adhesives, our work is in the line of this blooming activity. More particularly, we will focus on two complementary configurations used to probe adhesion: peeling and JKR indentations tests (Fig. 1.3).

The peeling test

Adhesive forces allows geckos to stand upside down on ceilings. From an amplitude point of view, capillary forces could play the same role. However geckos can also climb along vertical walls without sliding down. In addition to adhesion, friction is thus involved, which would not be the case with wet adhesion (with a non yield stress liquid). Beyond geckos locomotion, friction is more generally crucial when peeling is involved. Indeed when we want to remove the thin skin laying on the milk from the morning breakfast, the peeling direction is always normal to the liquid surface. Invariably, any attempt to peel the skin in another direction will indeed lead to a displacement of the whole layer until the peeling angle gets back to 90°. In contrast, we can peel off an adhesive tape from a surface with any peeling angle: friction prevents the tape from sliding away. Although friction obviously plays an important role in the adhesion of solid, it is not included in classical descriptions of peeling [7, 8]. In standard mechanics some effect of friction is nevertheless included in the notion of "mode mixity" where a first mode corresponds to cleavage (which is usually interpreted as "adhesion") and a second mode to shear. This shear mode only applies in the process zone, a region located in the vicinity of the crack tip ("where we hide the messy stuff under the rug", quoting Jay Finneberg). However, macroscopic sliding zones have been observed experimentally during peeling tests in the case of soft solids [9, 10, 11]. Should frictional dissipation be included in the description of peeling? Would friction modify the expression of the peeling force? Can we probe friction from a simple peeling test?

In the first part of this thesis we will focus on the peeling of an elastomeric strip from smooth plate. In chapter 3, we describe the particular and maybe singular case of peeling at zero degrees (figure 1.3a), where friction is dominant. We then continue in chapter 4 by considering the general case of finite peeling angle, with an emphasis on very small angles.

JKR indentation test

This classical test consists in extracting the adhesion energy from a measure of the force resulting from the indentation of an elastic sphere on a rigid plate. This method relies on a theoretical description of the phenomenon, assuming small strain (linear elasticity) and small displacements. This standard technique is difficult to apply in the case of weak adhesion forces or relatively hard materials since the tiny strains involved are difficult to monitor. In chapter 5 we consider the indentation of a thin elastic shell (Fig. 1.3b). Such structure is indeed more compliant than a plain sphere and may experience stronger deformations. Nevertheless the mechanical response of shells can be very complex, which brings a new difficulty. Recent approaches have been proposed to describe the non-linear mechanical properties of ping-pong balls [12]. Can we include adhesion in these concepts and formulate a generalized version of JKR indentation test? Will we be able to infer adhesion energies from such indentation tests?

In this thesis, our approach will be mostly based on experiments at macroscopic scale involving dry adhesion (Van der Waals) of elastomers on a rigid substrate (a glass plate). The elastomers will be considered as perfectly elastic, homogeneous and isotropic. Most of the time, we will use a versatile polyvynylsiloxane (PVS) polymer, which is quickly prepared, and easy to cast in any desired shape. As a general approach, we will compare our experimental results to analytical theories based on simplifying arguments, and scaling arguments, rather than comprehensive numerics or advanced theoretical developments.
Before presenting our research work, we first provide a brief overview of contact and adhesion mechanics in chapter 2.

Figure 1.3.: *Configurations investigated in the present thesis: (a) peeling of an elastomeric tape adhering on a smooth tape, (b) punch test with a highly compliant shell.*

2. A quick overview on the contact mechanics of elastic bodies

In this thesis we propose to study the mechanical and adhesive properties of thin elastic structures of a silicone-based elastomer, using the contact mechanics approach. In general, these contact mechanics problems can be treated from an energetic point of view, by considering three principal ingredients: the work done by an external force to peel or indent the elastomer, its elastic energy, and its surface energy properties.

In this chapter we outline the basic ideas of continuum contact mechanics. We start with a small summary of elasticity to describe the mechanics of soft elastomeric materials. We then introduce the concepts of surface energy, work of adhesion and energy release rate, in order to calculate interfacial properties of contact bodies. We apply these concepts when reviewing the two most commonly used adhesive tests: the peel the indentation test. We finish by suggesting the possible influence of friction during adhesive crack process in the case of smooth elastomeric material. As we will show, this phenomenon can appears in particular configurations of peeling and indentation test.

2.1. Fundamental concepts of the theory of elasticity

Theory of elasticity establishes a description of solid bodies as continuum media [13]. Solid materials can be deformed without loosing the cohesion of the bulk material. Due to these cohesive internal forces, external forces have to be necessarily applied to deform a solid.

Solids can be characterized by a constitutive law, i.e. the relation between applied stresses and the strains they induce. These deformations can be irreversible or not. When deformations are reversible, we say the solid is defined as elastic and plastic on the opposite case. In practical situations, solids can behave elastically or plastically depending on the amount of deformation applied. They can also be able to support very large deformations in a completely reversible way, before breaking, phenomenon called hyperelasticity. Solids can also be viscoelastic when their mechanical response to a external force depends on time.

In this thesis we treat with hyperelastic elastomers at room temperature, which is enough above their glass transition temperature. In this regime they are rubbery. In the following we will limit the discussion to a linear response theory of elasticity, meaning that the material shows a linear linking in stress-strain relation (constitutive law) to small deformations. Then, we briefly review their nonlinear response considering their hyperelastic behavior.

2.1.1. Strain, stress and elastic modulus

To simplify our discussion, we consider the example of a strip of initial length L_o submitted to a tensile test (Fig. 2.1). When deformed, there is a tensile strain in the strip. The strain is a measure of the deformation of a solid material. It is the local spatial variation of the relative displacements of the material points in a deformed body, when an external force is applied. In the simple case of an unidirectional tensile test, the strain can be easily defined by:

$$\varepsilon \sim \frac{\Delta L}{L_o}\,, \tag{2.1.1}$$

where L_o is the initial length of the elastomer at rest. When the elastic strip is deformed, a certain stress develops as a response of the body, that wants to recover its equilibrium state. In order to maintain the deformation, an external force has to be applied that equilibrates the internal stresses. In the linear response regime and for an isotropic homogeneous material, this small tensile stress (a force per unit area of cross section) reads:

$$\sigma = E\varepsilon \,, \tag{2.1.2}$$

where the coefficient E linking stresses and strains is the elastic tensile/compresive modulus or Young's modulus of the material.

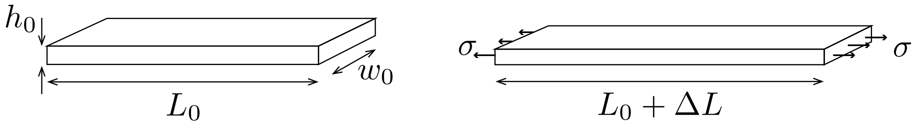

Figure 2.1.: *Basic streching test: a uniform extension load σ is applied to a strip of initial length L_0, which results an increase of it length by ΔL. Within the limits of linear elasticity, the strain $\varepsilon = \Delta L / L_0$ follows Hookes law: $\sigma = E\varepsilon$.*

Another important type of deformation for our work is shear. This is for instance the case if the elastic strip we have previously considered is now sandwiched between to parallel rigid plates and a relative displacement parallel to the strip $\Delta L_{||}$ is applied to the plates (Fig. 2.2). This displacement results in a shear strain $\varepsilon_{xz} = \Delta L_{||}/h$. Following Hookes law the corresponding shear stress τ is proportional to the strain:

$$\tau = \mu\varepsilon_{xz}, \tag{2.1.3}$$

where μ is the shear modulus.
Both Young and shear moduli are proportional:

$$E = 2(1+\nu)\mu,$$

where ν is Poisson coefficient that accounts for the compressibility of the material. However, elastomers can be considered as incompressible, which corresponds to $\nu = 0.5$. In this case, we obtain $E = 3\mu$.

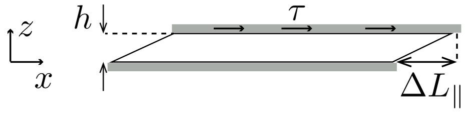

Figure 2.2.: *Basic shear test: and elastic layer is sandwiched between to parallel plates. A relative displacement parallel the strip $\Delta L_{||}$ to is applied to the plates, which results in a shear strain $\varepsilon_{xz} = \Delta L_{||}/h$. Following Hookes law the corresponding shear stress is given by $\tau = \mu\varepsilon_{xz}$, where μ is the shear modulus of the material.*

2.1.2. Elastic energy

In fracture and adhesion mechanics it is often useful to discuss in terms of energies. For instance, Griffith criterion for fracture states that a crack shall propagate if the cost in fracture energy is compensated by the release of equivalent elastic energy (see section 2.2.3). We present here the elastic energies stored as a beam is stretched and bent, respectively.

Stretching

In general terms, the elastic energy per unit volume stored in an elastic material is given by $\sigma\varepsilon$. Using Hooke's law $\sigma = E\varepsilon$ we immediately obtain the elastic energy stored in the stretched strip sketched in Fig. 2.1:

$$\mathscr{E}_{stretching} \sim \frac{1}{2} E h_o L_o w_o \varepsilon^2,$$

with $\varepsilon = \Delta L / L_o$.

Bending

When a curvature $1/R$ is applied to a slender beam, the inner side of the beam is compressed while the outer one is stretched (Fig. 2.7). Deriving the typical strain is straightforward. The length of the outer face is for instance given by $\alpha(R + h/2)$ while the center line remains $L = \alpha R$ (we assume $h \ll R$). The relative increase in length is thus $\varepsilon \sim h/R$. If we integrate the corresponding stretching energy over the whole beam, we obtain the global bending energy for the beam:

$$\mathscr{E}_{bending} \sim \frac{Eh^3}{R^2} wL$$

In reality, the bending stiffness depends also on the Poisson ration ν. A more comprehensive calculation gives [13]:

$$\mathscr{E}_{bending} \sim \frac{1}{2} \frac{Eh^3}{12(1-\nu^2)} \frac{wL}{R^2}$$

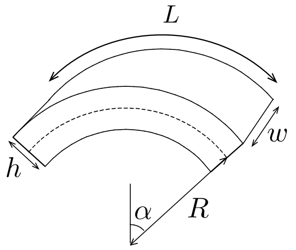

Figure 2.3.: *Bending of a beam to a curvature $1/R$: the inner side is compressed while the outer one is stretched. The typical strain is $\varepsilon \sim h/R$.*

2.2. Some concepts on contact mechanics

In this section we quickly review the different aspects of contact mechanics of soft materials with an emphasis on the elastic and adhesive properties of slender bodies. We overview some fundamental concepts of adhesion and present two standard methods to measure to measure adhesion energy: the peeling and spherical punch tests.A comprehensive review of intermolecular and surface forces and surface energy is beyond the scope of this chapter and only a brief overview is given here.

2.2.1. Surface and intermolecular interactions: van der Waals forces.

The types of forces operating between two surfaces depend on the nature of the interacting surfaces and the medium separating them. Intermolecular and surface forces can be attractive or repulsive and their range of action and magnitude can be very different. During this thesis we will assume that the interactions between our polymers and rigid surfaces are essentially determined by van der Waals interactions (vdW).
The vdW forces originate from interactions between electric dipole moments of the molecules. They exist between any pair of molecules or surfaces and can be attractive or repulsive. They are nevertheless always attractive between similar molecules. There are three major contributions to these forces [14, 15]: (*i*) Keesom interaction: a force between two permanent dipoles, (*ii*) Debye interaction: a force between a permanent dipole and a corresponding induced dipole, and (*iii*) London dispersion forces: a force between two instantly induced dipoles. The three contributions lead to the same expression of the vdW interaction energy between two molecules:

$$\mathscr{E}_{vdW} = \frac{C}{r^6} , \tag{2.2.1}$$

and its corresponding force is $F_{vdW} = -6C/r^7$. Here r is the separation distance between both surfaces or molecules and C is a constant depending on the geometry and optical properties of the interacting bodies.

Other surface and intermolecular interactions can also contribute in the understanding of the adhesive phenomena between surfaces: electrostatic (Coulomb, ionic, double layer), steric and bridging forces, hydrophobic, solvation, hydrogen bonding, etc.. For a more detailed discussion see for example [16, 17]. Van der Waals interactions, and more generally, intermolecular forces dictate surface energies, a concept that we will review in the following.

2.2.2. Surface energy and the thermodynamic work of adhesion

The thermodynamic (or Dupré) work of adhesion is an intrinsic interfacial property of any material, produced by van der Waals and other non-covalent interactions at the surface of a solid and the interface between contact bodies [18]. The work of adhesion corresponds to the work needed to separate completely the surfaces in contact and is given by:

$$w_{adh} = \sigma_1 + \sigma_2 - \sigma_{12} , \tag{2.2.2}$$

where σ_1 and σ_2 are the surface energy (also known as surface tension) of each body, and σ_{12} corresponds to the interfacial energy between them. The surface energy can be defined as the energy required to increase the surface area of medium by unit area. Thus, it represents the excess energy that the molecules on the surface possess compared to molecules in the bulk of a material. For identical materials $\sigma_1 = \sigma_2 = \sigma$ and then $w_{adh} = 2\sigma$ is called the work of cohesion.

The term *surface energy* is mostly used for solids, and it has the unit of energy per unit area (J/m^2). Conversely, the term surface tension is usually used for liquids and is measured in units of force per unit length (N/m). However, the two terms are dimensionally and numerically equivalent. For surfaces between which attractive forces can be accounted by van der Waals forces, the surface energy can be approximated by [16]:

$$\sigma \approx \frac{A}{24\pi(r/2.5)^2}\,, \tag{2.2.3}$$

where r is the interatomic or intermolecular center-to-center distance ($r/2.5 \sim 0.165$ nm is commonly used) and A is the Hamaker constant.
In the case of adhesive fracture process, the work of adhesion balances a mechanical quantity, the energy release rate G, for an ideal reversible process in a thermodynamic equilibrium.

2.2.3. Energy release rate G

The energy release rate G is a mechanical concept that comes from the theory of fracture. It is defined as the energy per unit area available to propagate a crack. When the energy release rate reaches a critical value G_c, it is possible to propagate a fracture, which is known as Griffith's criterion [19]. The critical energy release rate is the the quantity that compensates the dissipation of the fracture process. When G is lower than G_c, an beginning crack cannot propagate.
Cracks can propagate in the core of a single material as well as on the interface of dissimilar materials. We focus on structures composed by two different materials brought into contact. We can consider that separating both structures is analogous to consider that a crack propagating along the interface.

This concept was first applied into adhesion physics by Johnson, Kendall and Roberts [20] by considering that two surfaces of elastic materials that are in contact will be separated when the energy release rate is equal to the work of adhesion of the materials. In that case, G is given by an energetic balance considering the work provided by the pulling force and the elastic energy stored by deforming the bodies.
As noted before, in order to separate to contact bodies the energy release rate G must be equal to the work of adhesion w_{adh} for an ideal reversible equilibrium process. However, G depends in practice on various dissipation processes and then it largely exceeds the Dupré work of adhesion: $G = w_{adh} + w_{diss}$. This energy loss may be due to an interfacial process, associated with van der Waals forces or, in the case of soft polymers, with the rupture of interfacial bonds and chain pull-out, or to a bulk process, associated with the viscoelasticity of the material [21, 22, 23, 24]. All this factors should be taken into account by considering dynamical processes.

During contact dynamics, it is difficult to distinguish between the different contribution of both, interfacial and bulk energy looses of G. However, this amount of energy depends on the velocity of solicitation, i.e. if we detach two surfaces at low velocity or at high velocity, the energetic cost is not the same. We have all experienced that pulling out a scotch tape requires more efforts at high speeds than at lower speeds [25, 26]. To quantify this phenomena, some studies have used an empirical formalism developed by Gent and Shultz borrowed from rheology [27, 28]. In this formalism both contributions to energetic looses can be decomposed into:

$$G(v,T) = G_0(1+\Phi(v)), \tag{2.2.4}$$

where $\Phi(v)$ is called the dissipative function of the material and G_0 is the interfacial strength of the surface, i.e. the value of G at vanishing crack speed.
Throughout our work we will refer to *adhesion energy* γ as the value for which G reaches an stationary value $\gamma = G(\mathrm{v} \to 0) = G_0$. Note that in this case and at equilibrium during a reversible process (a quasi-static loading and unloading, for example) we then get: $\gamma = G_0 = w_{adh}$.

In the following sections we will describe two important tests commonly used to measure the work of adhesion in soft materials: the peeling test and the semi-spherical punch test, analyzed from the JKR point of view.

2.3. Contact mechanics of an elastic strip peeled from a rigid plate.

2.3.1. Inextensible strip: force divergence

About seventy years ago, Rivlin [29] proposed a method to measure the adhesion strength of paint over a substrate. His pioneering work, opened a new road to understanding the adhesion as a mechanical process and not only as an intermolecular interaction. He proposed probing a 90° peeling test on a flexible but non-stretchable material adhering on a rigid substrate. In this scenario, the surface energy will be completely furnished by the work done by the pulling force applied.

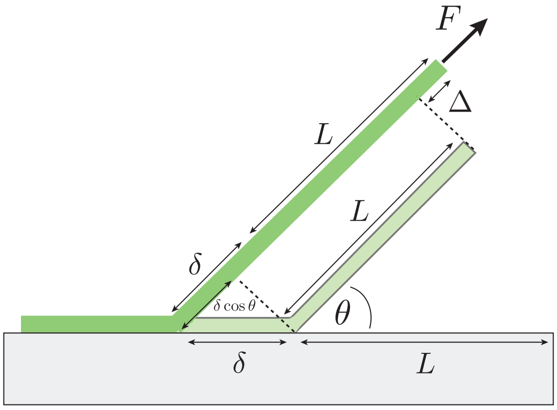

Figure 2.4.: *Sketch of the peeling process of a non-stretchable strip with no bending rigidity (in green) from a rigid substrate (in gray). The pulling force F works along a distance Δ.*

We first consider the case of an inextensible strip with no bending rigidity, adhering on a rigid substrate (figure 2.4). The adhering strip has a thickness h and a width w_o. A pulling force F is exerted at one end of the strip with an imposed direction θ If the crack advances along a distance δ, the detached part of the strip increases by a distance δ as well, since the strip is inextensible. We are interested in the work provided by the operator. The displacement in the direction of the pulling force is given by $\delta - \delta\cos\theta$ and the corresponding work can expressed as:

$$F\delta(1-\cos\theta)$$

On the other hand, the cost in surface energy is $\gamma w_0 \delta$. As a consequence, the steady peeling force is given by:

$$F = \frac{\gamma w_o}{(1-\cos\theta)}, \tag{2.3.1}$$

This relation is widely used, in the academy as well as in the industry, to estimate adhesion energies. However it predicts a non-physical divergence of the force as the peeling angle vanishes:

$$F_{\theta \to 0} \approx \frac{\gamma w_o}{\theta^2} \tag{2.3.2}$$

Although standard tests used to probe adhesive tapes are thus usually conducted at large peeling angles (usually 90° or 180°), assuming that the tapes are inextensible may not be valid for soft materials. In any case, the finite stretchability of the strip has to be taken into account for low peeling angles. We introduce this additional ingredient in the following section.

2.3.2. Extensible strip: regularization

In order to regularize this divergence on the peeling force at low angles, in 1975 Kendall [8] proposed to include the finite stretching rigidity of the elastic strip.

Now, we consider that the strip is elastic with a Young modulus E and, as before, it has a thickness h and width w_o. In this case, the work done by the force will compensate both the surface energy and the variation of elastic energy due to stretching the strip. We limit analysis to linear elasticity. In other words, we assume the strain ε to be small enough to neglect non-linear hyperelastic effects. It is thus proportional to the pulling force: $\varepsilon = F/Ehw_0$.

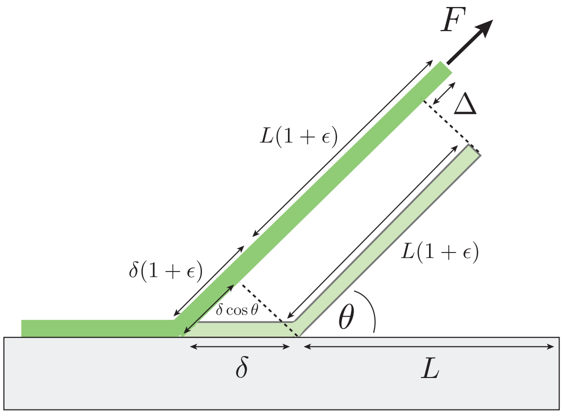

Figure 2.5.: *Sketch of the peeling process of a stretchable strip with non bending rigidity (in green) from a rigid substrate (in gray). The work $F\Delta$ provided by the operator not only compensates for adhesion energy but part of it is stored in the strip as stretching energy.*

Since the stripe is stretched with a strain ε, the displacement of the pulling force in the direction θ is now $\delta(1+\varepsilon) - \delta\cos\theta$. The work provided be the operator is thus:

$$F\delta(1+\varepsilon-\cos\theta)$$

The cost in surface energy remains:

$$\gamma w_0 \delta$$

However, the portion of the strip of initial length δ is stretched during the process. As a consequence, some elastic energy is stored in the stripe. This additional term is given by:

$$\frac{1}{2}Ehw_0\delta\varepsilon^2$$

In a steady propagation the work balances the sum of adhesion and stretching energies, which leads to:

$$F(1-\cos\theta)+\frac{1}{2}\frac{F^2}{Ehw_o}=\gamma w_o \tag{2.3.3}$$

Contrary to the simplified relation, this expression does not diverge for low angles. The force is indeed expected to reach a plateau value:

$$F_K=\sqrt{2Eh\gamma}w_o$$

In the opposite limit of high peeling angles, we recover the previous relation (Eq. 2.3.2). More quantitatively, we expect this large angle limit to be valid for:

$$1-\cos\theta \ll \sqrt{\frac{\gamma}{2Eh}}$$

We report in figure 2.6, the data obtained by Kendall with a strip of ethylene-propylene rubber of Young modulus of 1.2 MPa and a thickness of 0.75 mm. We have superposed to the graph both asymptotic limits obtained : the plateau F_K at low angles and the simplified Rivlin relation for high angles. The value of $\gamma = 5\,\text{N/m}$ used in these relations was measured with a standard 90° peel test. In this particular exemple, the crossover between both regimes occurs around 18°.

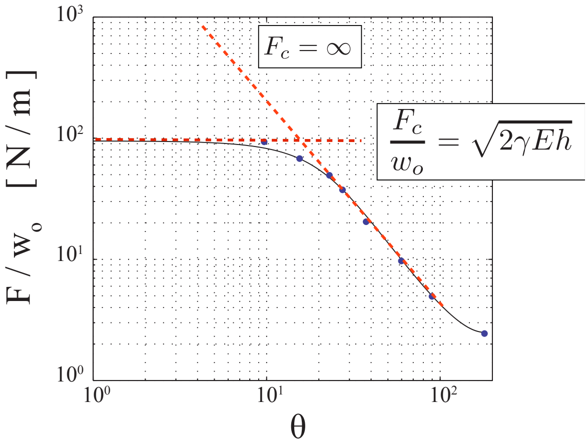

Figure 2.6.: *(●) Kendall's data points, (-) theoretical prediction and red pointed lines are references to the asymptotic behaviors for large and small angles.*

Bending energy and curvature on the strip

In the previous discussion we have disregarded the finite bending stiffness of the strip. However, the transition between the adhered and the detached parts of the strip is not as sharp as in the schematic view we presented. Bending the strip requires an additional energy which results into the finite curvature observed in actual experiments (Fig. 2.7).

Following recent works from the group, the typical radius of curvature of the strip is given by the "elasto-capillary" length scale [30]:

$$R\sim\sqrt{\frac{Eh^3}{\gamma}}$$

Our previous derivations are however still valid in the case of steady propagation since the additional bending energy remains constant. Considering bending can nevertheless be important in the estimation of the adhesion energy from an actual experiment. We discuss this effect in more details in chapter 4.2.4.

In the next section, we review the theory of one of the most popular test to characterize the adhesion of materials: the spherical punch test analyzed under the JKR perspective. Unlike the peeling test, JKR method allows to reduce significantly viscoelastic energy losses due to large deformations and the difficulty to carry peel experiments at low velocities.

2.4. Contact mechanics of an elastic sphere and a rigid plate.

In this section, we are interested in the study of the contact mechanics of an elastic sphere of radius R indented on a rigid plate. As shown in figure 2.8(a), the indentation displacement δ is perpendicular to the rigid plate. The normal loading force F can be compressive or tensile. Indenting the sphere results in a circular contact zone of radius a.In typical experiments, δ is imposed during load and unload processes, and F and a are measured. Some experimental realizations are depicted in Fig. 2.8(b)

In the following section, we will review the classical results for adhesive and non-adhesive contact mechanics for this configuration.

2.4.1. Non adhesive contact: Hertz model

During his Christmas vacations of 1881 H. Hertz developed his famous contact theory for two elastic spheres [31, 32]. His result can be easily extended to the spherical punch configuration described in the above section considering one sphere to be infinitely large and rigid (a plane). The assumptions of this contact theory are:

i) materials in contact are isotropic and elastically linear,

ii) the contact bodies are smooth and locally spherical,

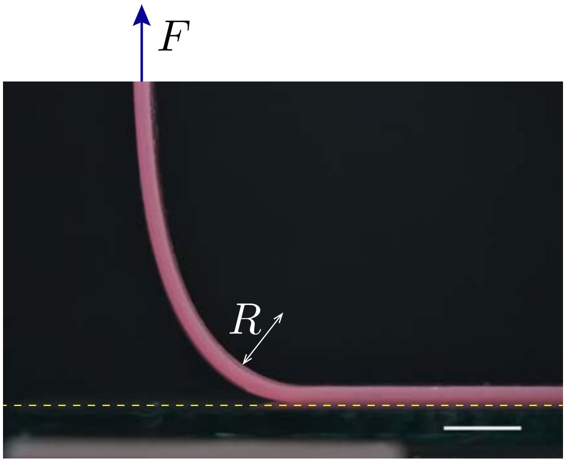

Figure 2.7.: *Peeling at 90° of strip of silicone rubber from a glass plate (scale bar 1 cm). Due to the finite bending stiffness of the strip, the connection between the adhered and detached parts does not make a sharp angle but displays a finite curvature.*

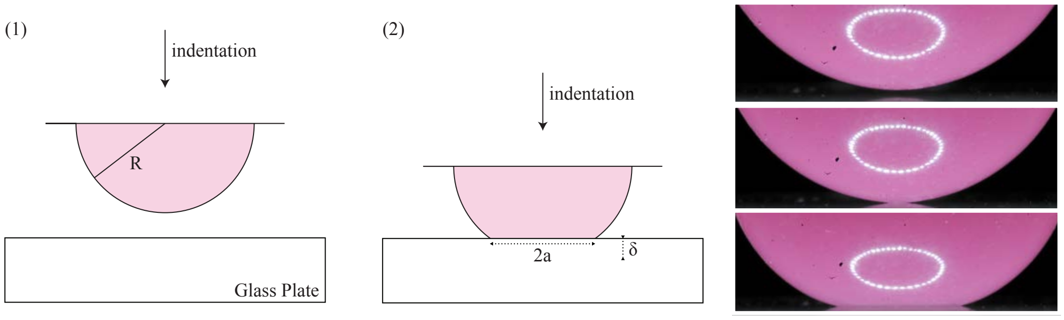

(a) Sketches before (1) and after (2) contact

(b) Experimental images

Figure 2.8.: *Spherical punch indented on a rigid plate. (a) Skteches. (b) Experiments increasing* δ *from top to bottom: before contact, just in contact and advanced contact.*

iii) the contact radii are smaller than the size of the bodies, i.e. $a << R$,
iv) only normal forces are transmitted between bodies, i.e. shear stresses are neglected,
v) frictional and adhesive properties are totally neglected.

The final expressions relating the indentation force and displacement with the contact radius are the following:

$$F_H(a) = \frac{4E^*}{3R} a^3 \ , \tag{2.4.1}$$

$$\delta_H(a) = \frac{a^2}{R} \ , \tag{2.4.2}$$

where $E^* = \frac{E}{1-\nu^2}$ is the reduced elastic modulus and E is the Young modulus of the semi-sphere. The first equation states that the contact radius will increase if we push harder (indentation force F_H) and the second one is a simple geometrical relation. In actual experiments, the load force and the contact radius are usually measured as a function of the imposed displacement indentation. In this case is useful to express the Hertz's theory as follows:

$$F_H(\delta) = \frac{4E^*}{3} \sqrt{R} \delta^{3/2} \ , \tag{2.4.3}$$

$$a_H(\delta) = \sqrt{R} \delta^{1/2} \ . \tag{2.4.4}$$

We can recover Hertz law with scaling arguments. In the limit $a \ll R$, the deformation in the indentation direction is of order $\varepsilon \sim \delta/a$. This deformation involves an obvious lateral length scale a. Due Saint Venant principle, the deformation in the vertical direction also occurs on the same length scale. The volume involved by the deformation is therefore proportional to a^3, which leads to the elastic energy is $\mathscr{E}^* \sim E^* \varepsilon^2 a^3 \sim E^* \sqrt{R} \delta^{5/2}$, where we have used the geometrical relation 2.4.4. In this way, the load force is given by:

$$F_H(\delta) = \frac{d\mathscr{E}}{d\delta} \sim E^* \sqrt{R} \delta^{3/2} \ , \tag{2.4.5}$$

which recovers the right scaling law expression for the force of equation 2.4.3. In this way we can also define the stiffness by the following equation:

$$S_H(a) = \frac{dF_H(a)}{d\delta}|_{\delta(a)} = 2E^* a \,. \tag{2.4.6}$$

2.4.2. Adhesive contact: JKR theory

Different theories of adhesion have been developed since the beginning of the 20th century. In a first instance all of them were conceived to interpret the adhesive case of the previously described Hertz's configurations, i.e. the contact sphere/sphere or sphere/plane. Some good reviews explaining these theories from a theoretical and conceptual perspective can be found in [33, 34].

The most used models in contact mechanics are the Derjaguin-Muller-Toporov (DMT)/Bradley model [35, 36] and the Johnson-Kendall-Roberts model (JKR) [20]. These two theories exhibit inconsistencies if we analyze the maximum tensile force needed to break the adhesive contact (the so called pull-off force). This discrepancy was first analyzed by Tabor [37] and later explained by Maugis [38] and Greenwood [39]. Maugis unifies both models in a single description, by extending the Dugdale-Barenblatt approach for a plastic crack [40] to an adhesive contact. He includes a cohesive zone around the contact where stresses are constant, thus avoiding the presence of singularities at this level. In this way, a general theory can be obtained for which DMT and JKR models are opposite limits (Maugis-Dugdale theory). The transition between both models is explained by considering a non-dimensional parameter representing the ratio between two lengths scales:

$$\mu_T = \frac{\delta_{po}}{\delta_i} = \frac{R^{1/3}\gamma^{2/3}}{E^{*2/3}\delta_i}\,. \tag{2.4.7}$$

This is the so called Tabor's parameter μ_T. Here, δ_{po} is the elastic displacement at pull-off force, which essentially corresponds to the height of the neck at the contact edge (fig. 2.9). It can be expressed as a function of the work of adhesion γ, the radius of the sphere R and the reduced elastic modulus E^*. The distance δ_i is the equilibrium distance between the two surfaces, roughly the interatomic distance at the closest contact point (typically of the order of nanometers).

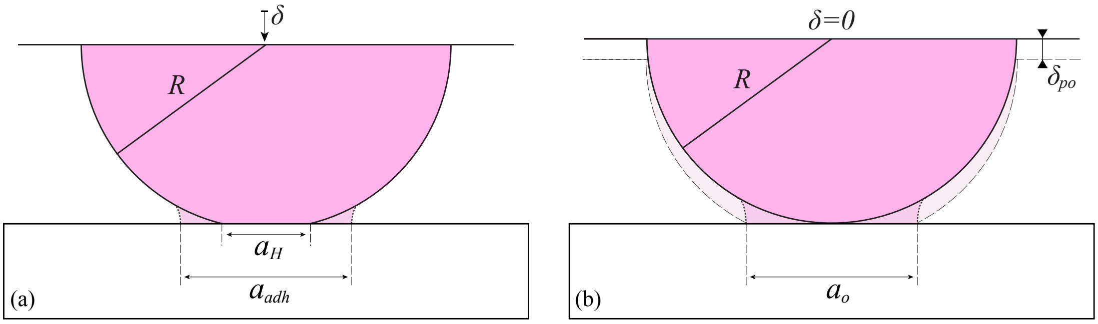

Figure 2.9.: *Spherical punch indented on a rigid plate. (a) The comparison between the non-adhesive (Hertz) and adhesive (JKR or DMT) contact radius for an equal indentation displacement δ. In the non-adhesive case, the contact radius is smaller ($a_H \leq a_{adh}$). (b) For null indentation displacement $\delta = 0$, in the adhesive case there is a contact radius equal to a_o. The solid displacement $\delta_{po} = \delta_{neck}$ is the solid displacement needed to have the same contact radius in the non-adhesive case.*

Tabor's parameter should be always calculated in order to distinguish which contact theory should be used to analyze experiments. Thus, when $\mu_T \ll 1$ DMT theory applies, which correspond to the limit of small, hard spheres with short-range adhesive interaction. On the other hand, when $\mu_T \gg 1$, JKR theory should be used. This corresponds to the limit of large soft compliant spheres submitted to long-range adhesive interactions.

JKR theory is the most relevant for the practical situations investigated in the current thesis involving soft materials. We thus focus on the details of this approach in this section. The assumptions of JKR model are the same that Hertz's theory but including the effect of adhesion. However, although stresses remain compressive at the center, tensile adhesive stresses appears close to the edge of the contact, and even diverges along the contact line. In addition, JKR theory neglects completely the adhesive interactions in the separation zone, i.e. outside the contact area.

The original JKR result is a model which relates F, a and δ as follows:

$$F(a) = \frac{4E^*}{3R} a^3 - 2\sqrt{2\pi E^* \gamma}\, a^{3/2} , \tag{2.4.8}$$

$$\delta(a) = \frac{a^2}{R} - \sqrt{\frac{2\pi\gamma}{E^*}}\, a^{1/2} , \tag{2.4.9}$$

where γ is the work of adhesion. We immediately note that, when $\gamma = 0$ we recover Hertz's theory.

One way to calculate these expressions is to interpret adhesion (or more exactly, debonding) in terms of fracture mechanics. The *energy release rate* G is then computed during the unloading process. At mechanical and thermodynamic equilibrium the Griffith's criterion states that $G = \gamma$.

JKR by using scaling

JKR solutions are based on the linear superposition of the adhesion-less Hertz's contact and the spherical punch solutions with adhesion. During unloading, when the sphere is moving away from the plane, a small neck of volume $v \sim a^2 \delta_{neck}$ is present, just before both surfaces totally separate. This meniscus is completely sustained by the competition between elastic and adhesive forces. Note that in this configuration we are in the regime $a \ll R$ where the deformations are essentially given by $\varepsilon \sim \delta / a$.

The elastic energy stored in this neck can be estimated by $\mathscr{E}_{el} \sim E^* \varepsilon^2 a^2 \delta_{neck} \sim E^* \delta_{neck}^3$, which leads to an elastic force $F_{el} \sim E^* \delta_{neck}^2$. On the other hand, the adhesive surface energy present on the neck is $\mathscr{E}_s = \gamma\pi a^2$, which gives a force $F_s \sim 2\gamma\pi a$ acting on the line enclosing the contact area (contact line). By balancing both forces we obtain:

$$\delta_{neck} \sim \sqrt{\frac{2\pi\gamma}{E^*}} a^{1/2} , \tag{2.4.10}$$

which corresponds to the adhesive contribution term of the equation 5.1.2. We also note that, by multiplying δ_{neck} by the stiffness $S_H(a)$ of the system (Eq. 2.4.6), we obtain the force acting on the neck:

$$F_{neck} \sim S_H(a)\delta_{neck} \sim \sqrt{2\pi\gamma E^*} a^{3/2} , \tag{2.4.11}$$

which corresponds to the adhesive part of the force in equation 2.4.8.

The typical value of the contact radius a_{typ} can be estimated by minimizing both energetic contributions with respect to the contact radius. Being the Hertz's energy, i.e. the elastic energy for the non-adhesive force, $\mathscr{E}_{el} \sim E^* a^5/R^2$ and the surface energy $\mathscr{E}_s \sim \pi\gamma a^2$ we can obtain:

$$a_{typ} \sim \left(\frac{\pi\gamma R^2}{E^*}\right)^{1/3} . \tag{2.4.12}$$

We finally note that by replacing Eq. (2.4.12) in Eq. (2.4.10) we obtain a typical value for the height of the neck:

$$\delta_{typ} \sim \left(\frac{\pi\gamma^2 R}{E^{*2}}\right)^{1/3} , \tag{2.4.13}$$

which essentially corresponds to the previously defined length δ_{po} used in the estimation of Tabor's parameter (see Eq. (2.4.7)).

Non-parametrical representation

In this section we perform some analysis of the the JKR model. For this purpose we can rewrite the JKR equations by using the following non-dimensional parameters: a/a_o, $\delta/(a_o^2/R)$ and $F/(\pi\gamma R)$ [38, 41]. Here, the contact radius at the instant of zero indentation is defined as $a_o = a(\delta = 0)$, so that $\frac{2\pi\gamma R^2}{E^*} = a_o^3$, and the unitary force $\pi\gamma R$ being proportional to the minimal force $F_{po} = -\frac{3}{2}\pi\gamma R$. In this way, the completely non-dimensional, non-parametrical equations read:

$$\frac{F}{\pi\gamma R} = \frac{8}{3}\left(\frac{a}{a_o}\right)^3 - 4\left(\frac{a}{a_o}\right)^{3/2} \quad \text{and} \quad \frac{\delta}{(a_o^2/R)} = \frac{a}{a_o} - \left(\frac{a}{a_o}\right)^{1/2} . \tag{2.4.14}$$

Here, the indentation displacement is re-scaled by the factor $\delta_H^o = a_o^2/R$, which corresponds to the indentation in the non adhesive case ($\gamma = 0$) necessary to obtain a contact radius a_o. The corresponding curves are shown in figure 2.10, where the shape does not depend on any physical parameter.

The minimal indentation force, the so-called the pull-off force F_{po} (also know as adhesive force F_a), does not depend on the rigidity of the material (its Young modulus) and is proportional to the adhesion energy as follows: $F_{po} = -3/2(\pi\gamma R)$, (see figures 2.10(a) and 2.10(b)).

The value of the contact radius that minimizes the force is:

$$a_{po} = \left(\frac{9}{8}\frac{\pi\gamma R^2}{E^*}\right)^{1/3} = \left(\frac{9}{16}\right)^{1/3} a_o,$$

which must not be confused with the contact radius for the minimal indentation displacement, which is:

$$a_d = \left(\frac{1}{8}\frac{\pi\gamma R^2}{E^*}\right)^{1/3} = \left(\frac{1}{16}\right)^{1/3} a_o.$$

These values are shown in the figures 2.10, where $(a_{po}/a_o) \approx 0.83$ is represented by a circle ○ and $(a_d/a_o) \approx 0.39$ by a triangle △.

The minimum force could allow us to infer directly the adhesion energy, since it does not depend on the rigidity of the material. Nevertheless, the contact radius and the indentation displacements do depend on the rigidity of the material. We note that Hertz's configuration can not be recovered form the previous representation and is used to an adhesive system. However, to observe the JKR and Hertz behavior together, a second re-normalization can be used.

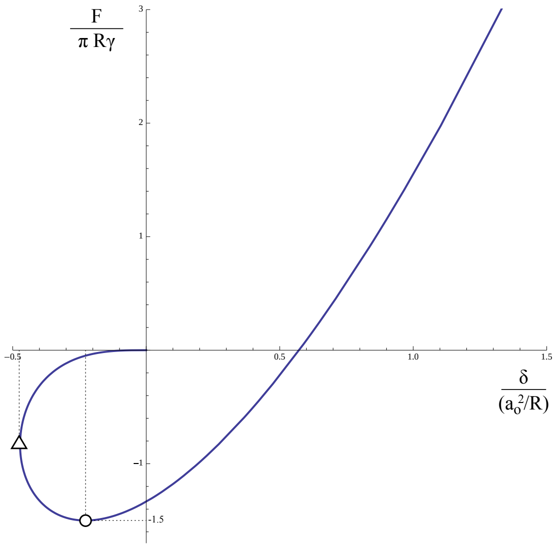

(a) Non-dimensional indentation force *vs* displacement

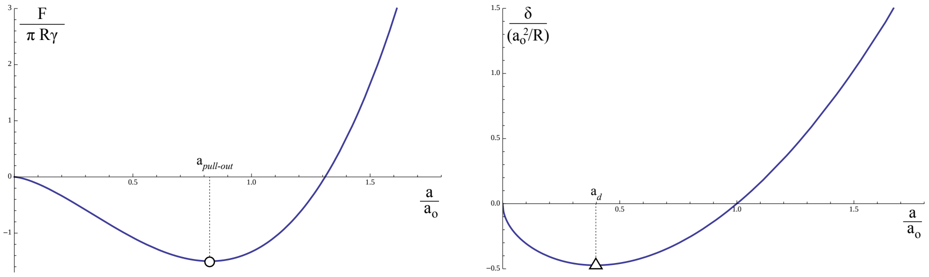

(b) Non-dimensional indentation force *vs* Contact radius

(c) Non-dimensional indentation displacement *vs* Contact radius

Figure 2.10.: *Master curves of an adhesive spherical punch indented on a rigid plate.*

Representation with a single parameter: Adhesion

JKR equations can be further analyzed by considering the following adimensional equations:

$$\frac{F}{\frac{4}{3}E^*R^2} = \left(\frac{a}{R}\right)^3 - \frac{3}{2}A\left(\frac{a}{R}\right)^{3/2} , \qquad (2.4.15)$$

$$\left(\frac{\delta}{R}\right) = \left(\frac{a}{R}\right)^2 - A\left(\frac{a}{R}\right)^{1/2} , \qquad (2.4.16)$$

where $F/\frac{4}{3}E^*R^2$, a/R and δ/R are the non-dimensional variables. A single non-dimensional parameter $A = \sqrt{\frac{2\pi\gamma}{E^*R}}$ can be tuned in order to modify the shape of the indentation curves. The non-dimensional parameter A can be rewritten in terms of the value of the contact radius at the instant of zero indentation a_o as $A^2 = (a_o/R)^3$ (eq. 2.4.14). Note that it is also related to δ_{po}, the approximated height of the adhesive neck during unloading, defined on Tabor's parameter. We display in figure 2.11, the plots of the previous non-dimensional equations. In figure 2.11(a), the non-dimensional indentation force is plotted as a function of the displacement for various values of A. Note that when $\gamma = 0$ (i.e. $A = 0$) the Hertz's theory is recovered (see blue curve in figure 2.11). Once adhesion is greater than zero, the indentation displacement can be negative when pulling out the sphere. Note that when increasing the value of the parameter A the non-dimensional force and indentation displacement decrease their values for a given contact radius, see figures 2.11(b) and 2.11(c).

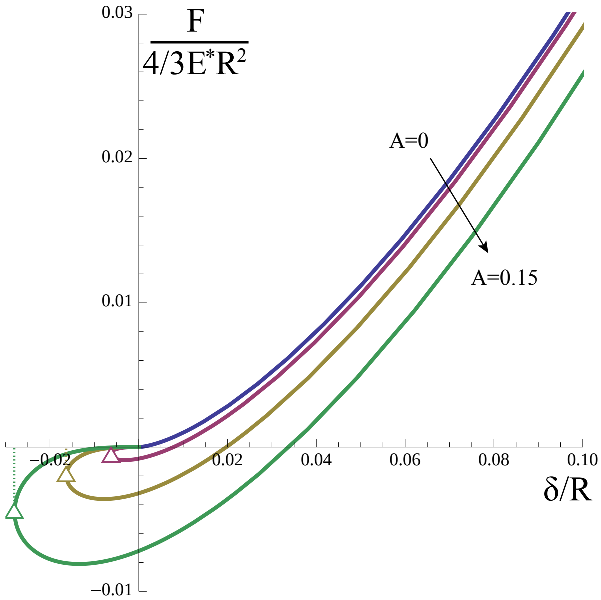

(a) Indentation force *vs* indentation displacement

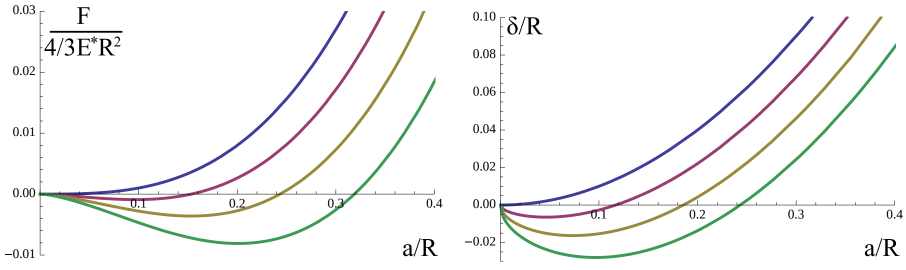

(b) Indentation force *vs* Contact radius

(c) Indentation displacement *vs* Contact radius

Figure 2.11.: *Theoretical curves of the non-dimensional variables showing the implicit relation between the equations (2.4.15) and (2.4.16). Different colors represent different values of the parameter A, from 0 to 1.32.*

Adhesion Hysteresis

Before closing this section, we have a last remark concerning the practical difference between indentation tests in loading or unloading cycles. Until now, we have indeed considered surfaces in ideal equilibrium conditions, for which the relation $W = 2\sigma$ is valid (when materials are the same). We thus assumed that the reversible work required to separate two surfaces from contact or two bring them together is the same. However, under realistic conditions, we observe that separating two surfaces involves more energy dissipation than the energy recovered by spontaneous adhesion. This difference is know as adhesion hysteresis and is usually defined as

[42]:

$$\Delta\gamma = (\gamma_r - \gamma_a)\,, \tag{2.4.17}$$

where γ_a is the advancing surface energy during loading and γ_r is the receding surface energy on unloading (note that $\gamma_r > \gamma_a$). Therefore, $\Delta\gamma$ is a measure of energy dissipation during a complete loading/unloading cycle. Thus, for two equal materials, the adhesion energy hysteresis per unit area is given by (or the work of adhesion of hysteresis):

$$W_{hyst} = 2\Delta\gamma\,. \tag{2.4.18}$$

Adhesion hysteresis can arise even between perfectly smooth and chemically homogenous surfaces supported by perfectly elastic materials. It can originate from some imperfections in the system such as rough or chemically heterogeneous surfaces, or because the supporting material is viscoelastic. However, mechanical instabilities, chemical interdiffusion, molecular reorientations and exchange processes at the interface after contact can produce the hysteresis. All these complex processes are certainly beyond the scope of this thesis.

2.5. Friction

Friction is one of the long-standing problems in physics which still remains partially unsolved. In this section we discuss some aspects of the frictional behavior of soft elastomers when they are squeezed and translated onto rigid smooth materials. We start with a general description of friction, from an historical perspective. We review the classical macroscopic results of macroscopic hard friction and we finally present the case of soft friction, where microscopic properties are important.

2.5.1. Basics on Friction: Hard materials

Friction is a dissipative process resulting from the relative motion of bodies in contact. Because of friction, continued energy input is required to sustain the relative motion between them. This relative motion is in general a combination of complex motions but is essentially governed by sliding, i.e. a linear displacement tangential to the contact plane.

At the beginning of the Renaissance, da Vinci discovered that the maximum force a block sitting on a plane can sustain before sliding is proportional to its weight, independently of the area of the face of the block in contact with the plane. In 1699 Amontons rediscovered the proportionality between the normal forces and the tangential force during sliding motion. In 1781, Coulomb discovered the existence of a sliding threshold and also postulates the kinetic behavior of the sliding force. All their pioneering works can be summarized in the following rules:

- The tangential sliding force F_s does not depend on the shape of the bodies.
- The sliding begins just once a threshold value is reached. The specific threshold value is a function of the materials. Once this critical value is overcome, friction force acts in the direction opposite to the relative velocity.
- The sliding force F_s is proportional to the normal applied force F_n. The constant of proportionality is called the coefficient of friction μ. (Amontons' 1st law).

- The sliding frictional force is independent of the apparent contact area A_a (Amontons' 2nd law).
- The kinetic friction force is independent of the sliding velocity (Coulomb's Law).

All these rules consider the effect of friction at a macroscopic scale. However, if we looked in detail the contact between materials, we could see that surfaces are rough, exhibiting asperities on different length scales (from nanometers to millimeters).
More recently, the studies of metallic surfaces lead Bowden and Tabor [43] to consider the microscopic roughness of materials. They discovered that all the microscopic asperities lead to a real contact area A_r that is orders of magnitude lower than the apparent contact area A_a, since real contact is essentially just made at the top of those asperities. In that scenario, all the energy dissipation are due to heating, melting or small deformations of these quasi-punctual contacts of hard materials. Macroscopically, i.e. at the size of the contact they found that the real contact area is proportional to the imposed normal pressure, which leads to a friction force proportional to the real contact area $F_s \propto A_r$. The same criterion is applicable when describing the adhesion between rigid solids, since the actual contact area can indeed be much lower than the apparent one, the effective adhesion energy may be quite weak. Although Coulomb's law is very relevant for hard materials, it fails to describe friction in the case of soft and adhesive materials as we describe in the next section.

2.5.2. Soft Friction

When materials are soft enough, the contact occurs in a large area, since their surfaces would be able to deform and fill interstitial spaces. In this case, the proportionality between frictional force and real contact area has been shown to be still valid, at least at the macroscopic scale of the contact [44, 45]. As in the case of the adhesive contact problems, soft smooth and rough friction couples mechanical properties of materials, geometrical properties of interfaces (such as roughness) and physicochemical characteristics of their surfaces (such us surface tension). All of them can involve dissipative processes at molecular scales on the interface, and also bulk dissipation.
At the scale of a single asperity, frictional energy dissipation involves poorly understood physicochemical processes occurring at the intimate contact between surfaces, such us adsorption or entanglement/disentanglement mechanisms [46], as well as viscoelastic or plastic deformations [47, 48]. In order to consider all these intricate phenomena, one needs to postulate a local constitutive law indicating how shear stresses τ depend on normal stresses (pressure P) and on the sliding velocity v_s at the interface. However, as has been recently shown, the macroscopic Amontons-Coulomb rules are not longer valid for soft contact (smooth and rough), at least at this local, mesoscopic scale (about 1μm) [49, 50].

In this thesis we will be interested on the frictional behavior of smooth and soft rubbery-like materials, sliding against hard smooth/rough surfaces. As "smooth" we refer to materials that exhibit asperities at the molecular scale, i.e. nanometric roughness. In particular we will analyze the effect of soft friction in the case of a particular configuration of typical peeling test.
In 1995, Newby *et al.* [9, 51, 10] put in evidence the sliding of an elastic material (PDMS) on a rigid substrate through a peeling test. They observed that an elastic material could slide long distances before detaching, this sliding lead to an extra shear dissipation that was considered as friction. In figure 2.12(a) [10], we show an experimental image where a relative sliding of

can be observed. Fluorescent particles (white dots) track a sliding displacement toward the detachment front over a distance about 20% of the strip thickness during a 1 min interval. The length of the sliding zone is of the order 2 or 3 times the thickness of the strip. The shear stress extrapolated in the peeling configuration for a slip velocity of the order of 10 mm/min is about 100 kPa.

Ever since, efforts are made by mechanics and physico-chemical communities to quantify the effect of smooth soft friction on the energy release rate [11, 52] during detachment process or sliding. In particular, it has been shown that for the steady-state frictional regime of a smooth contact between PDMS or epoxy resin and glass, the local shear stress τ is pressure-independent and slightly vary with the sliding velocity [53, 54, 49, 45]. The shear stress is in this case associated with small-scale dissipative processes. For such a smooth and intimate contact, friction is usually considered to arise from molecular scale dissipative processes occurring at the sliding interface.

In figure 2.12(b) [53], we show a sliding front that propagates in the interface of a glass spherical lens indented on a PDMS plane. Once the materials are in contact over an area of radius a_c, a torsional displacement is applied to the lens. Initially, the two surfaces turn solidary. Beyond a threshold, a sliding front begins to propagate radially, from the contact radius inwards, diminishing the solidary area to a radius a_s. Using such images, where displacement can be directly measured, the authors compute with a sophisticated technique the shear stress. During this shear friction front propagation, they find that the shear stress is constant on the order of 200 kPa and does not depend on the normal load.

As mentioned above, formation and breakage of adhesive molecular bonds at the contact interface is often evoked as the underlying physical mechanism accounting for this phenomena [55, 56, 57, 46]. In such a way, τ can be considered as a constant during this work.

In the next chapter we will see how to incorporate the effects of friction in a modified version of the classical peeling test: A zero-degrees peeling test.

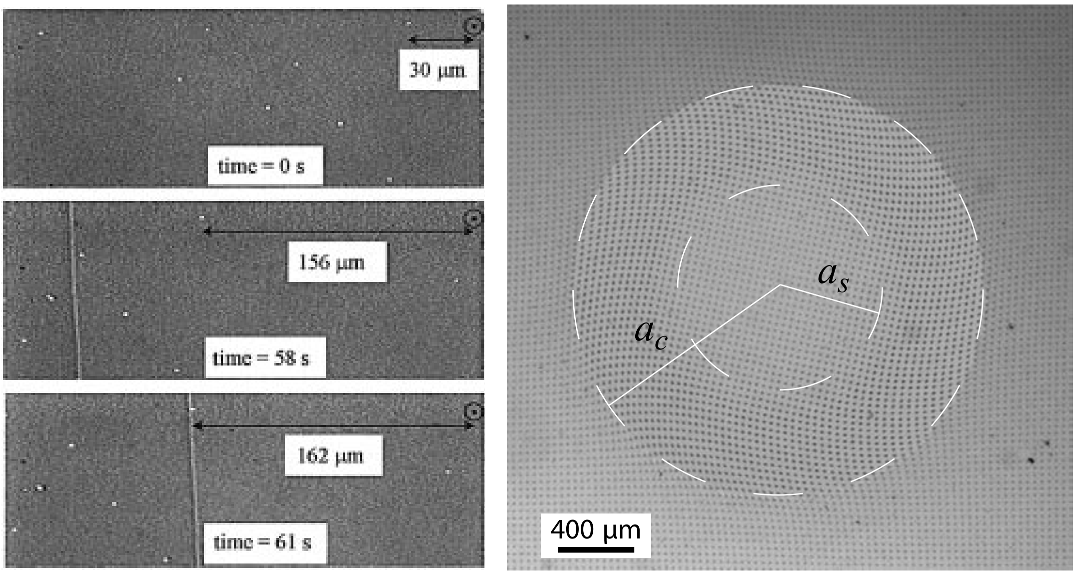

(a) Linear sliding

(b) Torsional sliding

Figure 2.12.: *(a) Linear sliding in a peeling test [10], fluorescent particles (white dots) show an sliding of about a 20% of the strip thickness during 1 min. (b) Radial sliding on the interface of a rigid spherical probe indented on a PDMS plane [53], a sliding front propagates with a radial extension of* $(a_s - a_c)$.

3. Zero Degrees Peeling: Friction Effect

3.1. Introduction

In the previous chapter (sec. 2.3), we have briefly presented the classical peeling test, which is based on the pioneering works of Rivlin, Kaelble and Kendall [29, 58, 7, 8]. This standard technique for instance is commonly used to measure the adhesion energy of pressure sensitive adhesives [25, 26]. Although friction obviously prevent an adhesive tape to slide as it is pulled away, frictions effects are generally not considered in these approaches. However, experimental studies have put in evidence a sliding motion in the vicinity of the peeling front in the case of soft adhesive [10] or substrate [11]. Very recently, McMeeking and coworkers studied the effect of friction during the peeling of a strip of silicone adhering on a glass plate through van der Waals interaction [59, 52]. They observe also observe sliding in a region whose extension is on the order of the thickness of the strip. However they were not able to estimate the corresponding shear stress.

Intuitively we would expect friction to play a dominant role as low peeling angles are considered, and especially in a shear-lap configuration. This situation has been extensively by Crosby and coworkers who were inspired by the intriguing adhesion of gecko lizards on walls. They predict a maximum pulling load based on the mechanical compliance of the system and adhesion energy [60, 61]. Nevertheless, friction is also not considered in this approach.

Would friction be important in some situations and negligible in others? In this chapter, we propose to bring a new light on this apparent contradiction. We indeed present a simple experiment involving a strip of elastomer that adheres on a glass plate by van der Waals interactions. How much force does the operator need to apply to detach the tape by pulling on its free end tangentially to the plate? Will we observe a friction front as previously reported [10, 11, 59, 52]? Is this maximum load in agreement with the results from Crosby *et al.*?

3.2. Lap Test: two conflicting models

3.2.1. Stretching and a steady debonding

In his pioneering work, Rivlin showed how the force required to peeled away an inextensible adhesive tape diverges as the peeling angle vanishes [29]. Kendall demonstrated later that accounting for the finite extensibility of the tape leads to a plateau force for low peeling angles [8]. We can easily recover this force by considering a linear elastic strip adhered to a smooth rigid plate, as sketched in figure 3.1.

A displacement δ is applied parallel to the surface at the free end of the strip. We note E the Young modulus the elastic strip, h and w_o are its thickness and width respectively and γ is the interfacial toughness. As the displacement is imposed, a portion of the strip can detach from the rigid plate, leading to a new equilibrium interface. If the interfacial crack propagates over a distance x_f, the detached zone of the strip will be homogeneously deformed by a strain $\varepsilon_o = \frac{\delta}{x_f}$.

Two terms contribute to the total energy of the system: the stretching elastic energy $\mathscr{E}_{el}$ and the adhesion energy $\mathscr{E}_{adh}$,

$$\mathscr{E}_{el} = \frac{1}{2} E\, h w_o x_f \left(\frac{\delta}{x_f}\right)^2 \tag{3.2.1}$$

$$\mathscr{E}_{adh} = \gamma w_o x_f \tag{3.2.2}$$

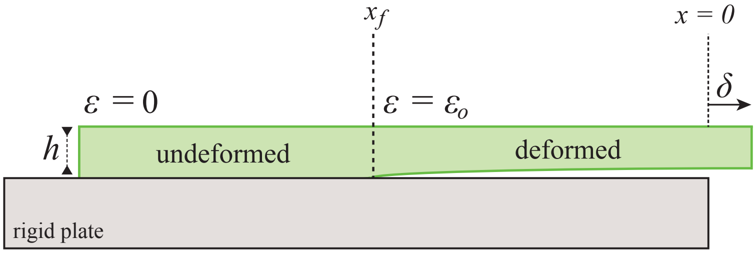

Figure 3.1.: *Schema of an idealized experiment: pulling a distance δ on the edge of a strip that initially was completely adhered, it detaches over a distance x_f.*

Minimizing the total energy with respect to the detached length x_f, provides the force balance

$$\frac{\partial \mathscr{E}_T}{\partial x_f} = -\frac{1}{2} E\, h\, w_o\, \delta^2 \frac{1}{x_f^2} + \gamma w_o \equiv 0 \tag{3.2.3}$$

from which we deduce the equilibrium position of the front,

$$x_f = \delta \sqrt{\frac{Eh}{2\gamma}} \tag{3.2.4}$$

The position of the front is thus proportional to the imposed displacement of the free end of the strip. This solution is mechanically stable since

$$\frac{\partial^2 \mathscr{E}_T}{\partial {x_f}^2} = E\, h\, w_o\, \delta^2 \frac{1}{x_f^3} \geq 0$$

In other words, the detachment front will propagate steadily if the displacement δ is progressively increased.
In terms of force, we find a steady value

$$F_K = Ehw_o\, \varepsilon_o = \sqrt{2Eh\gamma}\, w_o \tag{3.2.5}$$

which is similar to the prediction from Kendall for vanishing peeling angles.

3.2.2. Compliance and unstable debonding

Motivated by the design of biomimetic adhesives, Crosby and coworkers recently developed a different concept to predict the adhesive force capacity of a system on lap geometry [60, 61]. They were inspired by gecko lizards that exhibit strong adhering forces. Geckos can indeed climb safely along a wide variety of surfaces ranging from smooth glass plates to rough wooden barks. The amazing adhesion properties of their feet relies on their finely divided structure that provides enough compliance to accommodate the topography of rough substrates. These structures are terminated by spatulas with a diameter on the order of 200 μm, which have been shown to provide adhesion uniquely through van der Waals interactions [6].

As a general model, Crosby and coworkers consider an elastic body of a given shape, which is in contact to a rigid surface over an area A. A pulling force is applied to the elastic body. They assumed that beyond a critical load F_c the whole body suddenly detaches. This critical force is interpreted as the point when the elastic energy stored in the material overcomes the adhesion energy. The compliance of the system is defined as $C = \frac{\partial \delta}{\partial F}$ in a tensile test. As a consequence, a linear elastic system stores an energy $\mathscr{E}_{el} \sim CF^2$ as it is loaded with a force F. This energy reaches the adhesion energy $\mathscr{E}_s = \gamma A$ for the critical load:

$$F_c \sim \sqrt{\gamma A/C}. \tag{3.2.6}$$

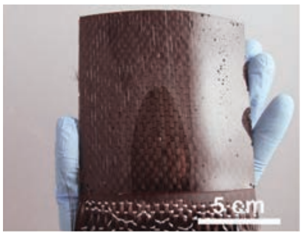

Figure 3.2.: *Adhesive pad composed of a stiff fabric imbibed with a soft adhesive elastomer, image extracted from [60].*

Although friction is not considered in this approach, nor the kinetic energy generated by the unstable fracture propagation, this relation is nicely verified on a wide range of biological and model systems. The model system is an adhesive pad composed of a stiff fabric backing of thickness h_b and Young modulus E_b coated with a compliant PDMS elastomer of thickness h and Young modulus E. An example is shown in figure 3.2. The adhesive pad verifies the condition i.e. $E_b h_b \gg \mu h$, where $E_b h_b = 4 \cdot 10^6$ N/m is the stiffness of the fabric layer, with $h_b = 400\,\mu$m and $\mu \sim 1$ MPa and $h \sim$ 1mm. In other words, the deformation is concentrated in the elastomer, while the fabric layer can be considered as inextensible.

A typical experience conducted with such pad is shown in figure 3.3(a). The compliance of the system C and the force capacity F_c are measured directly from the initial slope and the maximum of the force-displacement curve. The figure 3.3(b) represents a compilation of peeling experiments (from [60]). The data collapse over 4 orders of magnitude on a universal relation $F_c = \sqrt{G_c A/C}$, where G_c is the debonding energy. The average value of G_c is on the order of 30 N/m, but if take into account the scattering, we find a window of 20-200 N/m. This value is huge in comparison with the adhesion energy we expect for PDMS on glass, $\gamma \sim 0.1 - 1$ N/m.

To gain further insight in the debonding mechanism we consider an adhesive elastomer (of thickness h, width w_o and shear modulus μ) covered with an inextensible backing as in the geometry sketched in figure 3.4. If a load F parallel to the strip is applied, the backing layer is translated as a rigid body along a distance u, which induces a uniform shear strain u/h in the portion of the elastomer adhering to the rigid substrate. The zone of the strip which is out of contact is not deformed.

In this system, the elastic energy stored due to shear on the deformable adhesive is $\mathscr{E}_{sh} = \mu h (\frac{u}{h})^2/2$ per unit area. As a consequence, if the debonding front advances over a distance dx, the shear layer will release $\mu (\frac{u}{h})^2 w_o h \mathrm{d}x/2$ of elastic energy. Conversely, the displacement of the crack front will represent a cost in surface energy of $G_c w_o \mathrm{d}x$. We expect the front to propagate when the energy released overcomes the cost in debonding, which corresponds to the the critical displacement:

$$u_c = \sqrt{2 G_c h/\mu}$$

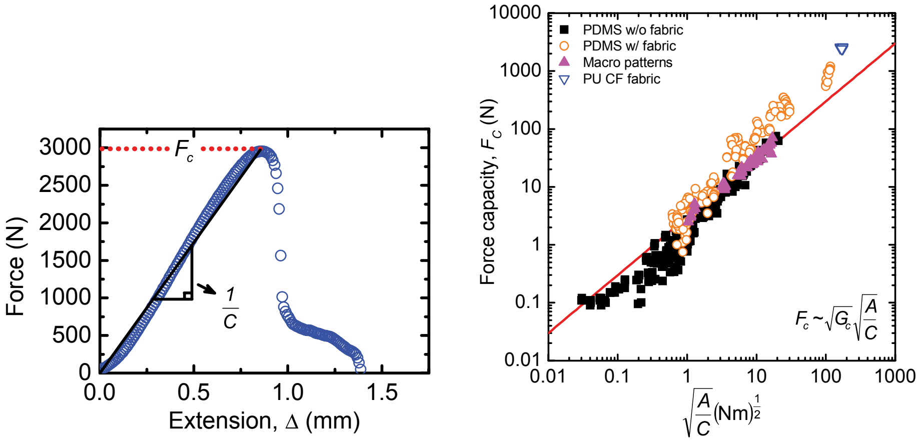

(a) Compliance and force capacity measurement (b) Maximal force capacity at detachment

Figure 3.3.: *Figures of a shear lap test made by Bartlett and coworkers with a stiff pad coated with a soft adhesive layer [60].*

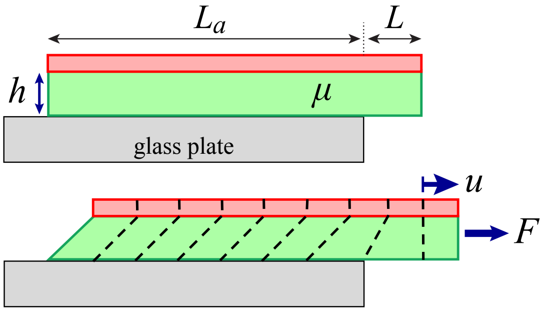

Figure 3.4.: *Sketch of an idealized shear lap experiment. (Up) Non-deformed state. (Bottom) Shear-deformed system. In red, a rigid backing covering the elastic adhesive layer, in green.*

. In terms of stresses, we obtain a critical shear stress along the adhesive layer $\mu u_c/h$, which leads to the critical load $F_c = \mu L_a w_o u_c/h$. Equation (3.2.6) is finally recovered:

$$F_C = A\sqrt{2\mu G_c/h} = \sqrt{2\gamma A/C} \tag{3.2.7}$$

where $A = wL_a$ is the adhesion area and $C = h/\mu w L_a$ the compliance of the system.

This scaling relation is not compatible with the peeling force predicted by Kendall (Eq. 3.2.5) which does not depend on the adhering length. Indeed, in the case of a strip simply composed of an elastomer (no stiff backing), the compliance is given by $C = L/(Ehw_o)$, where L is the length of the portion of the strip that is free of contact.

Equation (3.2.6) would thus lead to

$$F_C = \sqrt{2Eh\gamma}w_o\sqrt{L_a/L}\,, \tag{3.2.8}$$

which is in contradiction with Kendall's prediction, where the critical detachment force is constant and does not depend on the adhering length L_a. Nevertheless, if the free length L is of the same order of the adhered length L_a, both models are equivalent.

3.2.3. Reconciliation of both mechanisms

Which mode of failure should be selected in the case of a strip of soft elastomer covered with a more rigid strip? We sketch such a bilayer system in figure 3.5. We represent in red a stiff and thin elastic backing layer with Young modulus E_b and thickness h_b. And in green a soft elastic adhesive material, with Young modulus E and thickness h. Both layers are sticked together to prevent any relative slide. The strip of total length X adheres on the substrate over a length L_a while a pulling load is applied in the remaining portion, of initial length L (Fig.3.5).

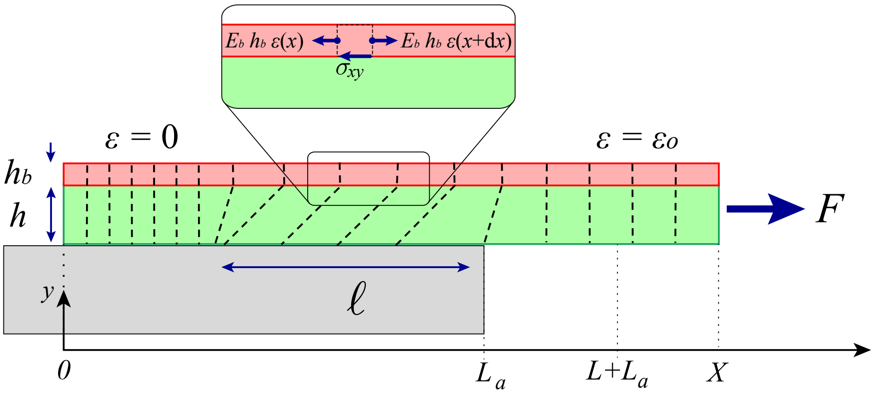

Figure 3.5.: *Sketch of an idealized shear lap experiment of a double layer elastic material. A stiff backing (in red) covers a sorter elastic material (in green). The coupling between the finite stifness of the backing and the shear in the soft adhering strip results into decay of the local strain characterized by a length scale* ℓ_{lag}.

We now consider the finite stiffness of the baking layer. In the detached side of the strip, we expect the strain to be uniform and stresses and to be dominated the elasticity of the stiffer material (the baking). How do strain and stresses evolve in the adhering part of the strip?

Although the stiffness of the baking is finite, we still consider that the baking is more rigid than the elastomer layer, i.e. $Eh \ll E_b h_b$. In addition, we assume that the backing layer is much thinner than the adhesive layer ($h_b \ll h$). Within this limit, the elastic strip is mainly submitted to a simple shear, whereas the stiff backing undergoes stretching deformation.

Consider a small slice of the backing layer as in the zoom-in of figure 3.5. A simple force balance on a short portion of the strip gives the reaction force due to the shear on the adhesive layer and the stretching of the backing layer [58, 62],

$$-\sigma_{xy} w_o \mathrm{d}x + E_b h_b w_o \varepsilon(x+\mathrm{d}x) - E_b h_b w_o \varepsilon(x) = 0$$

Where the shear stress on the adhesive layer is given by $\sigma_{xy} = E\frac{u}{3h}$, where $u(x)$ is the local displacement of the tape at the position x. This force balance leads to the equation

$$\frac{E}{3h}u - E_b h_b \frac{\partial^2 u}{\partial x^2} = 0 \tag{3.2.9}$$

As described by Kaelble, the integration of this equation leads to an exponential decay of the strain of the strip over a typical shear-lag distance:

$$\ell_{lag} = h\sqrt{3\frac{E_b h_b}{Eh}}. \tag{3.2.10}$$

Equation 3.2.9 can be rewritten as:

$$\frac{\partial^2 u}{\partial x^2} = \frac{u}{\ell_{lag}^2},$$

which solution is of the form $u(x) = A\cosh\left(\frac{x}{\ell_{lag}}\right) + B\sinh\left(\frac{x}{\ell_{lag}}\right)$. The boundary conditions are (1) $u'(0) = 0$ and (2) $u'(L_a) = \varepsilon_o$. The condition (1) leads to $B = 0$ and the condition (2) leads to $A = \frac{\varepsilon_o \ell_{lag}}{\sinh\left(\frac{L_a}{\ell_{lag}}\right)}$. The expressions for the displacement and the strain are finally:

$$u(x) = \varepsilon_o \ell_{lag} \frac{\cosh\left(\frac{x}{\ell_{lag}}\right)}{\sinh\left(\frac{L_a}{\ell_{lag}}\right)} \quad \text{and} \quad u'(x) = \varepsilon_o \frac{\sinh\left(\frac{x}{\ell_{lag}}\right)}{\sinh\left(\frac{L_a}{\ell_{lag}}\right)}$$

These expressions allows us to compute the total elastic energy per unit width of the system:

$$\mathscr{E} = \int_0^{L_a} \left[\frac{1}{2}E_b h_b (u')^2 + \frac{1}{6}Eh\left(\frac{u}{h}\right)^2\right] \mathrm{d}x + \frac{1}{2}E_b h_b \varepsilon_o^2 (X - L_a)$$

In the contact zone, we integrate two terms, the first one corresponds to the stretching energy of the backing layer and the second one to the shear energy on the compliant adhesive layer. The third term in the equation corresponds to the stretching energy of the non adhered strip.
After integration we obtain:

$$\mathscr{E} = \frac{1}{2}E_b h_b \varepsilon_o^2 \left[\ell_{lag} \coth\left(\frac{L_a}{\ell_{lag}}\right) + X - L_a\right]$$

However, we are interested on computing the energy release rate $G = \frac{\partial \mathscr{E}}{\partial L_a} - F\frac{\partial u(X)}{\partial L_a}$. The variation of the energy is simply given by

$$\frac{\partial \mathscr{E}}{\partial L_a} = -\frac{1}{2}E_b h_b \varepsilon_o^2 \coth^2\left(\frac{L_a}{\ell_{lag}}\right)$$

On the other hand, the displacement at the point X is $u(X) = \varepsilon_o(X - L_a) + u(L_a)$ and the force per unit width is $F = E_b h_b \varepsilon_o$. The second term on the energy release rate is then

$$F\frac{\partial u(X)}{\partial L_a} = -E_b h_b \varepsilon_o^2 \coth^2\left(\frac{L_a}{\ell_{lag}}\right)$$

Finally we obtain the following expression for the energy release rate:

$$G = \frac{1}{2}E_b h_b \varepsilon_o^2 \coth^2\left(\frac{L_a}{\ell_{lag}}\right) = \frac{1}{2}E_b h_b \varepsilon_o^2 \left[1 + \frac{1}{\sinh^2\left(\frac{L_a}{\ell_{lag}}\right)}\right] \tag{3.2.11}$$

From the previous equation we can extract two asymptotic behaviours

$$\begin{cases} \text{If } L_a \gg \ell_{lag}\ , \quad G \simeq \frac{1}{2}E_b h_b \varepsilon_o^2\ , \\ \qquad \text{then taking } G = \gamma \ \rightarrow F_c = w_o\sqrt{2\gamma E_b h_b} \\ \\ \text{If } L_a \ll \ell_{lag}\ , \quad G \simeq \frac{1}{2}E_b h_b \varepsilon_o^2 \left(\frac{\ell_{lag}}{L_a}\right)^2, \\ \qquad \text{then taking } G = \gamma \ \rightarrow F_c = w_o\sqrt{2\gamma E_b h_b}\left(\frac{L_a}{\ell_{lag}}\right) \end{cases} \tag{3.2.12}$$

The first case is equivalent to the prediction from Kendall, where the shear-lag length is negligible and the force does not depend on it: for $L_a \gg \ell_{lag}$, $F_c = F_K = w_o\sqrt{2\gamma E_b h_b}$.

In the second case, $L_a \ll \ell_{lag}$, the critical detaching force is inversely proportional to the shear-lag length. However if we input the relation $\ell_{lag} = h\sqrt{\frac{E_b h_b}{\mu h}}$ in the previous expression, we obtain $F_c = w_o L_a\sqrt{\frac{2\gamma\mu}{h}} = A\sqrt{\frac{2\gamma\mu}{h}}$. We thus recover the same expression as in equation (3.2.7) for a catastrophic debonding mechanism.

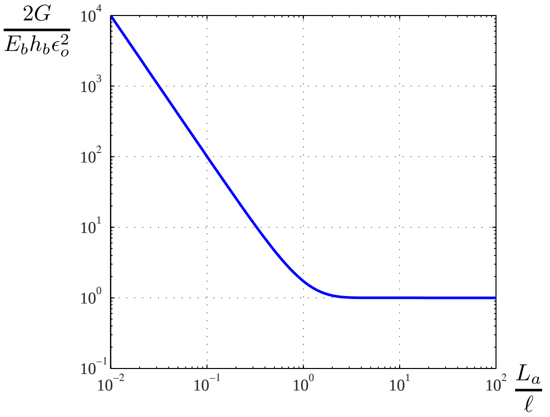

Figure 3.6.: *Non-dimensionalized energy release rate as a function of the ratio between the initially adhering length and the shear-lag length.*

In figure 3.6, we show a plot of the non-dimensional energy release rate $\frac{2G}{E_b h_b \varepsilon_o^2}$ as a function of the ratio of the initially adhering length with the shear-lag length L_a/ℓ_{lag}. Their dependence is given by equation 3.2.11. For $L_a/\ell_{lag} \gg 1$, the energy release rate (more precisely G/ε_o^2) is constant, so the crack propagation is stable. Its value corresponds to the adhesion energy and this scenario corresponds to front propagation described by Kendall. For $L_a/\ell_{lag} \ll 1$, G/ε_o^2 increases as L_a decreases. As a consequence, the energy release rate increases as the crack propagates. This situation is therefore unstable and leads to the sudden detachment of the whole strip.

In the case of the work presented by Crosby *et al.* in [60], we find $\ell_{lag} \approx 5$ cm, while the attached length $L_a \approx 10$ cm, which means that even when $\ell_{lag} \sim L_a$, the critical force will be high and the system will detach in a non-stable manner in agreement to the experimental observations. Conversely, if the strip is composed by a single material, we obtain $\frac{E_b h_b}{\mu h} = 1$. It means that the shear-lag length is of the order of the thickness of the strip and then we will recover the regime from Kendall.

As a conclusion, the mode of failure is selected by the length of the adhered zone L_a compared to the shear lag decay length ℓ_{lag}. Longer adhered areas will eventually reach the plateau predicted by Kendall (section 3.2.1), whereas shorter ones (or a very stiff backing) should follow a catastrophic scenario (section 3.2.2). However, although friction obviously prevents the tape from sliding, none of these mechanisms accounts for a possible energy dissipation through friction. One important hypothesis in Kendall's approach is to neglect the friction of the part of the strip which is after the front but is still in apparent contact with the substrate. Is this hypothesis always valid? Our experiences described in the following chapter will challenge this strong asumption.

3.3. Experimental methods

The experiments consist in pulling an elastic strip adhering to a rigid plate clamped in at the fixed jaw of a traction machine (figure 3.7). We conducted our experiments with strips made in PolyVinylSiloxane (PVS Elite Double 16, 22 and 32 from Zhermack) prepared by equal quantities of a “base” and “catalist” liquid. The strips were prepared with initial length of 250 mm, a width w_o ranging from 7.5 to 60 mm, and a thickness h of 1, 2 or 4 mm. The Young modulus of the PVS could be selected between 400 and 1200 kPa depending on the selected polymer. We present in table 3.3.1 the values of the Young modulus of the 2 mm thick strips used in our different experiments. Our experiments were performed on carefully cleaned smooth glass plates on which the strips spontaneously adhere through intermolecular interactions. The debonding energy was measured for each sample through a standard 90° peeling test[63] carried at a velocity of 0.5 mm/s with an Instron 5865 force-displacement machine. Depending on the elastic modulus and the peeling speed, the debonding energyγ could vary between 0.5 and 1.5 J/m^2. For details on the measurement of γ, see section 4.2.4. Note that γ is different from the work of adhesion that we determine with a splitting test [64, 65], $w_{ad} \sim 0.05-0.5$ N/m.

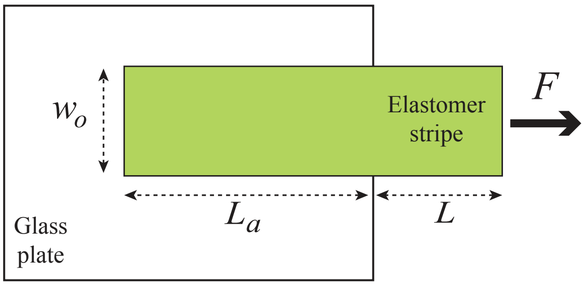

Figure 3.7.: *Sketch of the experimental setup at the initial stage, i.e. before any deformation is applied (top view). A long strip of elastomer (in green) of width w_o adheres on a glass plate along a length L_a. The force required to pull the free end of the strip of length L at a constant speed* v *is monitored with a force displacement machine.*

Before starting an experiment, a length of the strip L_a is deposited on the glass plate. After a waiting time on the order of 5 min, the extremity of the free portion of the strip is pulled at a constant velocity v ranging from 10 to 50 mm/min, while the glass plate is hold at a fixed position (Fig. 3.7). The pulling force $F(t)$ and the displacement of the free end $\delta(t)$ are simultaneously monitored. For a given set of experiments, the compliance of the non-adhering portion of the strip was maintained constant, i.e. its initial length had a fixed value $L = 40\,\text{mm}$. By refering to “longer” strip, we thus mean a longer initial adhering length L_a.

In the following section, we describe the force required to peeling away the strip. Will the force follow a plateau value as predicted by Kendall? Will we rather observe the catastrophic scenario presented by Crosby and coworkers?

●	$w_o = 7.5\,\mathrm{mm}$
Purple	E = 540 kPa
Yellow	E = 620 kPa
Green	E = 945 kPa
○	$w_o = 15\,\mathrm{mm}$
Purple	E = 470 kPa
Yellow	E = 615 kPa
Green	E = 1.26 MPa
△	$w_o = 30\,\mathrm{mm}$
Purple	E = 470 kPa
Yellow	E = 950 kPa
Green	E = 1.28 MPa
□	$w_o = 60\,\mathrm{mm}$
Purple	E = 580 kPa
Yellow	E = 740 kPa
Green	E = 1.05 kPa

Tables 3.3.1.: *Young modulus for data on this chapter.*

3.4. Peeling force

In this section we present preliminary data obtained from the force displacement machine. These raw results will be completed by a finer analysis of the detachment mechanism through image analysis.

3.4.1. Critical force

In figure 3.8, we present a typical set of curves of the tensile force F as a function of the imposed displacement d. In the limit of small displacements, the evolution of the force is linear. In agreement to Hooke's law, the slope of the curve is nearly proportional to the Young modulus of the elastic strip: $F/d = Ehw_o/L$. As the free end of the strip is pulled away, we observe a continuous increase of the force until the strip detaches completely in a sudden jump. Prior to detachment, the force sometimes displays jumps as it is commonly observed in systems displaying stick-slip behaviour. Qualitatively, the maximal force F_d is larger if the initial contact length is increased. All force-displacement curves also tend to collapse a a same master curve (although shorter strips detach earlier that longer ones). More quantitatively, the magnitude of the force is relatively high. In this set of experiments we obtained a a maximum value of F_d close to 18 N. Nevertheless, changing the elastic parameters or the adhering area can increase significantly the force. For instance, we obtained values up to 100 N, for $E \sim 1\,\text{MPa}$, $w_o = 60\,\text{mm}$ and $L_a = 140$ mm. Strikingly, the measured forces are much higher than the critical force predicted by Kendall, $F_K = 0.78$ N, for $\gamma \approx 1$ J/m^2.

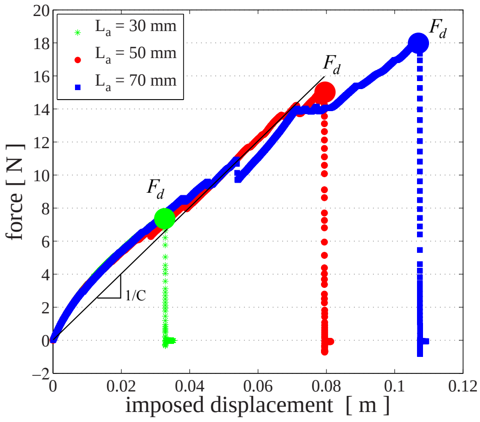

Figure 3.8.: *Tensile force applied to the strip as a function of the imposed displacement. The material parameters for the strip are E = 615 kPa, L = 40 mm, w_o = 15 mm, h = 2.2 mm.*

At first glance, the evolution of the force is reminiscent of the mechanism described by Crosby and coworkers where a sudden jump also follows a progressive increase of the force [60]. However, an estimate of the force from eq. (3.2.7) leads to $F_C \approx 0.65$ N, for an area $A = w_o L_a \simeq 10^{-3}$ m^2 and a compliance $1/C \approx 200$ N/m directly inferred from Fig. 3.8. This estimate is almost two orders of magnitude lower than the detachment force actually measured. Our preliminary observations thus strongly suggests that there is a different detachment mechanism which dissipates much more energy. A finer study of the evolution of F_d with the parameters of the experiment may however provide further informations.

3.4.2. An effect of the compliance?

We modified the compliance of the system ($C = L/Ehw_o$ selecting different lengths of the non-adhering part of the strip L. In fig. 3.9, represent the corresponding set of data obtained for $C = 1$ to 4 mm/N. Changing the compliance do not affect the evolution of the variation of F_d with L_a. This result is thus in contradiction with the mechanism described by Crosby *el al.* where the critical force is expected to follow $F_C = w_o\sqrt{2Eh\gamma L_a/L}$ in the current case of a strip composed of a single material. Indeed, the critical detachment force measured in our experiments is independent from L and follows a fairly linear dependence with L_a.

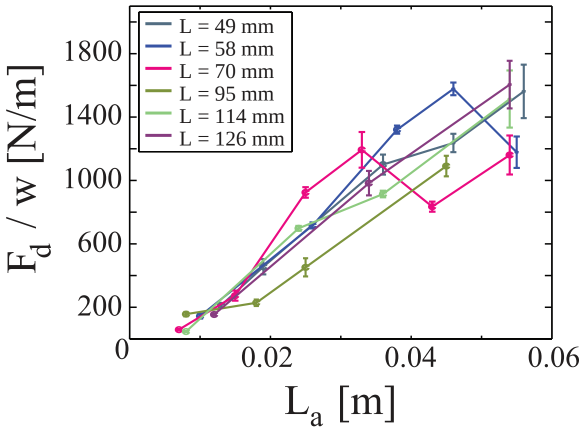

Figure 3.9.: *Detachment force divided F_d by the width of the strip as a function of the initially adhering length. F_d varies almost linearly with L_a and is independent from L (and therefore from the compliance). $w_o = 30$ mm, $h = 2.3$ mm, $E = 529$ kPa. $v = 50$ mm/min. In these particular experiments, the substrate was a PMMA plate (similar results were nevertheless obtained with a glass plate).*

To gain further insight, we performed similar experiments with strips of different geometries and elastic rigidities. We represent in figure 3.10 the maximum detachment force collected for these experiments as a function of the initially adhering area. The different symbols represent the data for different widths, while the colors indicate the Young modulus (green the stiffest ~ 1 MPa, and magenta the softest ~ 250 kPa). The variation of the thickness of the strip is limited since very thin strips are prone to break during the test and thick samples would remain in the limit of slender strips. In spite of some scattering, all the data tend to collapse in a single master curve. This curve is initially fairly linear and seems to saturate for high values of the contact area. In the linear part, the prefactor, which is homogeneous to a stress, is on the order of 20-30 kPa.

As a partial conclusion, these experimental results suggest a linear dependence of the force with the contact area:

$$F_d \sim \tau w_o L_a \tag{3.4.1}$$

This behavior is different from the models described by Kendall or Crosby and collaborators. However, the nature of the effective stress τ still remains an open question. Monitoring solely the force only provides an average estimate of this stress. Could we go beyond this limited analysis? In the following section we describe the propagation of the deformation along the strip, observed through image analysis.

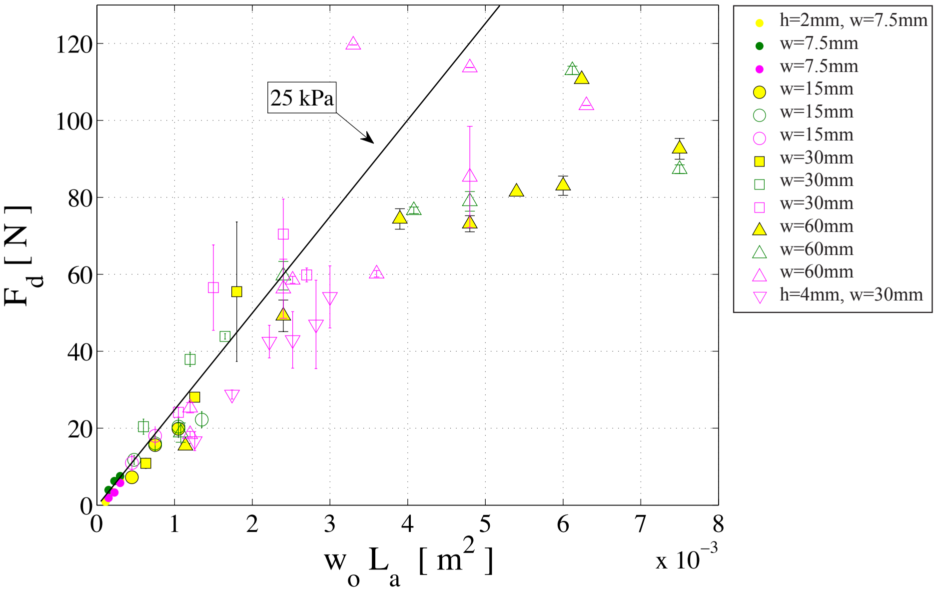

Figure 3.10.: *Force at the detachment of the strip* F_d *as a function of the initially adhering area. Specimens with* $h = 2\,mm$*:* $\bullet$ $w_o = 7.5\,mm$, $\circ$ $w_o = 15\,mm$, $\square$ $w_o = 30\,mm$, $\triangle$ $w_o = 60\,mm$*. Specimens with* $h = 4\,mm$*:* $\bigtriangledown$ *for* $w_o = 30\,mm$*. The color code corresponds to the Young modulus:* $E_{magenta} = 520(\pm 50)\,kPa$, $E_{yellow} = 730(\pm 160)\,kPa$ *and* $E_{green} = 1130(\pm 160)\,kPa$*. Error-bars represent the variation relative to three different experiments made with the same sample. See table 3.3.1.*

3.5. Propagation of a sliding front

We present in figure 3.11 successive snapshots of the strip captured during an experiment. The displacement of the free end of the strip is controlled and the corresponding pulling force is stable. The duration of the experiment is typically 5 min. Images of the strip are simultaneously taken for a further image analysis.

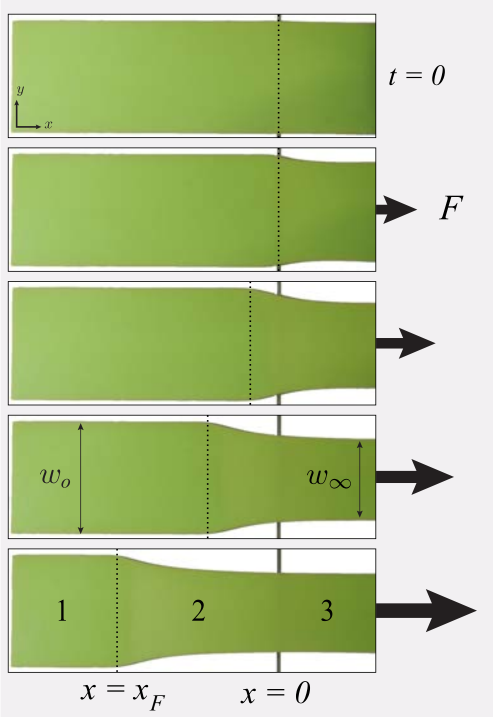

Figure 3.11.: *Image sequence of the strip during an actual experiment. The origin, $x = 0$ marks the limit of the glass plate (left side). On each snapshot, the pointed line marks the head of a sliding front x_F. A transition region 2 can be clearly identified between region 1 (where the strip is at rest) and region 3 where the strip is away from the glass plate and uniformly stretched. The deformation front which separates regions 1 and 2 advances towards region 1 as the strip is continuously pulled away.*

The striking feature in the image sequence is the propagation of a front in the direction of the end in contact with the plate. The position of the front x_F is clearly identified as a reduction of the width of the strip resulting from the its elongation in the pulling direction. Indeed, as the elastomer is almost incompressible (Poisson ration close to 0.5) stretching the strip in one direction induces a thinning in the other ones. The propagation of the front is nevertheless not immediate as it only starts after the second image. The front then propagates beyond a certain threshold (its position is indicated by the dashed line in the images). Three different zones can be delimited by following the local width $w(x)$ of the strip.

- In zone 1, for $L_a \geq x \geq x_F$, the strip is not deformed and does not experience any force, this zone is simply adhering to the glass plate.
- Zone 3, is the part of the strip that is away from the plate. The width w_∞ is uniform along

this zone, indicating a constant stress ($w_\infty < w_o$).

- Zone 2, for $x_F \geq x \geq 0$, corresponds to a transition between zones 1 and 3. The width $w(x)$ diminishes gradually along this region from w_o to w_∞. This evolution indicates that the tension on the strip progressively decays from zone 3 to zone 1. Viewing the setup from underneath indicated that the strip is still in contact with the plate in this region. Zone 2 is thus *under friction*.

The position of the sliding front x_F propagates through the strip at a nearly constant velocity towards region 1 as the free end of the strip is continuously pulled away. The strip eventually detaches when the front reaches the end of the zone 1 and the whole strip coils back.

The local deformation of the strip can be qualitatively tracked with spots of acrylic paint sputtered on the elastomer. In the experiment illustrated in figure 3.12(a), a pair of such spots are marked as yellow dots to visualize their displacement (the specimen is pulled upwards in this image sequence). In figure 3.12(b), the superposition of the different images provides "flow lines" that show the inward displacement of the tracers in addition to the displacement in the pulling direction. Although local strains could in theory be inferred from standard image correlation techniques, displacements are in practice very large and the tracers quickly disappear from the field of view. As a consequence we opted for a simpler technique to asses the averaged strain in a section of the strip. This method is discussed in the following section.

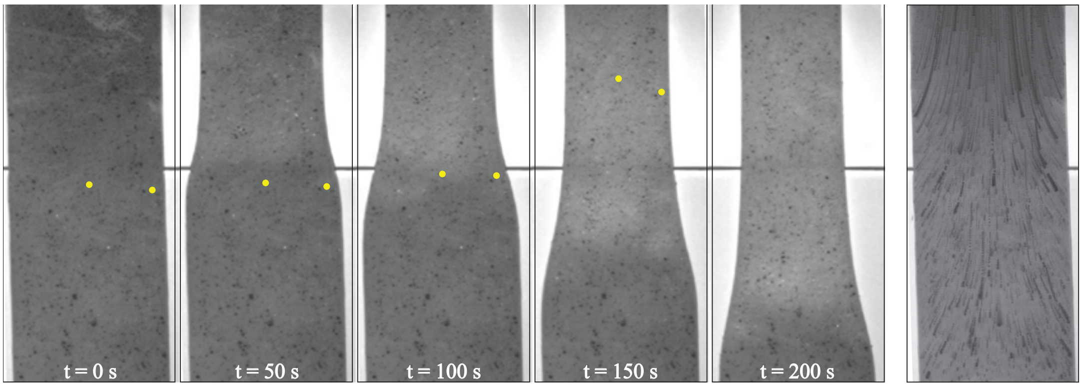

(a) Successive snapshots (b) Superposition

Figure 3.12.: *a) Successive snapshots of the strip during an experiment and b) image superposition. Black spots made with a spray acrylic paint are used to track the strain of the eleastomer. A pair of points of point are marked in yellow (they have left the field of view at* $t = 100\,s$*. The pulling speed is* $v = 100$ *mm/min.*

3.6. Friction stress on the strip

As the deformation of the strip varies, the strip remains in contact with the glass plate, which indicates that the adhering material experiences friction. Moreover, the force leading to the detachment of the tape is fairly proportional to the initial contact area, suggesting a constant friction stress on the order of 20-30 kPa (fig. 3.10). We propose in this section a simple method to estimate directly the shear stress acting on the strip by measuring its lateral deformation.

3.6.1. 1D model

We consider an elastic strip of initial width w_o and thickness h adhering on a rigid substrate over a length L_a (as in fig. 3.7). The deformation profile along the strip is symmetric with respect to the center line on the direction of the pulling force. Zone 1 of the strip is immobile and does not experience any stress. In the opposite side, zone 3 is under uniform horizontal stress, $\sigma_{xx} = F_\infty / w_o h$, where F_∞ is the pulling load.

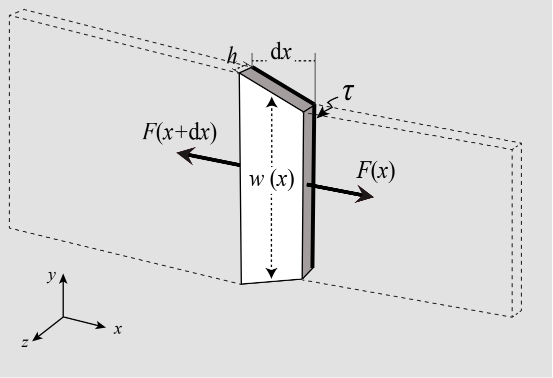

Figure 3.13.: *Force balance on a slice of the strip in zone 2.*

We now consider a transverse slice of the strip in the zone 2, as sketched in figure 3.13. We note x the direction of the pulling force and consider a slice of infinitesimal length dx. We propose to derive a force balance on this slice. As a main assumption, we neglect stresses in the y direction (i.e. $\|\sigma_{yy}\|$ and $\|\sigma_{xy}\| \ll \|\sigma_{xy}\|$). Our qualitative estimate of the strain field with markers indeed indicates that deformations in the y direction are much weaker than the pulling direction.If $F(x)$ is the local force acting on the strip, a simple balance leads in a quasi-static situation to:

$$-F(x + \mathrm{d}x) + F(x) - \tau w \mathrm{d}x = 0$$

where τ is the friction stress averaged in the section of the strip, i.e. $\tau = \langle \sigma_{xz} \rangle_y$. The spatial evolution of the force thus follows:

$$\frac{\partial F(x)}{\partial x} = \tau(x) w(x) \qquad (3.6.1)$$

Calibration.

In order to estimate the local force $F(x)$ from the profile of the width $w(x)$, we use an experimental calibration. This calibration consists in measuring the width of the strip as a pulling load is applied. The local force in then inferred from an interpolation of the calibration curve. This curve can be obtained from a standard tensile test carried separately. However, it can also be obtained directly from an actual lap-test experiment by monitoring the width of the strip w_∞ in zone 3.

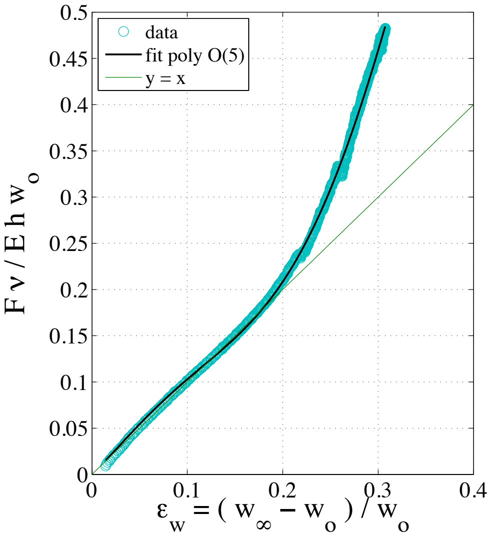

Figure 3.14.: *Calibration curve for the of the non-dimensional force* $\nu F/Ehw_o$ *as a function of the deformation of the width of the strip. The initial linear dependence provides the Young modulus of the material, afterwards used to plot the non-dimensional force (in the current case,* $\nu = 0.5$, $E = 1\,MPa$, $w_o = 60\,mm$ *and* $h = 2\,mm$*).*

In figure 3.14, we present the non-dimensionalized force ($\nu F/Ehw_o$) as a function of the transversal strain (ε_w), which is half the deformation on the x-direction. For moderate transverse strains, up to about a 15%, the elastomer follows a fairly Hookean behavior i.e.

$$\frac{(w - w_o)}{w_o} = \varepsilon_w = -\nu\varepsilon_{xx} = -\nu\frac{\sigma_{xx}}{E} = -\nu\frac{F}{Ehw_o}$$

The polymer then hardens for larger strains. To capture the non-linear response of the polymer, we fit the calibration curve with a Ta 5th order polynomial of the form $ax^5 + bx^4 + cx^3 + dx^2 + x$.

3.6.2. Local measurement of the frictional shear stress.

The local width is measured through a standard edge detection procedure from successive images. An example of the edge detection is shown in figure 3.15, where a typical image is shown superposed with the detected edge points (red dots).
Once we measure the local width of the strip $w(x)$ for a given time, as shown on top in figure 3.16, the local force is computed from a comparison with the calibration curve, (middle plot in the figure). Inputting both measurements into equation B.0.1, we finally obtain the local mean shear stress on the strip, (bottom plot in the figure).The variation of the local friction shear stress displays a *hat*-like shape: its value starts from zero in zone 1, quickly increases to a plateau value in zone 2 and vanishes again in zone 3. The same procedure can be repeated at successive instants of the experiment.

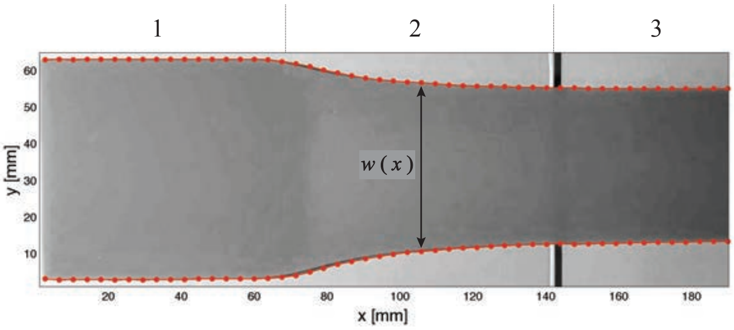

Figure 3.15.: *Edge detection of a strip in order to measure the local width.*

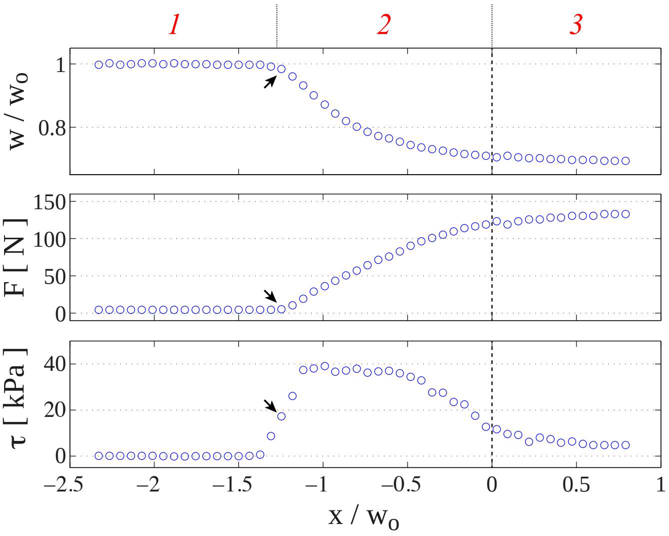

Figure 3.16.: *Measurement of the local width and estimate of the corresponding force and shear stress acting on the strip at a given time. In red, we indicate the corresponding zone 1 (limit signed by an arrow), 2 and 3. Positive x coordinate represents the out of contact part (zone 3), while negative coordinate represent the zones in contact to the glass plate (zone 1 and 2).*

The global evolution of the local measurements is best visualized using space-time diagrams. In figure 3.17, we represent the space-time diagrams for respectively the width, force and shear stress on the strip (from top to bottom). Each horizontal line on the diagram represents the spacial dependence of the local width, force or friction stress at a specific instant. The color bar indicates the amplitude of the displayed quantity. Going up on the figure represents the evolution in time.

- In figure 3.17(a), we present the space-time diagram of the width of the strip. At the first stages of the pulling, we do not observe any deformation in the part of the strip in contact with the plate. However, a front starts propagating progressively beyond a certain time, i.e. beyond a certain pulling load. The black line corresponds to the limit where the strain is 1% of the initial width. We use this line to define the border between zones 1 and 2.

- In figure 3.17(b), we show the local force measured from the variation of the width using the experimental calibration. The force increases progressively in time and spatially as the front advances. In the particular exemple, the The maximal force measured is about 120 N in this sample.

- Figure 3.17(c) corresponds to the friction stress. As the front propagates, we can observe the development of a zone of where the stress $\tau(x,t)$ is nearly constant. For large pulling strains ($t \sim 150\,\mathrm{s}$ in our particular illustration), we nevertheless observe a progressive decrease of τ close to the edge of the plate. In some cases we even observe “waves” in the diagram which are the signature of slick-slip events.

As a preliminary conclusion, a sliding front starts advancing beyond a threshold in the pulling force and the shear stress in the region of friction is nearly constant. The order of magnitude of this stress is 40 kPa for the experiments we conducted, independently from the geometry of the strip and the Young modulus of the elastomer (in a range 400 to 1200 kPa). The value of τ is compatible with our preliminary experiments where we measured the force when the strip detaches. Other studies on friction of elastomers on a flat rigid substrate have also been reported in the literature. Newby *et al.* and Amouroux *et al.* [10, 11] conducted peeling experiments, but with finite peeling angles, larger than 5°, which lead to much smaller strains than in our experiments. The authors report a friction shear stress, measured on direct shear geometries, on the order of the 10-250 kPa, depending on the sliding speed and the viscoelastic properties of the rubber. Chateauminois *et al.* [53] studied a different configuration where a spherical glass lens indents a flat rubber substrate and is then translated. The authors report a friction stress on the order of 100-200 kPa. A more recent variant of this experience is reported by Trejo *et al.* [45], where the lens is rotated. For a smooth lens, the authors also report a friction stress of the order of 100 kPa. Our current interpretation of the sliding front is therefore in good agreement with these other experiments involving the friction of an elastomer with a smooth rigid plate.

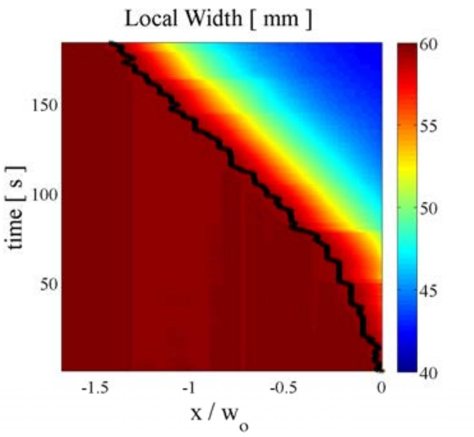

(a) Width

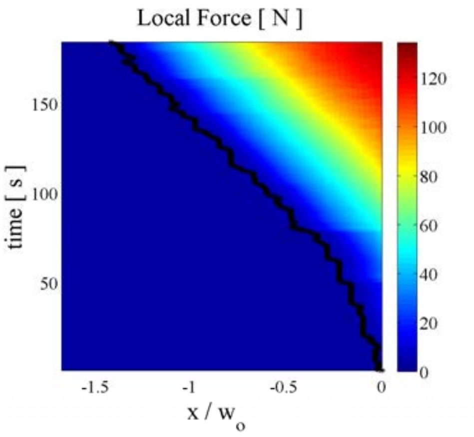

(b) Force

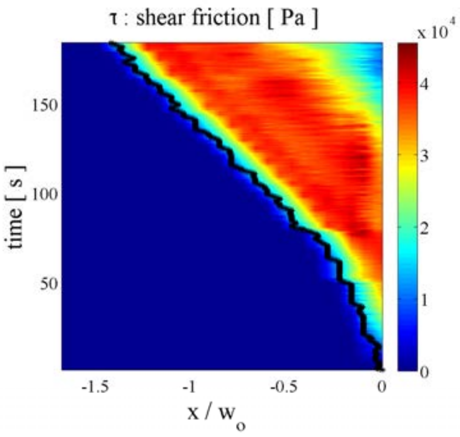

(c) Friction shear stress

Figure 3.17.: *Space-time diagram representing the (a) width, (b) force and (c) friction stress on the strip as its free end is pulled at a constant velocity (v = 0.5 mm/s). The sliding front is represented by a black line, it propagates progressively through the strip towards zone 1. Experimental parameters:* $E = 1055\,kPa$, *h = 2.2 mm and* $w_o = 60\,mm$.

3.6.3. From local friction to the global peeling force

We have seen that the force leading to the detachment of the tape is fairly proportional to the initial contact area, see figure 3.10. In addition, we have observed an almost constant friction stress in the sliding zone. The detachment of the strip finally occurs when the sliding front reaches the final edge of the strip. Beyond the final detachment force, the friction stress τ also dictates the instantaneous evolution of the sliding front. Indeed, the integration of the local friction stress provides the global pulling force, $F_{\text{inf}} = \int_0^{x_F} \tau(x)w(x)\mathrm{d}x$. In the previous section, the friction stress was found to quickly reach a plateau value as the sliding front progresses. Multiplying this plateau value by the contact area should thus provide a good estimate for the force. As a first order approximation, the contact area is equal to $x_F w_o$ with an error below 20%, leading to a pulling force proportional to the displacement of the sliding front.

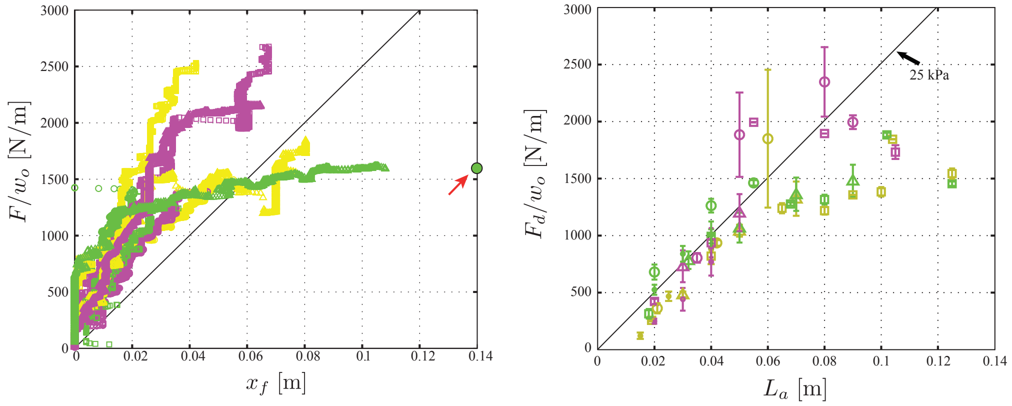

(a) Tensile force per unit length as a function of the displacement of the front.

(b) Detachment force per unit length as a function of the length of the strip initially adhering on the plate.

Figure 3.18.: *(a) Instantaneous applied force normalized by the initial strip width as a function of the position of the detachment front. The pointed green circle in figure 3.18(a) indicates* $x_f = L_a$ *in the corresponding* △ *curve and indicates that the strip detaches before* x_f *reaches* L_a*. (b) Final detachment force normalized by the width of the strip as a function of the initially adhered length. Data in (a) is part of the averaged samples in (b). The legend for both figures is the same as in figure 3.10, except for (b) where curves for* $w_o = 7.5$ *mm are not presented.*

In figure 3.18(a) we represent the instantaneous pulling force per unit length as a function of the position of the front position, i.e. the distance travelled by the sliding front. IThe figure shows the evolution of nine different experiments, where we change the Young modulus (400-1200 kPa) and the width of the strips (15-60 mm), see table 3.3.1. Each curve on figure 3.18(a) corresponds to one point (largest L_a) on figure 3.18(b). However we observed in each experiments that the strip detaches before x_f reaches L_a. As an illustration, the pointed green circle in figure 3.18(a) indicates $x_f = L_a$ in the corresponding curve. We interpret this premature detachment as a consequence of the curvature of the the sliding front. Indeed, the front is in reality not perfectly straight as in our schematic representation from Fig. 3.11 but rather curved. If we compare both figures 3.18(a) and 3.18(b), we observe a similar overall behavior, which suggests that observing the propagation of the front in one experience is equivalent to the collection of the detachment forces. However, the detail of the evolution of the pulling force with the position is in reality more subtle than a linear relation relying on a fixed value of the friction stress:

- We observe a threshold in force below which the front does not move.
- Stick-slip motion of the front is observed for high strains and higher pulling speeds.
- A secondary front can appear, it follows the primary sliding front diminishing the extent of the sliding zone, which leads to the diminution of the friction stress on the contact zone.
- The local shear stress (40-50 kPa) can be higher than the averaged one around 25-30 kPa.

These different points will be discussed in the next section.

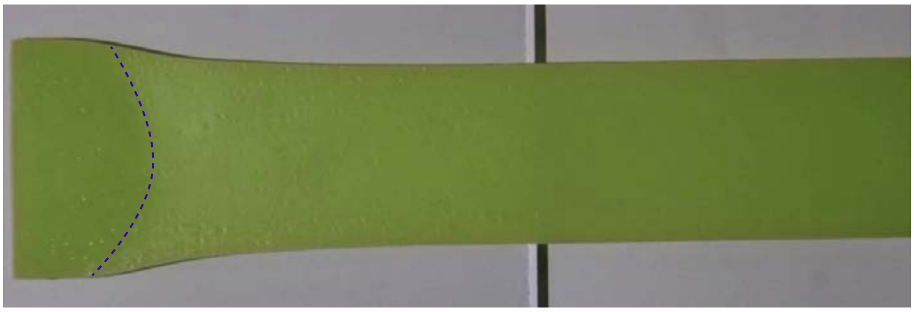

(a) Close view of the friction front emphasizing its curved shape

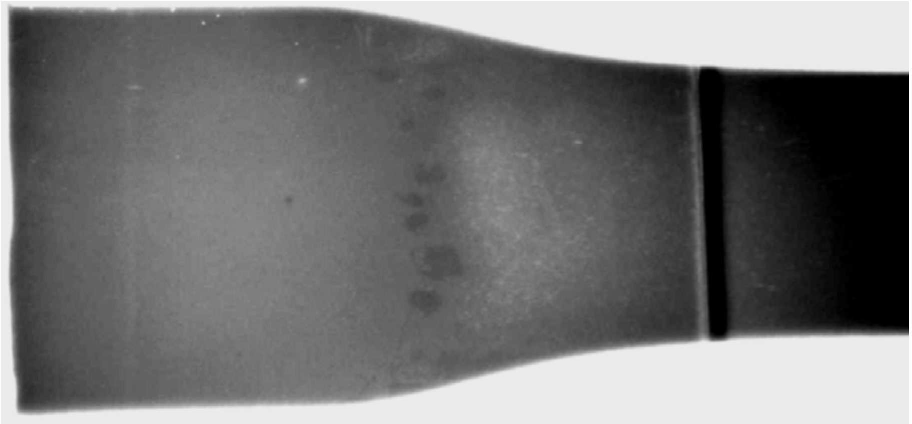

(b) View of the contact of a strip to the glass plate.

Figure 3.19.: *Curved shape of the sliding front. (a) Top view of a strip. (b) View from behind. The darker circular spots close to the sliding front are "air bubbles" in the interface, a similar mechanism to Schallamach waves.*

3.7. Before and beyond steady sliding

3.7.1. Threshold for front propagation

In our experiments, the sliding front is only observed to move beyond a critical pulling force F_{th}, in Fig. 3.18(a). The threshold force is approximately proportional to w_o, which corresponds to a threshold tension F_{th}/w_o on the order of 330 N/m (Fig. 3.20). This threshold is not included in our description involving a sliding front. In our description, the front propagates as soon as a force is applied.

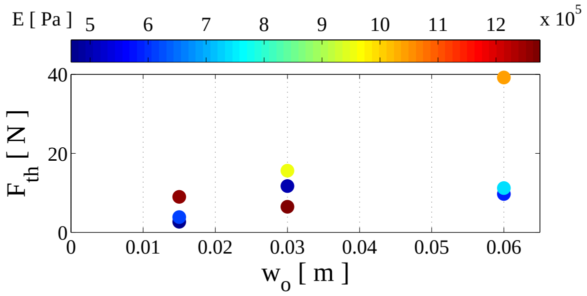

Figure 3.20.: *(a) Threshold force as a function of the width of the strip. The colorbar represents the Young modulus of each sample in units of Pa.*

We examine several possible explanations for this threshold. The threshold force could be intuitively compared with the law predicted by Kendall (eq. 3.2.5), since the strip is not sliding, we may consider this force as a sliding front precursor. However, the numerical estimates of $\sqrt{2Eh\gamma}$ lay within the range 30 to 50 N/m for our configuration (without any numerical prefactor), which does not account for the tension we measure in our experiments.

Another candidate for the threshold would be the product τl of the friction stress with a length scale l. In our simplified approach, the detail of the shear across the thickness of the strip was indeed not considered. However, we expect the strain distribution to evolve from a uniform axial strain to a uniform shear in the vicinity of the edge of the plate. Due to the Laplacian nature of elasticity equations, the length scale involved is set be the thickness of the strip h. Nevertheless, the product τh is in practice on the order of 50 N/m. This value appears too modest, although a numerical prefactor might increase the actual effective length scale.

Two-dimensional effects were finally neglected in our simplified approach. However the sides of the strip tend to slide toward the center line as the strip is stretched. In more pronounced situations this lateral displacement leads to the evolution of the peeling front into a V shape[66]. The coupling of the shear in both directions may also explain the premature detachment of the strip before the friction front reaches L_a. The consequence of such 2D effects would lead to a length scale l proportional to w_o. Numerically the product τw_o varies in the range 300 to 1800 N/m in our experiments, which now tends to be too high. Besides we would then expect a quadratic variation of the critical force with the width, which contradicts our observation (although the actual data is scattered).

To conclude, the detail of the threshold force remains an open question, its value should rely on a combination between the detail of shear strain and 2D effects.

3.7.2. Secondary front and stick slip

At high strains we generally observe that the friction stress is not uniform as in our schematic description. In figure 3.17c, a secondary front for instance develops for $t > 120$ s. The friction stress quickly decreases beyond this front. As a consequence the actual area under friction becomes nearly steady, which leads a plateau of the pulling force. This effect may be the due to a dramatic loss of the friction stress for high stains: the polymer would not “reattach” to the

substrate and would glide with a minor friction stress. We discuss the importance of "adhesion rheology" in the following section.
We also observe sudden jumps of the front as the free end of the strip is pulled steadily. We present in figure 3.21(b) an exemple where such stick-slip events are present for high strains. As the front position jumps ahead, the whole sliding zone is also shifted. In fig. 3.21(b), we present a space-displacement diagram where we show stick-slip. When the traction force (fig. 3.21(a)) shows a jump, at the same instant the sliding front position advances rapidly. As the front position jumps ahead, the whole sliding zone shifts ahead too. Jumps are also observed in the tensile force. However, the average value of the pulling force seem to reach a plateau since the extension of the zone under friction is nearly constant. The observed stick-slip behavior, also noticed by Lake and Stevenson [66] in a peeling configuration, is reminiscent of Schallamach waves [67, 68, 69]. Qualitatively, stick-slip appears for high strains and is very sensitive to small air bubbles trapped between the strip and the plate. We did search for more comprehensive description of the phenomenon. Understanding stick-slip is nevertheless crucial for practical applications since it may lead to a premature detachment of the band.

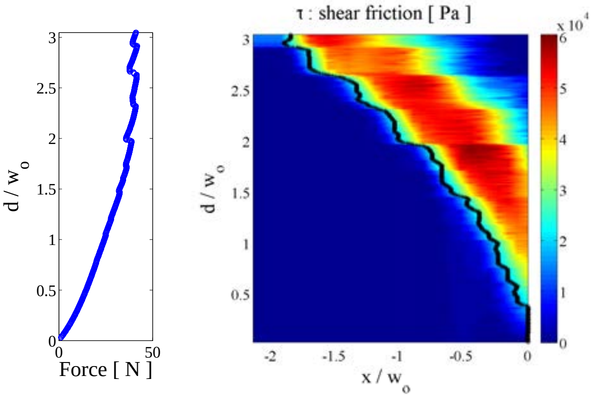

(a) Tensile force (b) Shear Stress

Figure 3.21.: *a) Evolution of the tensile force as a function of the imposed displacement in an experiment displaying stick slip behavior. b) Space-displacement diagram quantifying the corresponding shear stress on a strip, the black line represents the sliding front position. Material parameters of the slample:* $E = 1055\,kPa$, *h = 2.2 mm and* $w_o = 30\,mm$.

3.7.3. Comparison with other experiments.

Towards adhesion rheology?

Although our experimental procedure is very close to the study by Kendall [8], the results are significantly different. Both situations indeed involve the propagation of a front, but the case of Kendall does not include friction, which leads to a steady peeling force even in the limit of a vanishing peeling angle. Conversely, the propagation of a sliding front results into an increasing force in our experiments. If the specimens are long enough, the detachment force is orders of magnitude higher than the prediction by Kendall. Recent experiments conducted with strips of polydimethylsiloxane adhering on glass also involve important frictional dissipation at low peeling angles[52]. Similar large effects of friction for low angles are also observed in our system [70]. However, the reason why frictional dissipation plays a role in some cases and can be neglected in others remains an open question.

The answer probably relies on the different nature of the polymers used in the experiments. Kendall's experiments were performed with vulcanized ethylene propylene rubber while we used Poly Vinyl Siloxane rubber. Although macroscopic Young moduli and adhesion energies (measured with a standard peeling test at 90°) are comparable, the dynamics of adhesion may be totally different. Indeed Kendall's procedure required a contact time of 1h before running a test. The adhesion of PVS on glass seems much faster and our experiments were performed within a few minutes after depositing the polymer on the glass plate. Understanding in detail of the bonding / debonding dynamics would require a specific study at the molecular scale, which would be beyond the scope of the current thesis. However, our observations suggest that the "bonding" time plays a crucial role in friction [71]. We describe in Fig. 3.22 two different schematic scenarios that could represent contradictory situations. If the adhesion dynamics are slow in comparison with the velocity of the imposed displacement, the elastomer may not re-adhere behind the front, which would lead to scenario described by Kendall. Conversely, fast re-adhesion would lead to the important friction we observe in our experiments. Capturing all the ingredients involved in the coupling between friction and adhesion will require additional significant efforts. Nevertheless we hope that our study will motivate further studies in the field.

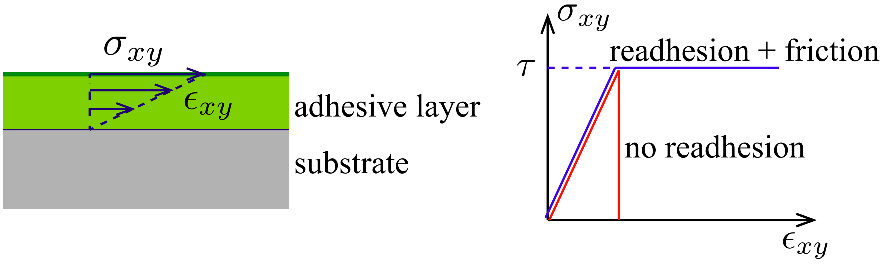

Figure 3.22.: *Simplified models for friction: adhering polymers would resist against shear until a critical shear stress τ and then debond. Although the polymer would still be in apparent contact with the substrate, "slow bonding" polymers (red curve) would not have the time to form new bonds with the substrate. Conversely, "fast bounding" polymers (blue curve) would immediately form new bond, which would lead to a constant friction stress while the adhesive layer is sliding. In a very schematic view both scenarios may represent the system described by Kendall and our situation, respectively.*

From catastrophic debonding to friction

We described in section 3.2 the theoretical transition from steady peeling to catastrophic debonding in the case of a strip coated with a stiffer backing. This transition is related to the finite stiffness of the backing, which results into shear-lag and a corresponding length scale ℓ_{lag} (Eq. 3.2.10). The comparison of ℓ_{lag} with the length of the adhered strip L_a determines which scenario is expected.

In order to probe experimentally this transition, we conducted a series of experiments with two different strips covered with a stiffer backing. These strips were covered with a thin mesh of nylon before curing. The imbibition of the mesh assures its firm anchoring to the strip. The effective stiffness $E_b h_b + Eh$ was measured with a standard traction test and it is of the order of $E_b h_b$ instead of Eh for a plain strip of the same thickness. We verified the condition for shear-lag $Eh \ll E_b h_b$. With strips of thickness $h = 2\,\mathrm{mm}$, we obtained $\ell_{lag} \simeq 20\,\mathrm{mm}$ and $30\,\mathrm{mm}$ for elastomers of $E = 1300$ and 225 kPa, respectively.

We followed the lap-shear procedure described by Crosby and collaborators. Force *vs.* displacement tests were carried on strips adhering over an area $A = L_a w_o$. We measured the critical pulling force F_C and deduced the compliance of the system from the slope of the corresponding curve (see Fig. 3.3(a)). We represent in figure 3.23 the critical load F_C as a function of $\sqrt{A/C}$. We obtain the expected linear dependence between both quantities for short lengths of adhesion (linear fits in the figure, which slopes provide estimates of the debonding). However, we observe a clear transition to a different regime for long strips. In this second regime the maximum load increases in a dramatic manner with a value compatible with friction stresses measured independently with plain strips. Interestingly, we find that the transition occurs for $L_a \simeq 2\ell_{lag}$. The description in terms of shear lag seems thus also relevant to describe the transition from the regime of catastrophic debonding reported by Crobsy *et al.* to a regime dominated by friction, which is the focus of the present study.

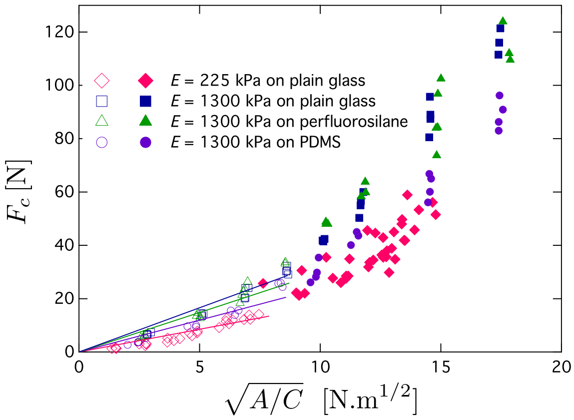

Figure 3.23.: *Experiments with a backing. Critical load F_C as a function of $\sqrt{A/C}$. We observe a transition from catastrophic debonding to the regime dominated by friction as L_a is progressively increased: open symbols $L_a < 2\ell_{lag}$, filled symbols $L_a > 2\ell_{lag}$. In the first regime, F_C is nearly proportional to $\sqrt{A/C}$. The slope of the corresponding linear fits provides an estimate of the shear debonding energy from Eq. 3.2.6.*

3.8. Conclusion

To summarize, the comparison of our experimental results with other studies from the literature put in evidence three different failure modes for a tape adhering on a rigid substrate though molecular interactions.

A first mode involves the coupling between a compliant adhesive and a stiff backing. In this configuration, the whole tape reacts to the load and suddenly detaches if the pulling force exceeds a critical value. This maximum load is proportional to the area of adhesion and to a characteristic stress accounting for both adhesion energy and compliance of the system.

A second mode corresponds to tapes consisting in a single compliant strip with slow adhesion dynamics (and consequently low friction). In this case, the peeling force is steady during the peeling process and exhibits a plateau value as the peeling angle vanishes. This force is proportional to the width of the strip and to a tension accounting for the adhesion energy and the material stretching modulus. A comparison of the shear lag distance ℓ_{lag} to the length of the strip discriminates between this progressive front propagation and the catastrophic debonding.

Our experiments involve a third scenario where friction plays a crucial role in the peeling process. A sliding front propagates along the adhering part of the strip beyond a threshold, as the other end is progressively pulled away. We developed a simple technique based on monitoring the deformation of the strip to estimate the corresponding friction stress. As a crude approximation, the shear stress is uniform and steady in the zone of friction. The global friction force thus increases linearly with the advance of the sliding front. The strip suddenly detaches when the front eventually reaches its end. The order of magnitude of friction stress estimated for the polyvinylsiloxane elastomers used in our experiences, $\tau \sim 30\,\mathrm{kPa}$, is in agreement with measurements from the literature conducted with other silicone rubbers. In the presence of backing, the criterion based on shear-lag is also relevant to describe the transition from catastrophic debonding to a regime dominated by friction. These different scenarios are sketched in Fig. 3.24 where we summarize the expression of the maximal pulling forces shapes of the qualitative shapes of the force *vs.* displacement curves. Although commercial adhesive tapes display more complex behaviors due to the rheology of the adhesive layer [26] or of the plasticity of the backing, the current study should be relevant for designing future soft adhesives.

Several fundamental questions remain open. The origin of the threshold force remains unclear and should be probed systematically in other configurations. In particular, the implication of friction in the propagation of the front remains to be elucidated. This selection may involve dynamics of the adhesion process at a molecular scale or, more macroscopically at the scale of the roughness of the materials. To investigate this last effect, it would be interesting to carry experiments on surfaces with patterned geometries such as pillars[72] or wrinkles[73]. Finally our study has so far focused on the particular lap test configuration. In the next chapter we address the more general case of peeling at finite angle, which is very relevant for practical applications. Is lap-test a singular configuration or does it correspond to the smooth limit of decreasing peeling angles?

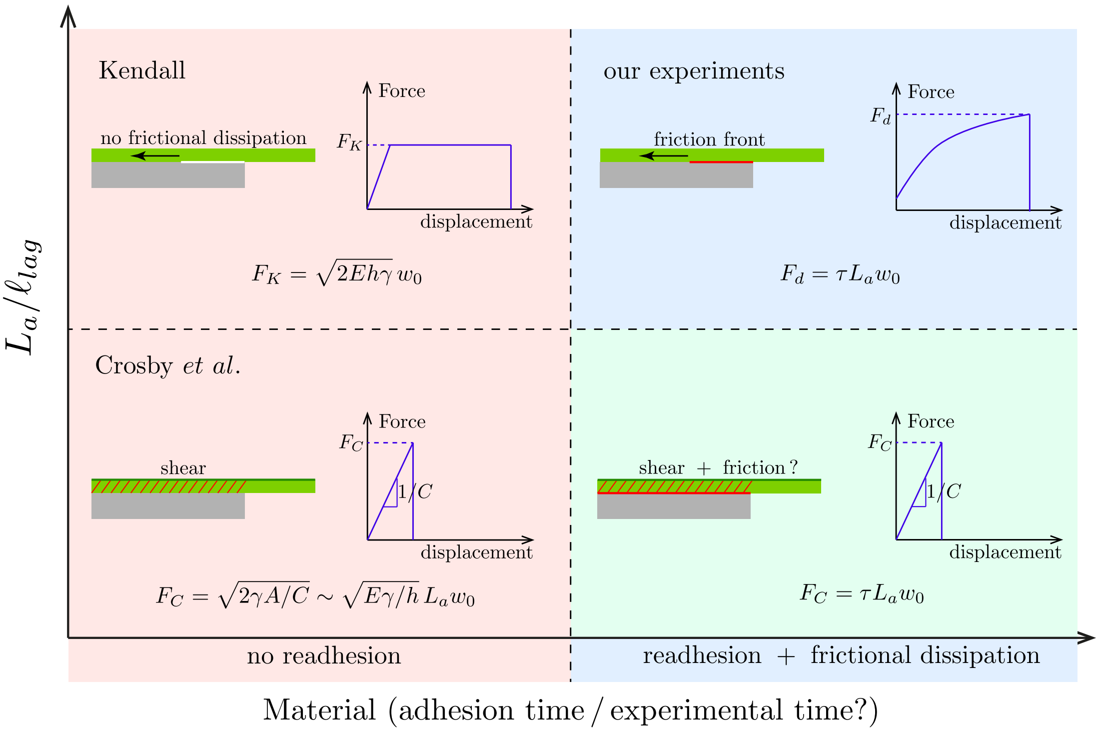

Figure 3.24.: *Schematic view of the different configurations described in this chapter. Depending on the material "adhesion rheology" the stripe may readhere (blue region) or not (red region). As a crude approximation, the first situation leads to a constant friction τ. If the shear-lag length ℓ_{lag} is large in comparison with the adhesion length L_a, a friction front propagates. In the opposite case we would expect the whole strip to slide beyond a critical pulling load (although we did not explore this situation in detail, the band seems in practice to undergo a stick-slip motion. In the second "no readhesion" situation, friction is not considered. If $\ell_{lag} \ll L_a$, we expect a steady peeling front to propagate as in the classical case described by Kendall. In the opposite case studied by Crosby et al., the whole strip is under shear and suddenly detaches beyond a critical load.*

4. Peeling at finite angle

4.1. Introduction

In the previous chapter, we have seen that friction stresses play a dominant role in the adhesion of a strip of elastomer on a planar surface in a lap test geometry: the force does not reach a plateau and the maximum detachment force is proportional to the adhering area. However, this configuration corresponds to a particular case of a peeling test, namely when the peeling angle goes to zero. Conversely, in a peeling experiment at large peeling angle, forces are expected to be constant during the progressive detachment, with a value proportional to the width of the strip (and independent from the adhesion area).

Is the lap-test configuration singular? Can we observe a macroscopic zone under friction for finite peeling angles? If the lap-test is singular, what accuracy do we need in the estimation of the angle to ensure that we are working in this particular configuration?

The sliding of a strip before detachment has been observed in non-zero peeling geometry and the importance of friction in the adhesive properties of elastomers has been mentioned in the literature [9, 10, 11, 52]. Between 1995 and 1998, Newby *et al.* have shown varied evidence of slipping of a polymer layer on the peeling geometry [9, 10]. They proposed that for small peeling angles, energy dissipation relies on two complementary contributions: adhesion (opening or cleavage mode) and friction (shear mode). A little later in 2001, Léger *et al.* [11] studied experimentally the transition between two shear dissipative mechanisms: viscous bulk dissipation and friction through slippage with the surface. In these works, the sliding length has been observed directly by measuring the sliding displacement of fluorescent or colored micro-particles imbibed on the polymer strip very close to the contact surface. Very recent works from McMeeking and coworkers were finally dedicated to the effect of sliding friction on peeling tests [59, 52]. In particular, they observed a strong increase of the peeling force as the peeling angle is diminished. Their theoretical approach follows the main lines drawn by Jagota and Hui for the case of small strain [74]. We will use the same theoretical framework to interpret the experiments described in this chapter.

The sliding displacement, as well the sliding length, reported in the mentioned works are on the order or smaller than the thickness of peeled strip. In the following sections, we wish to study the peeling process of a purely elastic material that is submitted to friction with a rigid surface. We propose to investigate the evolution of the peeling force from large to low angles and the transition to the zero angle case studied in the previous chapter. We wish to put in evidence a sliding length larger than the thickness of the peeled strip. We first describe our experimental setup and our observations. We will then present a model for peeling including friction, which relies on the friction stress τ that we observed in the previous chapter.

4.2. Experimental setup

We start by presenting our experimental setup for peeling at a constant angle θ, and the processing for the force and angle measurement.

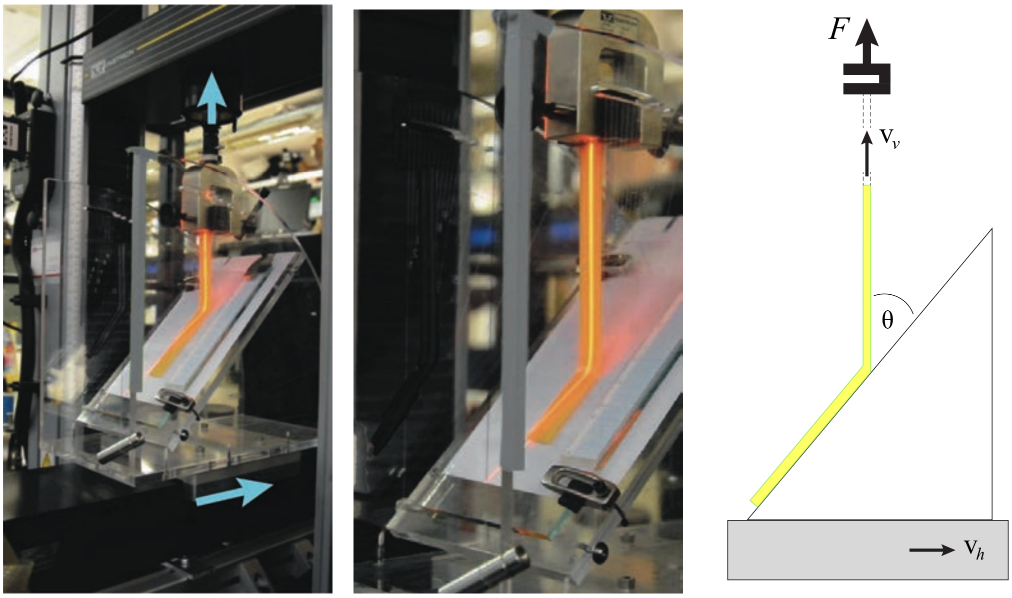

(a) Experimental setup (b) Close-up (c) Sketch

Figure 4.1.: *Global views of the experiment illustrate the system to adjust the angle and the horizontal and vertical displacement machines. (a) The sky-blue arrows show the displacement directions imposed. (b) The red line on top of the strip is the reflection of a laser line to measure the peeling angle. (c) Sketch showing the force captor position and the directions of the displacement at speed* v_h *and* v_v.

4.2.1. Description of the setup

We used the same type of silicone strips described in the previous chapter. However, the mechanical system was significantly modified to impose a fixed non-zero peeling angle. An additional support was built in poly-methyl-methacrylate. Besides being transparent, PMMA is very convenient as it can be easily machined through laser cutting. The setup consists of a plate attached to a pair of parallel quadrants where the angles have been engraved, as shown in figures 4.1 a and b. The support of the quadrant can be translated horizontally with a 1 - axis stage Newport ESP-301. To control the vertical displacement and to measure the tensile force $F(t)$ at every instant, we used the same Instron 5865 force-displacement machine as in the previous chapter, see figure 4.1(c). Before starting an experiment, a portion of the strip is deposited on a glass plate which is attached to the quadrant support. The peeling experiment begins after a waiting time on the order of 5 min.

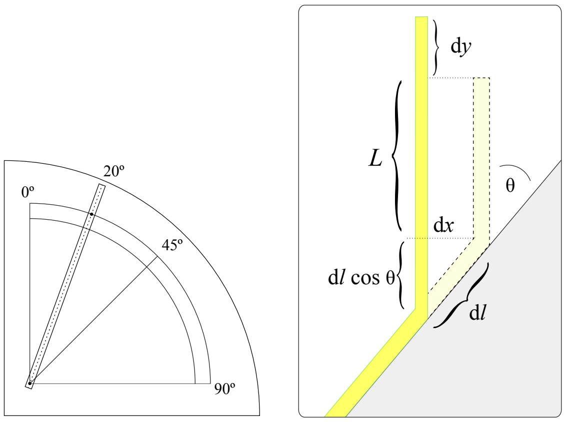

(a) Quadrant (b) Velocity components

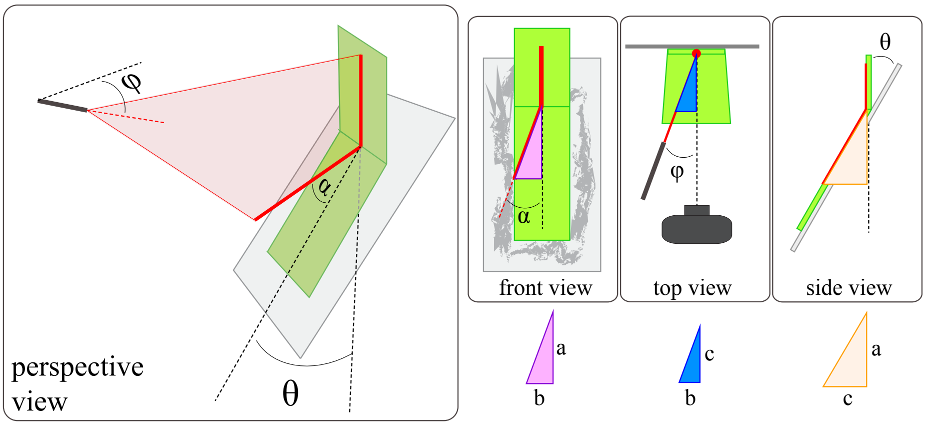

(c) Angle monitoring

Figure 4.2.: *(a) Sketch of the quadrant and supporting plate. (b) Sketch to determine the vertical and horizontal displacements. (c) Sketchs showing three different views of the setup to explain the method to measure the peeling angle.*

4.2.2. Controlling the peeling velocity: horizontal and vertical displacements

To impose the peeling speed, we need to control simultaneously the vertical tensile velocity as well the horizontal velocity of the support. The vertical velocity was imposed by the traction machine, whereas the horizontal component was controlled by a displacement stage. Both velocity components were determined by considering the actual speed of the peeling front during the process and the deformation of the strip.

We consider the evolution of the strip during a time interval dt, as shown in figure 4.2(b). During that interval, the strip detaches over a distance dl along the rigid plate, which is inclined at an angle θ. The actual detachment velocity is $v_C = \frac{\mathrm{d}l}{\mathrm{d}t}$, its horizontal and vertical components are v_h and v_v respectively. Then, $v_h = \frac{\mathrm{d}x}{\mathrm{d}t}$ and $v_v = \frac{\mathrm{d}y}{\mathrm{d}t}$, as sketched in figure 4.2(b).

The horizontal displacement is simply $\mathrm{d}x = \mathrm{d}l \sin\theta$. However, the vertical displacement dy of the clamped end of the strip cannot be directly determined since the strip is extensible. If the total length of the detached strip is initially L, an extra length dl gets detached during dt. Taking into account the extension of the strip, we obtain

$$L(1+\mathrm{d}\varepsilon)+\mathrm{d}l(1+\varepsilon)=L+\mathrm{d}y+\mathrm{d}l\cos\theta.$$

The vertical displacement of the machine thus verifies $\mathrm{d}y=L\mathrm{d}\varepsilon+\mathrm{d}l(1+\varepsilon-\cos\theta)$. We consider here a steady regime where the pulling force, and therefore ε, are constant, which leads to the following components of the velocity:

$$v_h = v_C \sin\theta \tag{4.2.1}$$

$$v_v = v_C(1+\varepsilon-\cos\theta) \tag{4.2.2}$$

It is easy to set v_h and v_v in the case of an inextensible strip or when $\varepsilon \ll 1$. However, if the peeling angle $\theta \to 0$, this additional term becomes dominant and we would need to know ε or F in advance, before being actually able to measure it. In order to set the vertical velocity, we compute the strain ε as a guess from the value predicted by our model, which we will described in the section 4.4.

4.2.3. Monitoring the peeling angle

In practice it is difficult to be sure that the angle obtained with a given inclination and the set of velocities is exactly the one we aimed. In order to monitor the actual peeling angle, we take pictures in front of the setup, aligning the camera to the horizontal axis of the imposed displacement. A vertical laser sheet is positioned in front of the peeled strip. To measure the peeling angle we used three characteristic angles that have a geometrical relation that we now describe. These angles are sketched in figure 4.3(a) and 4.2(c) respectively.

First of all, the laser sheet has to be oriented vertically. Its plane forms an angle φ with respect to the axis of the camera in front of the strip. Then, looking from the position of the camera, the laser line forms an angle α with respect to the vertical. Finally, the angle we want to determine is θ, i.e. the actual peeling angle of the strip with respect to the glass plate.

In the right side bottom of figure 4.2(c), we show three triangles which represent the projection of a laser line over three planes. From the front view, we obtain the relation $\tan\alpha = b/a$. From top view, we observe $\tan\varphi = b/c$. And finally, from side view, $\tan\theta = c/a$.

These geometrical relations finally lead to:

$$\tan\theta = \frac{\tan\alpha}{\tan\varphi}$$

In general, we choose $\varphi = 45^\circ$ so the measured angle on the images is the same as the peeling angle. For small peeling angle, the idea is to amplify the angle on the image α, to make it easier to measure. Then, we choose larger φ angles, since the amplification factor is $\tan\varphi$.

During an experiment, the peeling angle keeps a fairly constant value, see figure 4.3(b). We show in red the angle measured on the images α and in blue the peeling angle θ (amplification of α). In this case, the measured peeling angle is 15°, while the angle we fixed on the quadrant was 10°. Ideally, they should be the same, but it is not actually the case. Indeed, the detached part of the strip is not completely vertical. In conclusion, these experimental constraints confirm that it is necessary to monitor the peeling angle during an experiment, because it is not exactly the same that we aim.

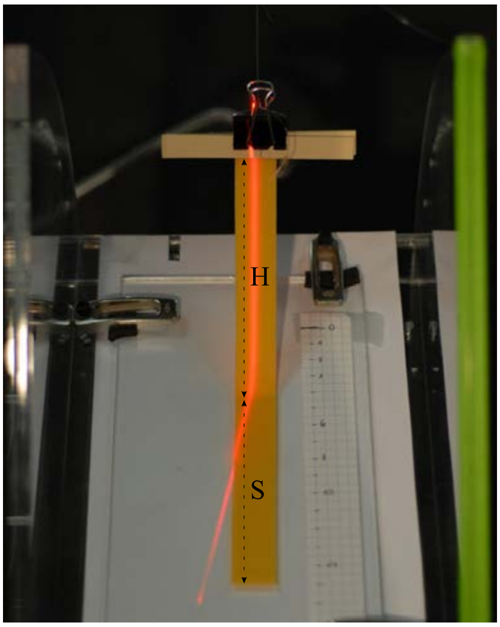

(a) Experimental front view, with $\theta = 45^{\circ}$

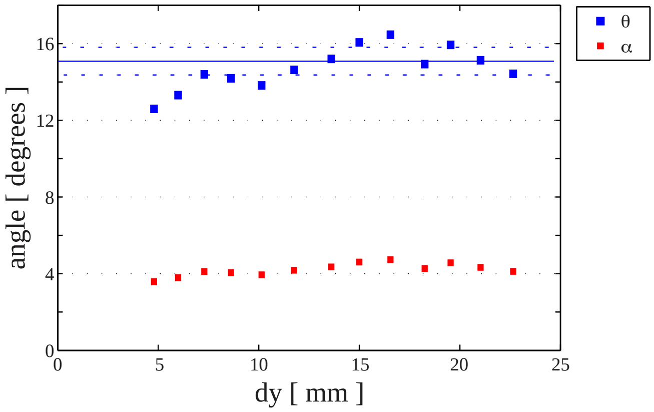

(b) Experimental measure of the peeling angle

Figure 4.3.: *(a) Experimental image showing a strip being peeled from a 45° inclined glass plate. The red line is the reflection of a vertical laser sheet which is used to determine the peeling angle. (b) Measure of the angle α (red) and θ (blue) during a peeling experiment as a function of the imposed vertical displacement. Here, $\varphi = 15.4^{\circ}$. The solid line is the mean value during the experiment and the dashed lines represent the standard deviation from the mean.*

4.2.4. Renormalization of the force: taking weight out

In the experiment we observe that the weight of the strip (around 80 mN, for the 1 mm thick strips) is not negligible when the measured force F_m is weak (around 30-100 mN, for larger peeling angles). We need to compute the equivalent peeling force f_{pl} that the operator would apply in absence of gravity. This requires to compensate the weight of the strip in the measurements, a procedure that is complicated by the fact that the strip undergoes stretching and bending. An intuitive approach is to consider that the operator must apply the peeling force plus the weight of the hanging strip. However, the distribution of weight of the bending region near the peeling front remains ambiguous : does this bent part hang from the clamp, or is it rather supported by the substrate plane?

In the following, we have used a procedure that allows us to estimate the weight from distances measured on pictures. This procedure does not rely on any additional assumption, other than that of steady peeling.

A general procedure to compensate for gravity

In this approach, we compute the additional work done by gravity during the detachment of the strip by a distance dl that has to be added in the energy balance used before (equation **??**). We note l the debonded distance, H the height of the operator's clamp above the peeling point. The non-deformed width and thickness of the strip are w_o and h and ρ is the mass density in the rest state.

We repeat the energy balance of section 2.3.2 with this extra effect. The operator applies a force F_m which works on a distance $(1-\cos\theta+\varepsilon_m)\mathrm{d}l$, where ε_m is the strain in the detached part of the strip, close to the attachment of the strip $\varepsilon_m = F_m/Ehw_o$. The corresponding work is $F_m(1-\cos\theta+\varepsilon_m)\mathrm{d}l$. On the other hand, the variation of elastic energy is $d\mathscr{E}_{el} = Eh\varepsilon_m^2 w_o\,\mathrm{d}l/2$. This is the energy of a portion of length dl of strip initially attached and now submitted to a strain ε_m.

We now compute the variation of gravitational potential energy, which can be decomposed into two terms. First, the part of the strip that was initially detached has moved down parallel to the substrate, as illustrated in figure 4.4(a). This rigid displacement lowers the potential energy by $d\mathscr{E}_1 = -\rho g l w_o h\,\mathrm{d}l\cos\theta$. Second, there is an increase of potential energy due to lifting up the additional length dl by a distance H: $d\mathscr{E}_2 = \rho g h w_o \mathrm{d}l\; H$. With those considerations the total variation of potential energy is

$$d\mathscr{E}_{grav} = d\mathscr{E}_1 + d\mathscr{E}_2 = \rho g h w_o\,(H - l\cos\theta)\,\mathrm{d}l.$$

Finally, we are led to the following expression for the energy release rate G,

$$\frac{1}{2}\frac{F_m^2}{Ehw_o} + F_m(1-\cos\theta) - \rho g h w_o g(H - l\cos\theta) = Gw_o \tag{4.2.3}$$

We are interested in the force f_{pl} that would provide the same energy release rate in absence of gravity. Using equation 2.3.3, we find that the equivalent force reads

$$f_{pl} = Ehw_o\left[\sqrt{(1-\cos\theta)^2 + 2G/Eh} - (1-\cos\theta)\right] \tag{4.2.4}$$

In a infinitely flexible strip, an easier procedure to compensate gravity

It is instructive to study the particular case of vanishing bending rigidity: the strip has initial non-stretched length l, it remains straight but now undergoes gravitational and tensional loads, so that its final length is H. Indeed, the stress distribution is $\sigma = \rho g(z-l) + F/hw_o$, where z is a coordinate along the strip. It leads to the vertical displacement $u(z) = \rho g[(z-l)^2 - l^2]/2E + Fz/Ehw_o$, so that

$$H = u(z=l) + l = l - \rho g l^2/2E + Fl/Ehw_o$$

within this assumption, we input the last expression in equation (4.2.3), and we find

$$F_m^2/2Ehw_o + F_m(1-\cos\theta) - \rho g h w_o l(1-\cos\theta + F/Ehw_o - \rho g l/2E) = Gw_o$$

which can also be rewritten into

$$(F_m - \rho g l h w_o)^2/2Ehw_o + (F_m - \rho g l h w_o)(1-\cos\theta) = G, \qquad (4.2.5)$$

We recover in this limit the intuitive idea that the equivalent peeling force f_{pl} is the one acting close to the detachment front. The measured force $F_m = f_{pl} + Mg$ is in this case increased by the mass $M = \rho w_o h l$ of the detached strip that has to be lifted up.

Experimental procedure

We chose to use the most general treatment to compensate for gravity. In practice the experimental data are treated using analysis of images synchronized with the measurements of the force.[1] On several images (see figure 4.3(a)) we measure the apparent detached and adhering lengths H and the apparent distance S. It is easy to deduce the actual detached length l from these geometrical quantities. Since we know that in steady peeling l and H increase linearly with time, it suffices to determine it in a finite number of images to interpolate their value for all time.

In figure 4.4(b), we show the actual measured force (in blue) and the renormalized force f_{pl} (in red) for a $\theta = 90°$ test. The first term of equation 4.2.3 can be neglected since the deformation of the strip is practically zero. We also observe that the measured force increases monotonically as the detached weight increases progressively. Looking at the renormalized force, after a first transient time, the force reaches its *plateau* value (marked with darker points over the red curve).

The adhesion energy was measured for each sample using this method in a standard 90° peeling test [63] carried at a velocity of around 0.1 mm/s with an Instron 5865 force-displacement machine. Depending on the elastic modulus and the peeling speed, the adhesion energy[2] γ could vary between 0.5 and 1.5 J/m^2. We did not see a clear correlation between the Young modulus E of the sample and its adhesion energy. We expect the adhesion energy to depend on the peeling velocity due to viscoelastic effects. However, we kept the peeling velocity approximately constant to avoid such influence.

---

[1] We define the zero reference force when there is nothing attached to the traction machine.

[2] We also measure the work of adhesion by a splitting test at rest [64, 65], $w_{ad} \sim 0.05 - 0.5$ J/m^2.

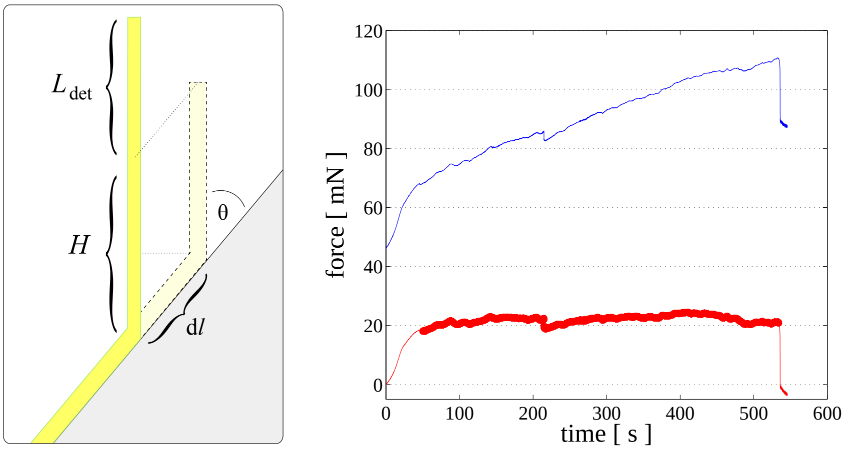

(a) Schema potential energy

(b) Measured force + *plateau* force, $\theta = 90°$

Figure 4.4.: *(a) Sketch illustrating the effective displacement of the strip as a portion of length dl is detached from the substrate. (b) Peeling force measured as a function of time: E = 250 kPa,* w_o *=29.5 mm , h = 1.2 mm. Here,* $f_{pl} = 19 \pm 1$ *mN, so* $G(90°) \equiv \gamma$ *= 0.64 J/m*^{2}.

4.3. Experimental observations

4.3.1. Force measurements

As it was described on the previous section 4.2.4, once the force is corrected by removing the weight of the strip, a *plateau* force is observed. In figure 4.4(b), a peeling force curve measured as a function of time for $\theta = 90°$ is presented. Here, $f_{pl} = 19 \pm 1$ mN, so $G(90°) \equiv \gamma = 0.64 \pm 0.03$ J/m^2.

In figure 4.5(a), an example of force-displacement curve for a large angle is shown. The measured *plateau* force is $F_{pl} = 56 \pm 6$ mN, for $\theta = 45°$. This corresponds to an energy release rate $G = 0.58$ J/m^2. At comparing the energy release rate at 45° and at 90°, we observe that $G(45°) \approx \gamma$, this means that most of the dissipation at 45° is also due to adhesion, in agreement with the seminal work from Kaelble [62].

We now focus on lower peeling angles. On figure 4.5(b) we present a force-displacement curve for the same sample at a low angle equal to 3°. The mean *plateau* force is $F_{pl} = 5.64 \pm 0.06$N. This force corresponds to an energy release rate of $G = 61$ J/m^2, Which is more than a hundred times the adhesion energy $(G \sim 100\gamma)$! This indicates the existence of a form of energy dissipation which is not the same as the adhesion energy obtained at large peeling angles.

To gain further insight, we measured the mean plateau force as a function of the peeling angle. In figure 4.6, we present the data obtained by varying the peeling angle for the previous sample. In blue, we show our data, the error bars are measured as the standard deviation of the force and angle measured during every peeling test. In red, we show the force predicted by equation 2.3.3, which converges to a value of around 0.6 N for small angles. Clearly, we can see that the theoretical prediction does not correspond to our data for peeling angles smaller than $\theta \approx 10° - 20°$. Indeed, the peeling force to detach the strip is much larger than the theoretical prediction (around 100 times larger). It can also be seen that the difference between the observed value and the predicted one increases as the peeling angle decreases.

These observations are consistent with the fact that there is an extra dissipative effect to take

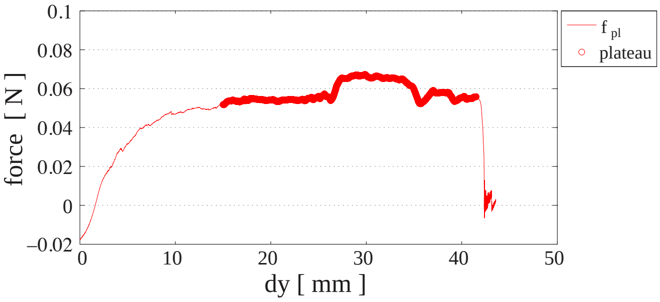

(a) Force plateau, $\theta = 45^\circ$, $F_{pl} = 0.056 \pm 0.006$ N.

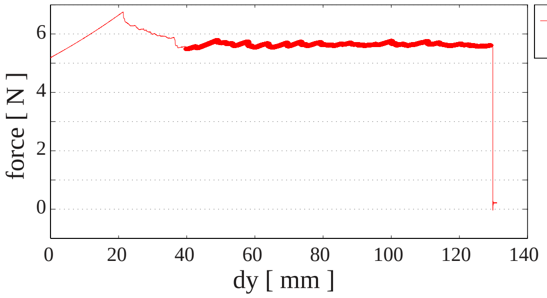

(b) Force plateau, $\theta = 3^\circ$, $F_{pl} = 5.64 \pm 0.06$ N.

Figure 4.5.: *Plateau force for two different angles (a) 45° and (b) 3°. Note that the force for 3° is two order of magnitude higher than the force for a smaller angle. Sample parameters:* $h = 1.2\,mm$, $w_o = 29.5\,mm$, $E = 250\,kPa$ *and* $\gamma = 0.6\,J/m^2$.

into account. This effect, which begins to be observable for angles smaller than about 15°, increases as the peeling angle approaches to zero. We propose that this effect is due to sliding friction, following the same mechanism we described on the previous chapter 3.

Moreover, the peeling force seems to diverge as the peeling angle vanishes. We can now interpret the results shown in the previous chapter, considering that the diverging peeling force (in the lap-shear limit) corresponds to an infinite value for the plateau force. As we have seen, the force remains bounded by the finite length of the strip, and a sudden detachment occurs, for a force proportional to the initially adhered area. The infinite plateau force would require an infinite strip to be attained. For longer strips than we have tested, the material eventually reaches its fracture strain, which is another bound for the detachment force.

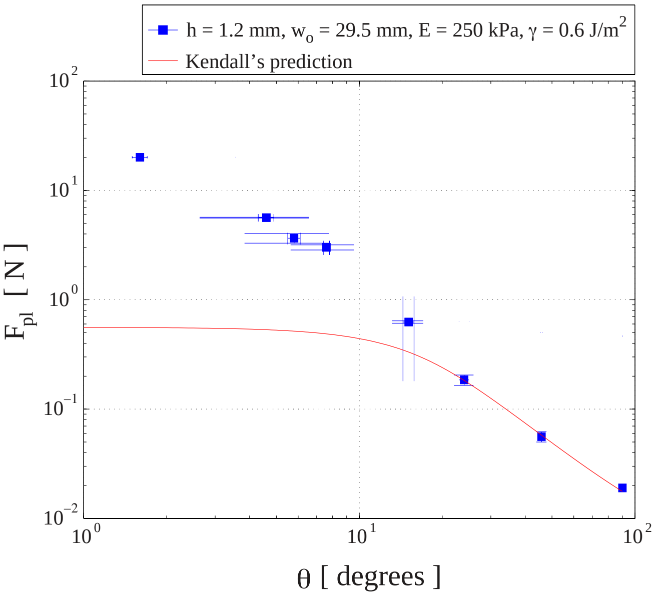

Figure 4.6.: *Steady peeling force for a typical strip, measured for different angles and compared to Kendall's theoretical prediction. Sample parameters:* h = *1.2 mm,* w_o = *29.5 mm,* E = *250 kPa and* γ = *0.6 J/m*^{2}.

4.3.2. Sliding area and frictional force

Interesting information about friction can be obtained by observing the shape of the strip during peeling off a glass plate. In figure 4.7(a), we show a close up view of four consecutive images of an experiment. The adhering part of the strip is dark purple, while the detached part is lighter in color. This color change is not a shading effect, but is due to the thickness thinning of the strip. Indeed in the detached area, the strip undergoes larges strains $\varepsilon_\infty = \frac{F_{pl}}{Eh_o w_o}$, and Poisson effect reduces the thickness, whereas in the adhering region far from the detachment front, we expect the strip to be in its rest state. The thinning is best observed by studying the interceptionof the laser with the strip: the red laser line is more inclined in an intermediate zone close to the detachment front in comparison to the completely adhered and the completely detached parts. This is because in the intermediate zone the strip exhibits a gradient of deformation. As we have seen before, this gradient of deformation is the signal of friction stress with the glass substrate. The length of this intermediate zone will be called frictional length.

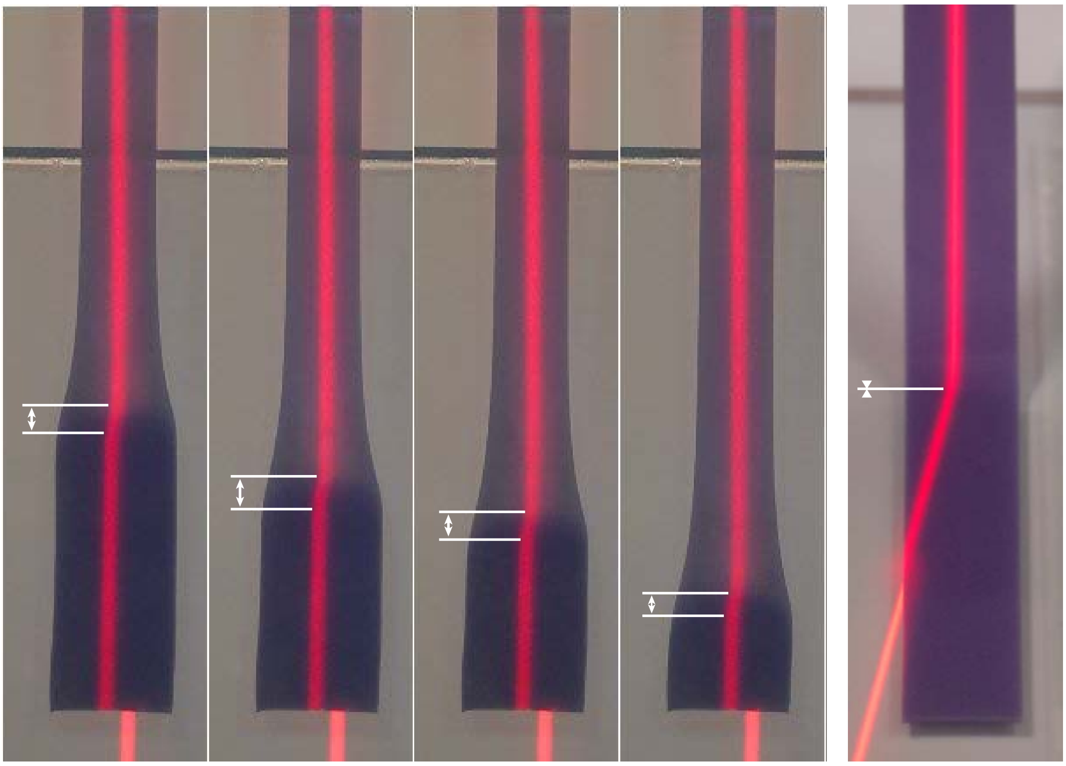

(a) $\theta = 1^\circ$

(b) $\theta = 45^\circ$

Figure 4.7.: *(a) Sequence of four experimental images of a strip peeled off at 1°. (b) An experimental image of the same strip peeled off at 45°. The red line is the reflexion of the laser sheet and the white arrows show what we consider as the sliding length. Sample parameters:* $h = 1.2\,mm$, $w_o = 24\,mm$, $E = 545\,kPa$ *and* γ *= 1.09 J/m*^{2}.

We note that the frictional length (indicated by white arrows) is nearly constant in the four images of 4.7(a), which is consistent with a steady-state peeling condition. In figure 4.7(b), we show an experimental image of the same strip but with a large peeling angle $\theta = 45^\circ$. In this case the frictional length is minute, since the slope change is observed to occurs through a kinking point. If frictional stress τ is at play in this zone of extension l, we expect the following balance of force parallel to the substrate :

$$F\cos\theta = \tau w_o l,$$

where F is the peeling force. Note that we have assumed that adhesion only contributes to forces perpendicular to the substrate plane. In figure 4.8, we present the component of the peeling force parallel to the substrate as a function of the frictional area $w_0 l$, using the trace of the laser sheet to measure precisely the actual peeling angle. We observe a linear dependence with a prefactor $\tau \simeq 40\,\mathrm{kPa}$, which is consistent with the other estimates obtained in the lap-test configuration, described in previous chapter. Going back to the example in figure 4.7(b), we see that the very small frictional length was due to a very law peeling force F for such large angle.

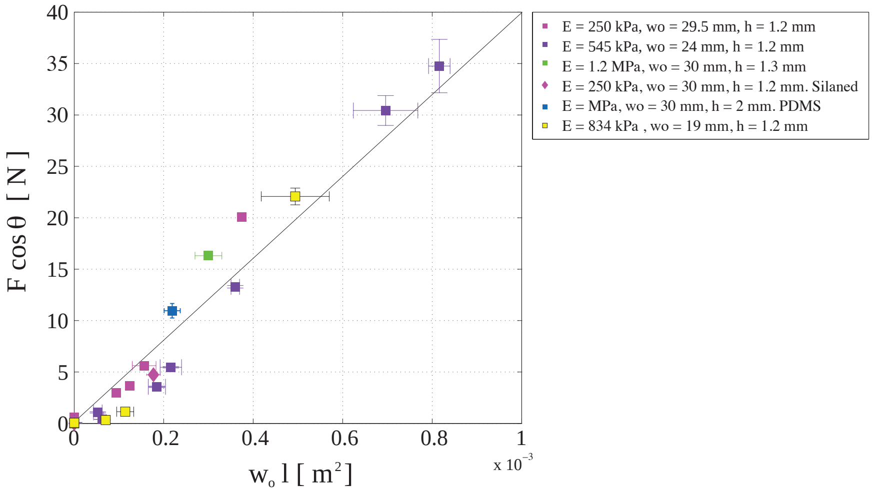

Figure 4.8.: *Horizontal component of the force as a function of the friction area. The black line represents a linear regression, which slope corresponds to* $\tau = 40$ *kPa.*

The distance l along which frictional stresses are distributed should in principle be divided in two parts :

1. Starting from the adhered part towards the detachment point, we expect the shearing frictional stress to build up exponentially with a characteristic length ℓ_{lag}. This is the shear-lag zone that we have already described in previous chapter. Note that in this part, shearing frictional stresses are still low and there is no sliding (and therefore no frictional dissipation). However, this zone of shear-lag contributes to a horizontal force on the order of $\sim w_0\tau\ell_{lag}$, where the shear-lag length ℓ_{lag} is fixed by geometry and material properties of the strip (Eq. 3.2.10). We deduce that there is a maximal horizontal force $w_0\tau\ell_{lag}$ above which sliding should occur.

2. In this case, the shear-lag zone is followed by a sliding zone of extension ℓ where the strip moves relatively to the substrate. The tangential stress is equal to τ in this region. The strip undergoes in-plane tension with gradually increasing intensity towards the detachment front. In contrast with the sliding length, the friction ℓ does depend on the loading and may be null. This sliding zone has already been evidenced in the peeling

geometry [10, 11, 52]. In our case it becomes very large and is observable to the naked eye.

In the case of a strip composed of a single material as we used in our experiments, we expect $\ell_{lag} \sim h$, while the frictional length is in many cases much larger. We therefore consider that the frictional length is almost equal to the sliding length ($\ell \gg \ell_{lag}$, leading to $l = (\ell + \ell_{lag}) \sim \ell$. Within this limit, we expect: $F\cos\theta \sim \tau w_0 \ell$.

Although the results in figure 4.8 are rather convincing, they only support the fact that the component of the peeling force parallel to the substrate is balanced by frictional stresses on the glass plate. This argument does not provide a prediction of the peeling force, which is the focus of the next section.

4.4. Peeling model for adhesion with friction

In the absence of friction (i.e. $\ell = 0$) we expect the peeling force to follow the law derived by Kendall (eq. 2.3.3), which does not account for any frictional dissipation. In this section we focus on the opposite case where a friction front is present behind the peeling front. In fact, the importance of frictional sliding in the adhesive properties of elastomers has already been put in evidence in previous studies [10, 11]. This effect was phrased as *Friction in Adhesion*. Chaudury *et al.* proposed that for small peeling angles, energy dissipation relies on two complementary contributions: adhesion (opening or cleavage mode) and friction (shear mode).

Inspired by these pioneering works, we propose to develop an analytical model that accounts for these two ingredients and would predict the peeling force as a function of the angle. As a simplifying approximation we first consider a small strain approximation with linear elasticity. We will then generalize our results to the more general situation of a non-linear elastic material.

4.4.1. Small strain approximation

To simplify our description we first consider a linearly elastic strip. The free end of the strip is pulled at a fixed peeling angle as in our experiments and we assume that the steady state has been reached. Following our experimental observations, we consider that a sliding zone is present behind the peeling front as sketched in figure 4.9.

With the light of the previous chapter, we assume that the sliding zone has a characteristic length of size ℓ and the frictional sliding results in a constant shear stress τ. Note that we neglect here the shear-lag zone, i.e. we assume $\ell_{lag} \ll \ell$. In a steady regime, we consider that a sliding front (x_f) propagates along the strip together with the detachment front. The distance ℓ between the two front tips is thus constant.

The strain before the sliding front position is null and is constant after detachment, $\varepsilon_\infty = \frac{F}{Ehw_o}$, see bottom figure 4.9. In the sliding zone, the stress is given by the force balance equation

$$h\frac{\partial \sigma}{\partial x} = \tau,$$

where $\sigma = E\varepsilon$. After integrating the last equation, we obtain $\varepsilon = \tau\frac{(x - x_f)}{Eh}$. Therefore, the strain

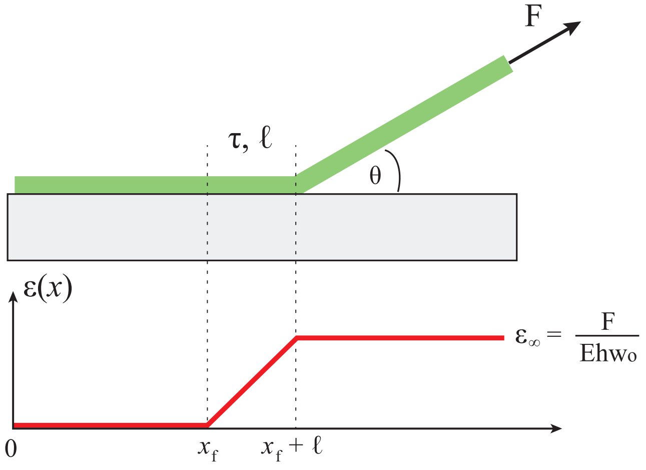

Figure 4.9.: *Sketch showing the strain distribution along the strip during a peeling experiments.*

in the sliding zone is proportional to the shear stress and increases linearly from zero to ε_∞,

$$\varepsilon(x) = \begin{cases} 0\,, & \text{for} \quad x \leq x_\mathrm{f}\,, \\ \frac{\tau(x-x_\mathrm{f})}{Eh}\,, & \text{for} \quad x_\mathrm{f} \geq x \leq x_\mathrm{f}+\ell \\ \frac{F}{Ehw_o}\,, & \text{for} \quad x \geq x_\mathrm{f}+\ell\,. \end{cases} \tag{4.4.1}$$

In order to compute the dissipated energy by sliding friction, we need to estimate the displacement of the material over the surface. We know that for small displacements $\varepsilon = \frac{\partial u}{\partial x}$, which leads to

$$u(x) = \int_0^x \frac{\tau(x-x_\mathrm{f})}{Eh}\mathrm{d}x = \frac{\tau}{Eh}\left(\frac{x^2}{2} - x x_\mathrm{f} + \frac{x_\mathrm{f}^2}{2}\right) \tag{4.4.2}$$

In a steady regime, the extension of the sliding region is constant. The friction front of coordinate x_f thus moves in the same way as the peeling front localized at $x_d = \ell + x_f$. As a consequence, a variation of the position of the sliding front δx_f will lead to a displacement of a material point on the strip $\delta u = -\frac{\tau(x-x_\mathrm{f})}{Eh}\,\delta x_f$. The energy dissipated by friction is therefore:

$$d\mathscr{E}_{fr} = -\int_{x_\mathrm{f}}^{x_\mathrm{f}+\ell} \delta u\, \tau w_o \mathrm{d}x = -\frac{\tau^2 w_o}{Eh}\frac{\ell^2}{2}\delta x_\mathrm{f} \tag{4.4.3}$$

This dissipated energy corresponds to a shear mode energy release rate component. As a result, the total energy dissipation rate can be expressed in terms of the friction shear stress τ, the characteristic length of the sliding zone ℓ, the adhesion energy γ, the Young modulus E and the thickness of the strip h:

$$G = \gamma + \frac{(\tau\ell)^2}{2Eh} \tag{4.4.4}$$

We can finally rewrite an equation for the energy balance during the peeling process as in equation 2.3.3, but adding an extra term due to the friction dissipation:

$$\frac{1}{2}\frac{f_{pl}^2}{Ehw_o} + f_{pl}(1-\cos\theta) = \left(\gamma + \frac{(\tau\ell)^2}{2Eh}\right) w_o, \tag{4.4.5}$$

where F_{pl} is the force measured at steady front propagation (renormalized by the weight of the strip). A priori, we do not know neither the value of the friction shear stress nor the value of the sliding zone length ℓ. However, we know that the horizontal component of the force will compensate the friction force in order to keep the front in quasi-static equilibrium. Note again we neglect here the contribution of the shear-lag zone $\ell_{lag} \ll \ell$ to the frictional stresses, so that that

$$f_{pl} \cos\theta = \tau \ell w_o.$$

Inputing this relation into the previous equation we obtain

$$f_{pl}(1-\cos\theta) + \frac{1}{2}\frac{f_{pl}^2}{Ehw_o}\sin^2\theta = \gamma w_o \tag{4.4.6}$$

Equation (4.4.6) was already reported in 2011 by *Jagota and Hui* [74] where a similar derivation was used, but it was not compared to experimental data. Note that this expression is reminiscent of Kendall's "frictionless" prediction: $F(1-\cos\theta) + \frac{1}{2}\frac{F^2}{Ehw_o} = \gamma w_o$, which accounts for the extensibility of the material, but does not involve frictional dissipation. The difference between both expressions is a factor $\sin^2\theta$, and this factor is very important as it leads to a diverging peeling force for vanishing peeling angle. In some sense, equation (4.4.6) is closer to the inextensible peeling formula $F(1-\cos\theta) = \gamma w_0$ than the extensible case: frictional dissipation seems to reduce greatly the effect of extension of the strip.

In figure 4.10, we show the comparison of this simple model with the data previously presented on figure 4.6. We can already see that our linear model is already in quite good agreement with the experimental data, even though very large strains on the order of 25% are reached in experiments. We now describe a finite elasticity model that accounts for non-linear elasticity.

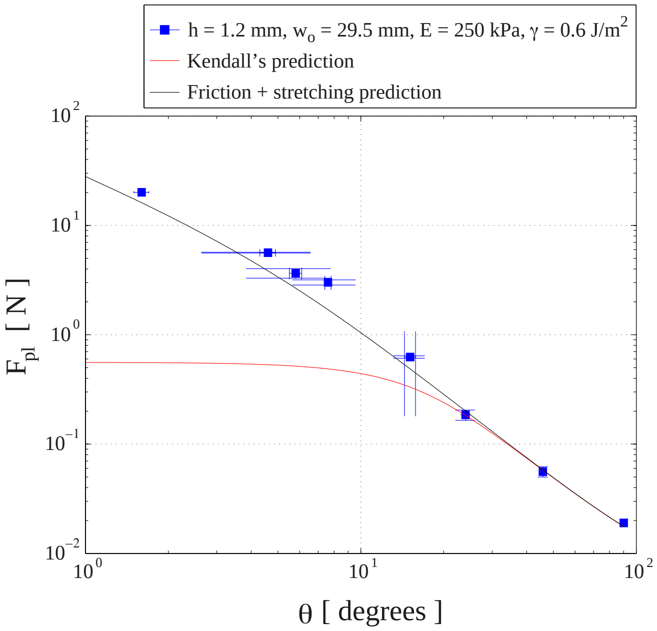

Figure 4.10.: *Peeling force for a typical strip measured for different angles and compared to Kendall's "frictionless" theoretical prediction (red line) and to equation (4.4.6) in solid brack line. (Same sample as in figure 4.6).*

4.4.2. Large strains

Section developped in collaboration with C.Y. Hui

Nonlinear elasticity

Consider a strip with initial width w_o, length L_o and thickness h_o. Under uniform uniaxial tension, its length becomes $L = \lambda L_o$, where λ is the stretch ratio. The material is also deformed in the other directions. We define the corresponding stretching ratios by $w = \lambda_2 w_o$ and $h = \lambda_3 h_o$. Under uniaxial tension, we expect $\lambda_2 = \lambda_3$. Volume conservation for an elastomer material finally imposes $\lambda_1\lambda_2\lambda_3 = 1$, which leads to $\lambda_2 = \lambda_3 = \lambda^{-1/2}$.
The elastic energy in this state can be written as

$$\mathscr{E} = \frac{\mu}{2} w_o h_o L_o \phi(\lambda)$$

with $\phi(1) = 0$. Here, $\phi(\lambda)$ is the density of the non-linear elastic energy for a specific material and μ is its shear modulus. For example, in the case of a neo-Hookean solid, the energy is $\mathscr{E} = \frac{\mu}{2} w_o h_o L_o (\lambda_1^2 + \lambda_2^2 + \lambda_3^2 - 3)$, and $\phi(\lambda) = \lambda^2 + 2\lambda^{-1} - 3$ if the material is incompressible. However, we will consider the general case independently from the detailed expression of $\phi(\lambda)$.

The tension force T that produces a stretch λ is obtained by considering the case where L is stretched by dL. The work of the operator TdL is transformed into the elastic energy $d\mathscr{E} = \frac{1}{2}\mu w_o h_o L_o \phi'(\lambda) d\lambda$. Since $dL = L_o d\lambda$, the tension is given by

$$T = \frac{1}{2}\mu w_o h_o \phi'(\lambda)$$

Again, in the neo-Hookean case, $\phi'(\lambda) = 2\lambda - 2\lambda^{-2}$, and if we write $\lambda = 1 + \varepsilon$ for small deformations ($\varepsilon \ll 1$), we recover $T = w_o h_o \mu \varepsilon$ where μ is proportional to the Young's modulus.

Energy balance in steady state peeling

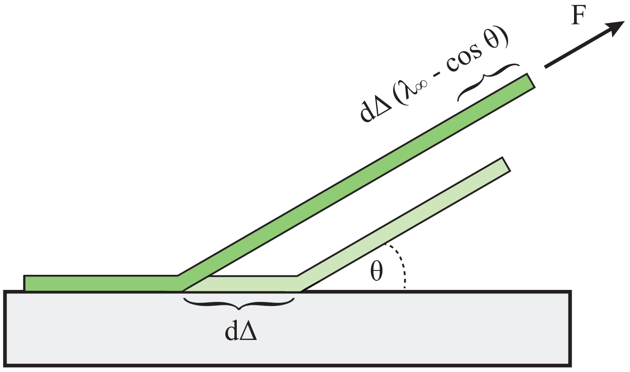

Figure 4.11.: *Sketch of the peeling process, showing the configuration before and after the detachment of a certain length of crack* $d\Delta$.

We consider again a steady state peeling where the front advances by a distance $d\Delta$. During this step, the work of the operator is calculated using the displacement along the force $\lambda_\infty d\Delta - \cos\theta\, d\Delta$, where λ_∞ is the stretch ratio due to force F.

$$dW_{op} = F(\lambda_\infty - \cos\theta)d\Delta$$

The variation of the elastic energy in the strip is that of a strip with initial length $d\Delta$ now submitted to extension λ_∞

$$d\mathscr{E} = \frac{1}{2}\mu w_o h_o \phi(\lambda_\infty)d\Delta$$

The work of adhesion is simply:

$$\gamma w_o d\Delta.$$

We now focus on the work of friction.Assuming steady state propagation, a material point with initial position X slides from $X + u(X)$ to a new position which corresponds to $X + u(X + d\Delta)$, leading to a frictional dissipation $\tau w \frac{du}{dX} d\Delta$ and therefore to

$$dW_{friction} = d\Delta \int_{slip\ zone} \tau w \frac{du}{dX} dx$$

However, the equilibrium equation remains valid:

$$\frac{dT}{dx} = \tau w,$$

where T is the tension. The equation can thus be rewritten into:

$$dW_{friction} = d\Delta \frac{1}{2}\mu w_o h_o \int_{slip\ zone} (\lambda - 1)\phi'' d\lambda$$

where we have used $\frac{du}{dX} = \frac{d(x-X)}{dX} = \lambda - 1$. This last integral is integrated by parts into

$$dW_{friction} = d\Delta \frac{1}{2}\mu w_o h_o [(\lambda - 1)\phi' - \phi]_{slip\ zone}$$

If we note λ_o the value of λ just before detachment, and use the fact that ahead of the sliding front, $\lambda = 1$, we obtain:

$$dW_{friction} = d\Delta \frac{1}{2}\mu w_o h_o [(\lambda_o - 1)\phi'(\lambda_o) - \phi(\lambda_o)]$$

It is again remarkable that the rate of energy dissipation by friction is independent from the actual value of the friction coefficient τ.

As we consider at a global force balance, frictional contact equilibrates the component of the force F parallel to the substrate, which leads to:

$$F_o = F\cos\theta = \frac{1}{2}\mu w_o h_o \phi'(\lambda_o)$$

The global energy balance is :

$$F(\lambda_\infty) - F = \gamma w_o + \frac{1}{2}\mu w_o h_o \phi(\lambda_\infty) + \frac{1}{2}\mu w_o h_o [(\lambda_o - 1)\phi'(\lambda_o) - \phi(\lambda_o)]$$

or more simply

$$
\begin{aligned}
2\frac{\gamma}{\mu h_o} &= \left[\lambda_\infty\phi'(\lambda_\infty)-\phi(\lambda_\infty)\right]-\left[\lambda_o\phi'(\lambda_o)-\phi(\lambda_o)\right] && (4.4.7)\\
F &= \frac{1}{2}\mu w_o h_o\phi'(\lambda_\infty) && (4.4.8)\\
F\cos\theta &= \frac{1}{2}\mu w_o h_o\phi'(\lambda_o) && (4.4.9)
\end{aligned}
$$

These series of equations were derived independently by *Begley, Collino and coworkers* [59, 52], together with experimental measurement of peeling force for relatively low angles. Note that if we linearize these equations for small strains $(\lambda-1)=\varepsilon\ll 1$, and using $\phi\sim\varepsilon^2$, we find that $[\lambda\phi'(\lambda)-\phi(\lambda)]\sim 2\varepsilon+\varepsilon^2$. Because in this limit $T=\mu h_o w_0\varepsilon$,

$$2\frac{\gamma}{\mu h_o}=2\frac{F}{\mu h_o}(1-\cos\theta)+\left(\frac{F}{\mu h_o}\right)^2(1-\cos^2\theta)$$

and we finally recover equation (4.4.6) obtained directly from linear elasticity and small strain theory.

Comparison with experimental data for a single strip

We wish to test the validity of the finite strain model by comparing the experimental data to the numerical solution of the system of equations (4.4.7), (4.4.8) and (4.4.9). To solve the system of equations, we have to estimate the energy density $\phi(\lambda)$ as a function of the stretch ratio λ. We use the experimental description of the force as a function of the strain $F(\varepsilon_w)$ already described in section 3.6.1. The force is considered to be $\frac{\nu F(\varepsilon_w)}{E h_o w_o}=\phi'(\varepsilon_w)=a\varepsilon_w^5-b\varepsilon_w^3+\varepsilon_w$, where $\varepsilon_w=\lambda_w-1$ (which can be large or small strain). Then the previous expression can be rewritten in terms of λ_w as

$$\phi'(\lambda_w)=a\lambda_w^5-5\lambda_w^4+(10a-b)\lambda_w^3+(-10a+3b)\lambda_w^2+(5a-3b+1)\lambda_w+(-a+b-1)$$

Being a polynomial, it is easy to integrate this expression and compute $\phi(.)$, with an integration constant equal to $c=(31a+7b)/6$, which ensures that $\phi(\lambda=1)=0$. The constants a and b are computed for each material through the fitting of the experimental data (see for example a typical curve on figure 4.12 where we find in this case $a=125.2693$ and $b=6.8980$).

We can now compare the non-linear elastic model to the experimental peeling forces. In figure 4.13, we present the measured plateau force as a function of the peeling anglecompared to three different models: Kendall's "frictionless" model of a stretchable and non sliding strip (red line) and our frictional models for linear (black line) and non-linear (blue dashed line) elastic behavior. We can see that the experimental data is well described by the models considering sliding friction in the range of angles that we could test. In this range, the linear and non-linear predictions are very close. Although the difference between the two predictions could be more important for smaller angles, they are out of our experimental range. We will therefore use and analyze the linear model from now on, for the sake of simplicity.

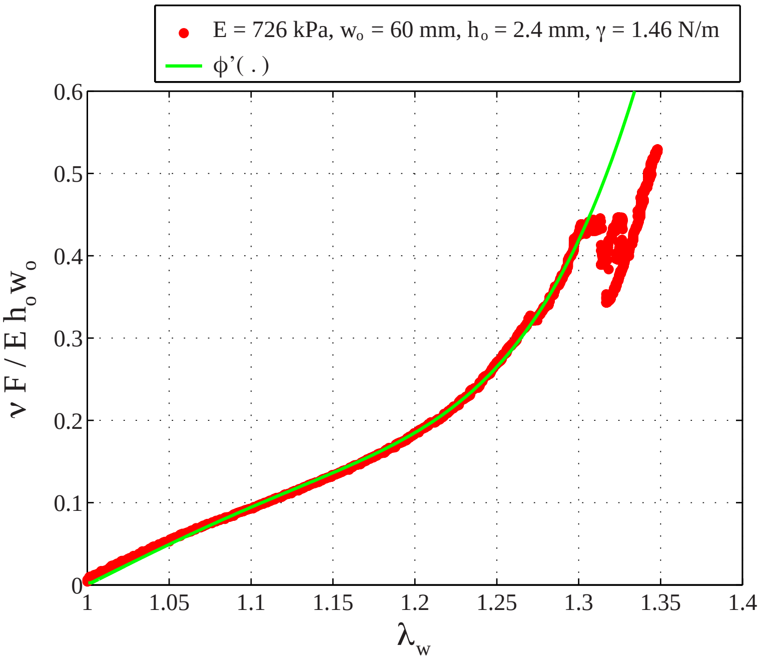

Figure 4.12.: *The force-strech curve* $F(\lambda)$ *gives a measurement of* $\phi'(\lambda) = \frac{F}{Ew_o h_o}$. *Experimental data is presented in red together with the fit which serves to compute a and b constants (in green).*

4.5. Discussion

4.5.1. Peeling force and asymptotic regimes

Comparing experiments with different samples

We extend our comparison of equation (4.4.6) to five additional sets of experiments in figure 4.14. For a better comparison of the data sets we have non-dimensionalized the peeling force f_{pl} by γw_0. These data as thus compared with the non-dimensionalized version of eq. 4.4.6:

$$\left(\frac{f_{pl}}{\gamma w_o}\right)(1-\cos\theta)+\frac{1}{2}\left(\frac{f_{pl}}{\gamma w_o}\right)^2\frac{\gamma}{Eh}\sin^2\theta = 1$$

These additional experiments have been carried with different material parameters (see table 4.5.1), and therefore slightly different values of the non-dimensional parameter γ/Eh that governs the behavior of the system. Higher values of γ/Eh correspond to a more elastic deformation induced by adhesion. In the experiments, γ/Eh was varied from 7.10^{-5} to 2.10^{-3}.

Expression (4.4.6) fairly describes our experimental data. Although γ/Eh was varied by a factor of 30, it does not lead to significant variation of the force-angle curve in our experiments.

Asymptotic regimes

Two asymptotic regimes can be determined for large and low peeling angles, respectively. Below which angle should we account for the final extensibility of the strip and for friction?

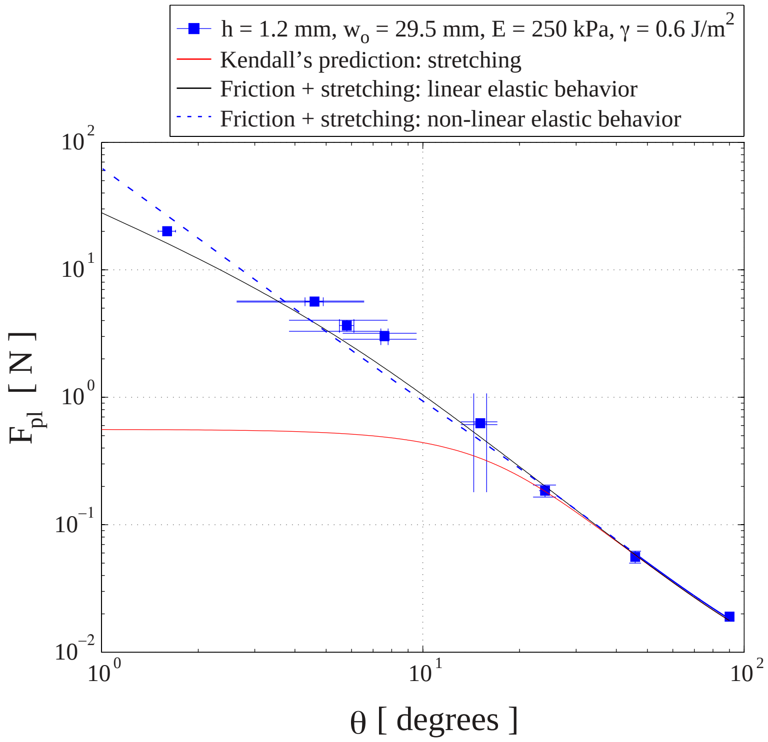

Figure 4.13.: *Peeling force for a typical strip (Same sample as in figure 4.6), measured for different angles. Kendall's "frictionless" theoretical prediction is drawn in red line, linear elasticity equation (4.4.6) in solid brack line, and the solution to non-linear prediction (4.4.7), (4.4.8), (4.4.9) in dashed blue line.*

Large angles
For large peeling angles, the data and theoretical prediction converge towards the classical case of an inextensible strip described by Kendall in equation (2.3.2):

$$F_{pl} = \frac{\gamma w_0}{1-\cos\theta}.$$

Low angle limit
In the limit $\theta \ll 1$, the expression for the force can be simplified into:

$$\left(\frac{F_{pl}^2}{Ehw_0} + F_{pl}\right)\theta^2 \simeq 2\gamma w_0$$

Since the force tends to diverge at low peeling angles, we may assume $F_{pl} \gg Ehw_0$, which leads to:

$$F_{\theta\to 0}^{friction} \simeq \frac{w_0\sqrt{2\gamma E h}}{\theta} = \frac{F_K}{\theta}$$

Conversely, in the classical limit of an inextensible strip ($F_{pl} \ll Ehw_0$), the expression for the force becomes:

$$F_{\theta\to 0}^{inext} \simeq \frac{\gamma w_0}{\theta^2}$$

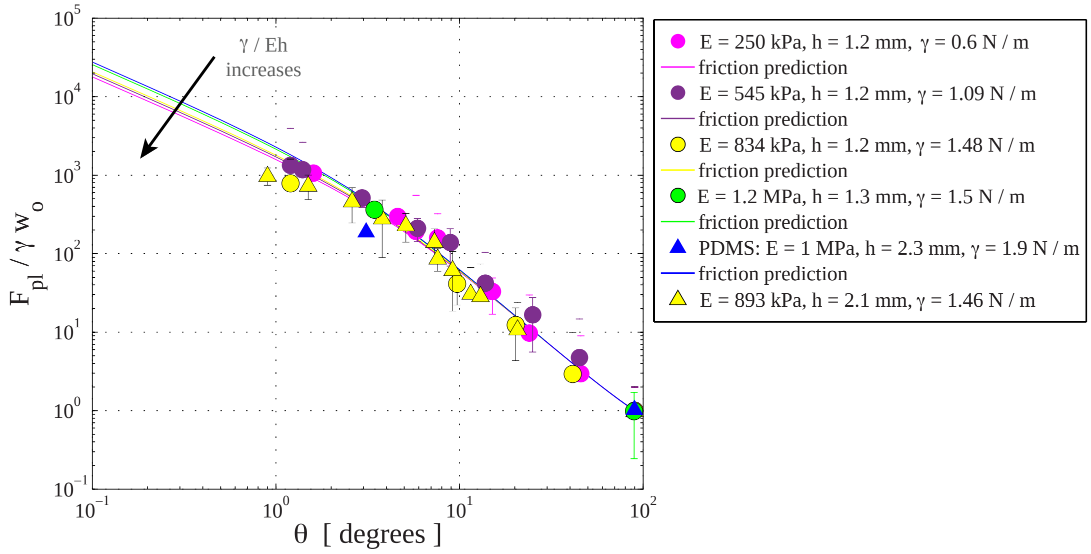

Figure 4.14.: Plateau *value of the peeling force non-dimentionalized with respect to the 90° adhesion force as a function of the peeling angle.*

	E [kPa]	h_o [mm]	w_o [mm]	γ [J/m^2]	γ/Eh_o
●	250	1.2	29.5	0.6	$2{\cdot}10^{-3}$
●	545	1.2	24	1.09	$1.7{\cdot}10^{-3}$
○	834	1.2	19	1.48	$1.5{\cdot}10^{-3}$
●	1200	1.3	30	1.5	$9.6{\cdot}10^{-4}$
△ (PDMS)	1000	2.3	30	1.9	$8.3{\cdot}10^{-4}$
△	893	2.1	30	1.46	$7.8{\cdot}10^{-4}$
■ (bilayer)	17000	1.2	30	1.5	$7.4{\cdot}10^{-5}$

Tables 4.5.1.: *Specifications for data presented in figure 4.16.*

Although our set of experimental data is limited for very small angles, we do observe a transition between both regimes ($F_{pl} \propto 1/\theta$ and $F_{pl} \propto 1/\theta^2$). The crossover between both regimes is expected for $F^{friction}_{\theta\to 0} \sim F^{inext}_{\theta\to 0}$, *i.e*:

$$\theta_c \sim \sqrt{\frac{\gamma}{2Eh}}$$

The numerical value of this crossover angle ranges from 1.6° to 2.6° for our experimental data. In order to probe our prediction more convincingly, it would thus be interesting to conduct experiments with softer or thinner elastomers. However, we would then be limited by the high strains generated by peeling. For instance, we observed that thinner strips often break before reaching a steady regime.

Prediction of the sliding length ℓ

In figure 4.15, the length of the sliding area is shown as a function of the peeling angle θ. As expected, the sliding length increases as the peeling angle is decreased and vanishes for large angles. From the asymptotics, we expect the peeling force to be given by $\sqrt{2\gamma Eh}/\theta$ for low

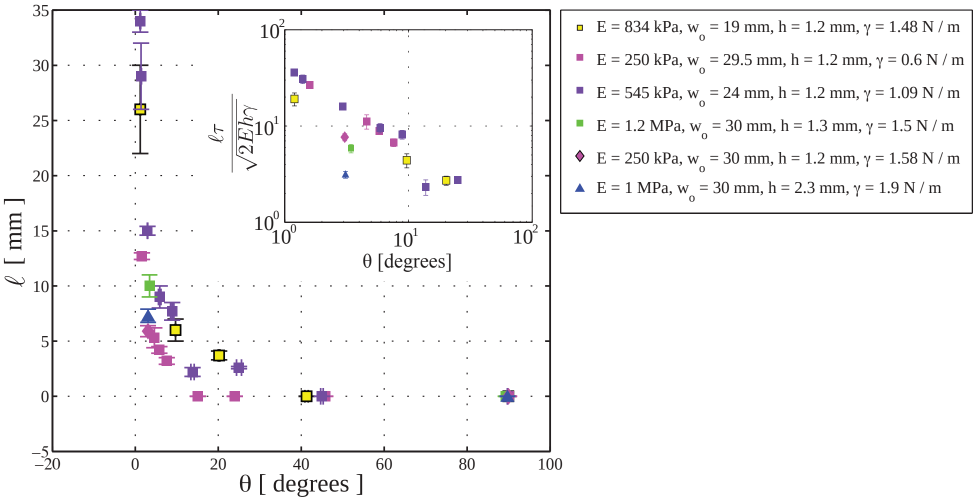

Figure 4.15.: *Sliding length as a function of the peeling angle. In linear-linear scale axes. On the inset, we show the renormalized sliding length as a function of the peeling angle, with log-log axes.*

angles. If we balance this force with the friction force $\tau\ell w_o$, we obtain:

$$\ell \simeq \frac{\sqrt{2\gamma Eh}}{\tau\theta} \tag{4.5.1}$$

We have plotted the renormalized sliding length as a function of θ on a bi-logarithmic scale in the inset in figure 4.15. Although our measurements do not span a wide range of peeling angles, our data are in agreement with the prediction for the sliding length, displaying a slope around -1. We note however a large dispersion in the non-dimensional data. This scattering may be due to fluctuations of the value of τ in the different experiments. We have indeed considered a constant value $\tau = 40$ kPa in the expression $\ell\tau/\sqrt{2E\,h\gamma}$ represented in the graph.
Finally, when the sliding length for small angle reaches a value of the order of the finite adhering length L_a, we cannot see any difference with the lap-shear configuration. In that case, we recover $F \sim F\cos\theta = \tau w_o L_a$.

4.5.2. Energy dissipation

As correctly computed by Kendall, the measure of the peel force F at a given peeling angle θ provides an estimate of the corresponding energy release rate G:

$$Gw_0 = \frac{1}{2}\frac{F^2}{Ehw_o} + F(1-\cos\theta)$$

In the previous sections, we have interpreted the dissipation rate as the sum of the adhesion energy γ (cleavage) and a dissipation due to a friction stress τ, so $G = \gamma + (\tau\ell)^2/2Eh$. The adhesion energy can be estimated from a standard 90° peeling test (with some precautions to account for the weight of the strip in the actual measurement as described in section 4.2.4). We expect the relative excess of dissipation to be given by:

$$\frac{G-\gamma}{\gamma} = \frac{(\tau\ell)^2}{2Eh\gamma}$$

Using the force balance in the direction of the substrate plane $\tau\ell w_o = F\cos\theta$ leads to:

$$\sqrt{\frac{G-\gamma}{\gamma}} = \frac{F\cos\theta}{w_o\sqrt{2Eh\gamma}} \tag{4.5.2}$$

This expression is in good agreement with the experiments where F, G, γ and the material properties are measured independently. The excess of dissipated energy vanishes for high peeling angles. However, we observe in the most extreme case a relative excess of energy release rate with respect to the adhesion energy on the order of 400, which confirms the strong effect of friction at low peeling angles.

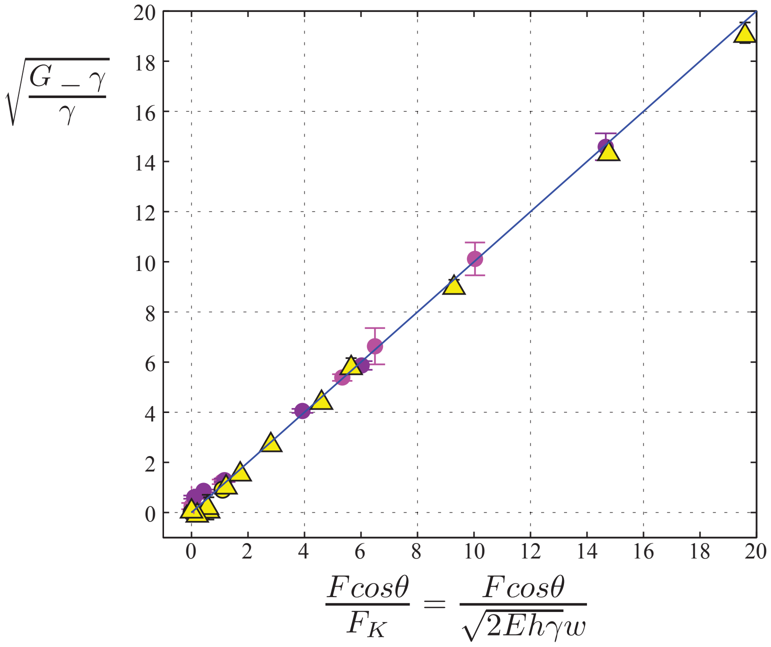

Figure 4.16.: *Relative excess of dissipated energy as a function of the component of the force parallel to the plane. The different quantities F, G, γ and the material properties are measured independently. Straight line, unit function as expected from Eq. 4.5.2*

Our model considering sliding friction could be interpreted in terms of "mode mixity" as defined in traditional fracture mechanics. The adhesion energy γ would indeed be equivalent to a cleavage mode I, while friction would correspond to a shear mode II. However, the hypotheses required for standard crack theory are not fulfilled. Indeed, the process zone of this "crack" is not confined in a narrow region around the crack tip, but has a macroscopic extension ℓ. Nevertheless our simple approach with two additive terms could be considered as an interpretation that provide insights of the phenomenon in a wider scope. We hope that our study will open deeper discussions in the field.

Frictional adhesion in other systems : dissipation and extensional energy

In our peeling experiments, the elastic strip undergoes large extension. If extensional energy were neglected (case of an inextensible strip), we would predict a diverging peeling force $F = \gamma w_o/(1-\cos\theta)$ for a vanishing angle. The effect of extensional energy is to increase significantly the energy release rate (by $F^2/2Ehw$), and therefore allow a peeling front propagation for lower (bounded) forces. When sliding friction dissipates energy, we have seen that it compensates for almost all the extensional energy release rate (up to a factor $\cos^2\theta$). The result is that the friction dissipates almost completely the extensional energy provided to the system, retrieving a force almost as high as for the non-extensible case.

In Annexe B, we give theoretical examples of other situations where the adhesion, friction and extensional energy take place and compete/cooperate in order to detach a thin layer from a substrate.

4.5.3. Some surprising properties of the frictional model

The frictional dissipation model that we have presented involves some unexpected features, which we comment in this section.

The peeling force is independent of τ

A first property can be read directly on the equation for the peeling force (4.4.6):

$$f_{pl}(1-\cos\theta)+\frac{1}{2}\frac{f_{pl}^2}{Ehw_o}\sin^2\theta = \gamma w_o$$

The value of the frictional stress τ *does not appear in this equation.* This relation suggests that the peeling force is independant from the value of friction (large or low). This effect is due to the horizontal force balance $F\cos\theta = \tau\ell w_0$ (which ensures that low friction will produce large sliding length ℓ, and high friction will be equilibrated on a small sliding zone) and the remarkable fact that dissipation only depends on the product $\tau\ell$.

The consequences are somehow puzzling since we may have expected to recover the classical frictionless peeling force as some limit case of our frictional model. The limit $\tau = 0$ thus seems singular, because when continually decreasing τ to zero, the peeling force would be constant (but the sliding length ℓ would become infinite). If $\tau = 0$ is exactly zero, the component of the peeling force parallel to the substrate cannot be balanced, and the whole strip should slide without detaching, for a vanishing force[3].

Counterintuitively, the opposite limit $\tau \to \infty$ is the one that leads to the frictionless model. Indeed, in that case the sliding length should decrease, and the assumption $\ell \gg \ell_{lag}$ may break down. In this case, equation (4.4.6) should not apply. The peeling force may now depend on τ, and we expect this force to decrease with increasing friction stress τ. Indeed for higher friction, the sliding length ℓ may eventually vanish as the sole shear-lag zone may drive enough friction. At this point, and for higher friction, there is no more frictional dissipation (absence of sliding) and we recover the classical Kendall's "frictionless" balance.

---

[3] This is, for example, the case in a liquid surface.

The force is independent from spatial inhomogeneities of friction stress τ

Our model is based on considering a constant, uniform friction shear stress τ. However, we show here that this result is general and remains valid even if we drop this hypothesis. In order to compute the work of the friction force, we have used the expression:

$$\delta W_{fr} = \int_0^{x_f+\ell} w_o \tau(x) \delta u \, dx$$

In the limit of linear elasticity, the displacement is given by $\delta u = \frac{\partial u}{\partial x} \delta x_f = \varepsilon \, \delta x_f$, with $\varepsilon = \sigma / E$. The force balance provides $\tau(x) = \frac{\partial \sigma}{\partial x} h$.

But The work of friction can also be written as

$$\delta W_{fr} = \frac{h}{E} \int_0^{x_f+\ell} w_o \delta x_f \sigma(x) \frac{\partial \sigma(x)}{\partial x} dx = w_o \delta x_f \frac{h}{2E} (\sigma(x_f+\ell)^2 - \sigma(0)^2) = \frac{1}{2} E h w_o \varepsilon_\infty^2 \, \delta x_f$$

which depends solely on the value of the friction shear at the edge of the sliding zone. The dissipation is therefore independent of the variation of the friction stress in the limit where the friction is not localized in the immediate vicinity of the peeling front but is distributed along a macroscopic sliding zone.

Robustness of experimental measurements

These properties of the model (being independent on the detail of friction stress) probably explain why our measurement of the peeling force are rather reproducible, whereas in previous chapter the sliding and frictional dynamics (e.g. stick-slip and secondary detachment front for lap-shear geometry) were observed to be very noisy and not so reproducible from one experiment to the other.

4.5.4. When is frictional adhesion expected?

In which case do we expect frictionally enhanced adhesion to hold? We propose to review the different conditions leading to frictional adhesion and to provide a configuration diagram describing the different cases.

In the case of peeling at zero-degrees, we have assumed that frictional sliding may occur in some materials, and not in others. This argument was rationalized with the speculative idea of a time-scale for re-adhesion to be compared with typical time for an experiment. If the sliding friction is null, then our model obviously does not hold. We thus focus on “re-adhering” materials such as the silicone rubber used in our experiments.

If the sliding friction is zero, then our model obviously does not hold. So, the first condition is the existence of a sliding friction shear stress τ. Beyond this first condition on material properties, three lengths should be compared in order to predict the frictional behavior of the strip:

- the shear-lag length ℓ_{lag}, which is fixed for a given material independently of loading,
- the sliding length ℓ,
- the adhered length of the strip L_a.

The second condition is $\ell_{lag} \ll L_a$.
Indeed if this condition, which is verified for all our experiments, does not hold then the whole strip undergoes shearing when loaded in a peeling geometry. We then expect a different mechanism close to the catastrophic scenario proposed by Crosby and collaborators.

The third condition is: $\ell_{lag} \ll \ell \leq L_a$
This condition allows on one side ($\ell_{lag} \ll \ell$) to connect the sliding length to the peeling force in a simple way through the force balance $\tau \ell w_0 = F \cos\theta$. Note that if $\ell > L_a$, the strip is not long enough to allow for the entire sliding zone to develop and reach the steady state. We now carefully study this double condition, which is not obvious because the sliding length ℓ is not a constant and depends strongly on the peeling angle.

A phase diagram

A good way to describe the effect of the conditions on the sliding length ℓ is to imagine an experiment starting from large peeling angle and reducing the angle up to zero. Because it is quite complex, we summarize it in the form of a schematic phase diagram in figure 4.17 which only considers the case $\ell_{lag} \ll L_a$ and the existence of a frictional sliding stress τ.
If we start with $\theta = 90°$, there is no component of the peeling force parallel to the surface. We therefore do not have any sliding, $\ell = 0$. As a result, we expect Kendall's frictionless model to hold. We note $F_K(\theta)$ the corresponding peeling force. We expect this non-sliding condition to be valid as long as the peeling angle leads to:

$$F_K(\theta)\cos\theta < \tau w_o \ell_{lag}. \tag{4.5.3}$$

As the peeling angle is reduced, $F_K(\theta)$ increases and the condition (4.5.3) may fail. This will occur if the maximum force (reached for vanishing θ) within this "frictionless" model is higher than the sliding condition:

$$F_K(0)/w_o = \sqrt{2Eh\gamma} > \tau \ell_{lag} \tag{4.5.4}$$

We note θ_2 the corresponding peeling angle where the non-sliding condition (4.5.3) is violated. At this point sliding occurs and the component of the peeling force parallel to the substate is balanced partially by the shear-lag friction and partially by sliding stress. At first, ℓ is very small and the computation of the peeling force requires a model where both ℓ and ℓ_{lag} are comparable. We do not give here an analytical expression for the peeling force $F(\theta)$ in this case, but must have $F(\theta) > F_K(\theta)$ for $\theta < \theta_2$ since dissipation increases due to frictional sliding.

As lower peeling angles are explored, the force $F(\theta)$ and the length ℓ increase. The 3rd condition $\ell \gg \ell_{lag}$ will eventually be reached for an angle θ_1. We expect that the frictional adhesion model holds when $\theta_0 < \theta < \theta_1$. Within this model, we indeed know that the peeling force diverges as the peeling angle approaches to zero. Eventually there is an angle θ_0 above which ℓ would be larger than L_a. In an experiment for an angle $\theta < \theta_0$, we thus expect a sliding front to propagate and reach the end as in our zero-degrees peeling configuration. In this case we do not observe any plateau for the force and the strip suddenly detaches as the front reaches its free end. The corresponding maximal force is given by $F = \tau w L_a$. Our first situation was therefore not singular as a small peeling angle lower than θ_0 would lead to the situation we described in the previous chapter.

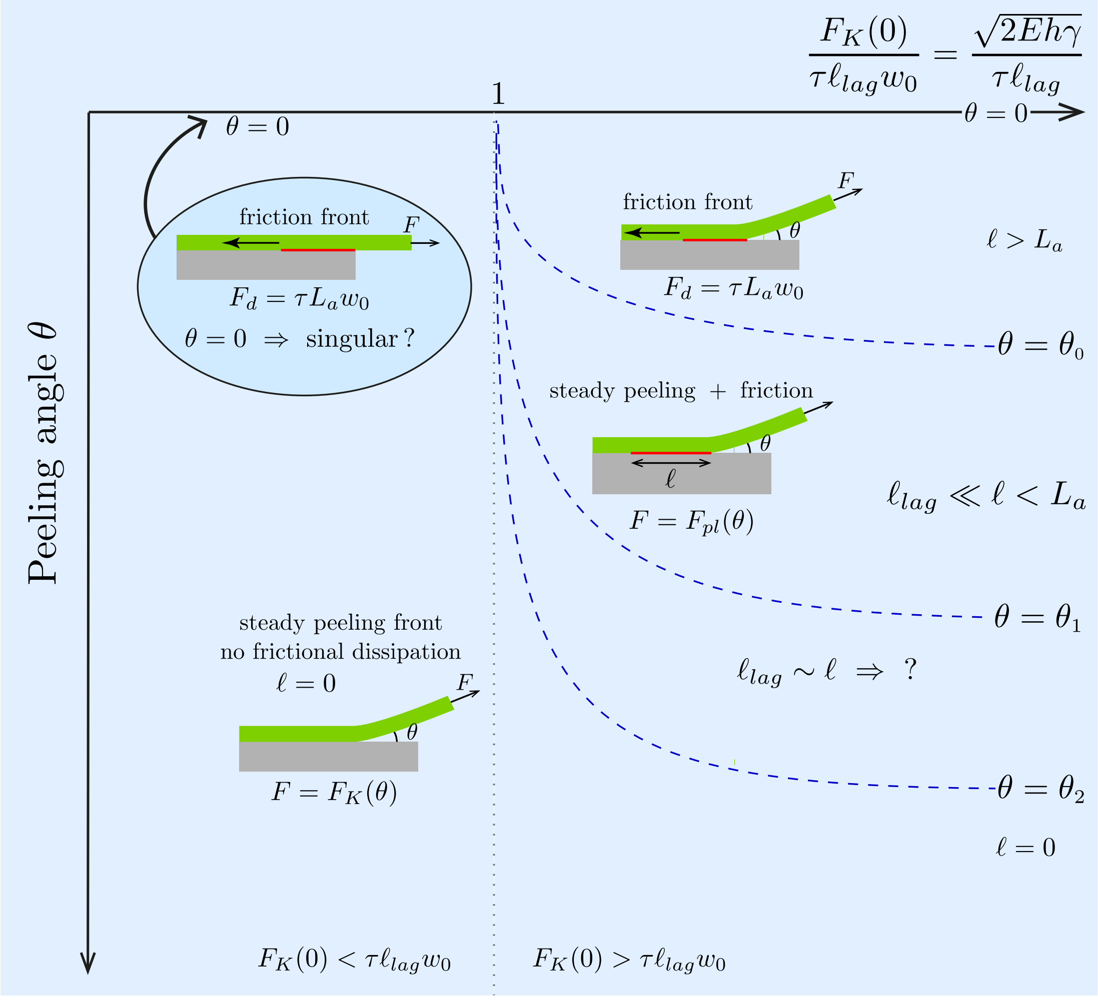

Figure 4.17.: *Configuration diagram for $L_a \gg \ell_{lag}$ in the case of a frictional sliding stress τ. Note that the exact shape of the boundaries in dashed lines will depend on the value of Eh/γ.*

In diagram 4.17, the abscissa represents the non-dimensional number $F_K(0)/\tau\ell_{lag}w_o = \sqrt{2Eh\gamma}/(\tau\ell_{lag})$ which divides the plane in two zones. The four regions described above are all displayed on the right of the $F_K(0) = \tau\ell_{lag}w_o$ limit. Note that the expression for the peeling force in the case of frictional adhesion (Eq. 4.4.6) is not valid for $\theta > \theta_1$. In the limit of large angles ($\theta > \theta_2$), this expression nevertheless gives almost the same prediction as Kendall's frictionless model. Indeed the extensional term is negligible in this limit. We therefore expect the model to provide a reasonable prediction also in the transition region.

We now focus to the case where condition (4.5.4) is not satisfied, so that even the largest force in Kendall's frictionless model does not lead to any sliding. For non-zero angles, we indeed expect Kendall's frictionless prediction to correctly describe the system (this is represented in the left part of diagram 4.17). We however believe that the $\theta = 0$ case is a singular limit here, because geometry imposes sliding (the displacement of the strip is parallel to the substrate). In the following section, we give an experimental observation that seems to support this scenario.

An example of frictionless peeling ?

We investigated the case of strips of the same PVS elastomer, but covered with a thin backing layer. For this experiment we used a layer of PVS, $h = 1$ mm thick with a Young modulus $E = 250$ kPa. The layer was covered with a backing made of thin mesh of nylon fabric ($70\,\mu$m square lattice) that we placed on the upper surface of the strip when the polymer was curing. The backing is $80\,\mu$m thick and its effective stretching rigidity is $E_b h_b = 16 \cdot 10^3$ N/m.

In figure 4.18 we plot in blue stars the data obtained with the backing layered strip and compare them to the results previously presented on blank strips of similar properties (pink squares). Although both types of strips display a similar “Kendall” behavior for large peeling angles, forces are significantly different for angles lower than 10°. Surprisingly, the data with the backing seem to follow Kendall’s “frictionless” theoretical prediction very well (note that the model including frictional adhesion for this effectively stiffer composite strips would lead to an even larger force than that for the blank strip). We only have one point here, but it seems to lay on the plateau force of the frictionless model, suggesting that even for lower angles, the force would not rise higher, so that sliding has little chances to occur even at much lower angles.

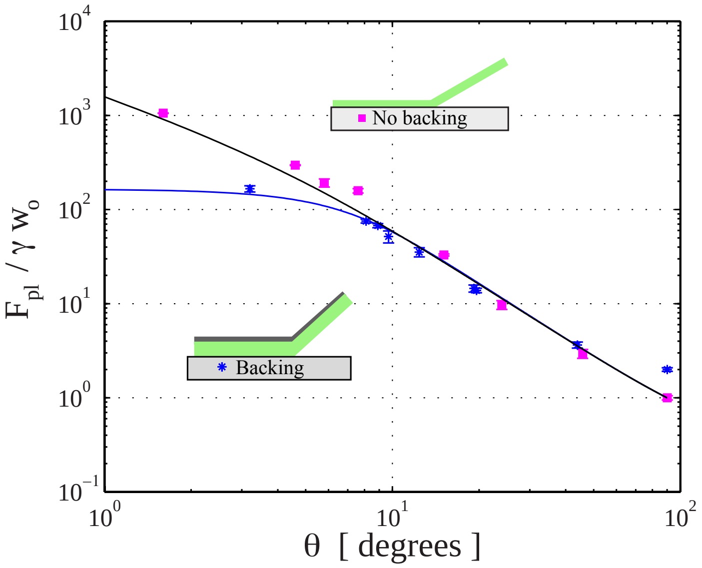

Figure 4.18.: *Effect of a backing tape in the peeling of an elastomer strip. Data collected corresponding to strips covered with a thin baking of effective stiffness $E_b h_b = 16 \cdot 10^3$ N/m (blue stars) are compared with the previous data obtained with blank strip (pink squares). The elastomer used in both cases is the same. Experimental parameters: E = 250 kPa, h_o = 1 mm, $w_o \sim$ 30 mm.*

Why do we seem to recover Kendall’s regime when a backing layer covers the elastic strip? We believe that friction in the shear-lag distance ℓ_{lag} allows to sustain the peeling force without sliding (so that we stand on the left side of diagram 4.17). Indeed due to the larger stiffness of the backing, the characteristic shear-lag length is $\ell_{lag} \sim h\sqrt{\frac{E_b h_b}{E h}}$ (eq. 3.2.10). For our particular situation ℓ_{lag} is on the order of 8 mm. The maximum force predicted in Kendall’s model is

$\sqrt{2E_{total}h_{total}\gamma} \sim 180$ N/m. The ratio for shearing stress to the critical sliding stress reads

$$\frac{\sqrt{2E_{total}h_{total}\gamma}}{\tau\ell_{lag}} \sim \frac{\sqrt{2E_b h_b\gamma}}{\tau h\sqrt{\frac{E_b h_b}{Eh}}} \sim \frac{\sqrt{2E\gamma h}}{\tau h} \sim 0.75$$

From our scaling analysis we may only conclude that the shearing stresses computed without frictional dissipation are on the order of the sliding stress τ. We assume that in this case the shear stresses are *lower* than the critical threshold for sliding. Our observations would thus be compatible with the configuration diagram (Fig. 4.17).

Note that in the absence of backing ℓ_{lag} is reduced to the thickness of the strip h, and the maximum force without sliding $F_K(0)$ is reduced to $\sqrt{2Eh\gamma}$. It turns out that both quantities are reduced by similar factor with respect to the bilayer case, so that the ratio of shear stresses to critical sliding stress in absence of backing is also

$$\frac{\sqrt{2E\gamma h}}{\tau h} \sim 0.75$$

of order one. Again we can only say that shear stresses at the interface are comparable to sliding threshold. We suggest that the numerical prefactors in this expression (that we did not compute) lead to shear stresses *above* the sliding threshold in this case, since in experiments, a large amount of sliding is observed.

We see that a strip with or without backing (in the limit of very stiff backing) should in general behave in the same regime (belong to the same column in diagram 4.17). This may be rather surprising at first because the backing allows shearing stresses to be distributed on a larger distance, but the peeling forces are also larger, so that both effects balance. Another remark is that once the threshold for sliding is attained, the peeling force jumps to a potentially much larger value. This suggests that strips that may have rather similar parameters could lead to very different peeling forces, if they are close to the sliding threshold.

We note however that other ingredients may also play important roles. Indeed adding a backing not only stiffens the strips but may also modify its effective Poisson coefficient and limit its deformation in the span-wise direction. The presence of a stiff backing may also modify the re-adhesion dynamics of the elastomer on the surface. Finally, here we have used a mesh as a backing layer, which when stretched may induce some periodic strains in the underneath interface, which could modify the adhesion properties of the strip.

Our experimental observations are therefore compatible with the arguments presented in the previous section, but many other experiments should be conducted to probe the validity of this criterion in a wider range of parameters.

4.6. Conclusions

As a summary for this chapter, we have extended our previous results obtained in a lap-test configuration to the more general case of peeling at a finite angle. We confirmed the crucial role of friction in the debonding of a soft strip of elastomer for very low angles. Our experiments confirm the propagation of a steady macroscopic sliding front that precedes the peeling front.

Guided by our experimental observations and our previous experience in the lap-test configuration, we developed a model where dissipation is decomposed in the simple sum of adhesion (cleavage) and friction energy. This model is in good agreement with our experimental data for angles ranging from 1° to 90°. We defined a crossover angle between the classical model derived by Kendall for high angles and a regime dominated by friction.

We could also check the dependence of the extension of the sliding front with material parameters. Curiously, although all experimental evidences are consistent with a constant friction stress on the order of 40 kPa, our model predicts a peeling force independent from the spatial distribution of frictional stress.

As in previous chapter, we suggest that the existence of this frictional sliding stress τ is material dependent. But even if dissipative contact sliding is possible, it may or may not occur in a given peeling configuration. For an infinite strip, we separated two typical scenario depending on the value of $\sqrt{Eh\gamma}/\tau\ell_{lag}$, where ℓ_{lag} is the shear-lag distance. In a first regime (large value of this parameter), sliding will eventually occur for sufficiently low angles, and our frictional model applies (and in this case, our model gives in fact a pretty good approximation for all angles). In a second regime (low value of the parameter), friction does not dissipate energy, and the classical results on the peeling force apply for any non-zero angle. These different regimes are sketched in figure 4.17.

This diagram needs to be thoroughly explored and checked experimentally. We hope that our preliminary study will motivate further works towards a better understanding of the coupling between friction and adhesion.

5. Adhesion of Elastic Shells

5.1. Introduction

In the first part of this manuscript (two previous chapters) we have revisited the peeling test by considering frictional sliding, which may become an important effect at low peeling angles. In this chapter we will focus on another very important test to measure adhesion, the JKR test, which consists in measuring forces when an adhesive full sphere is brought into contact with a rigid plate. This test is now a standard method to measure adhesion (see section 2.4).

Here we wish to study how this technique can be modified or extended using slender structures, whose deformations can be very large, instead of a sphere. The motivation for the use of thin shells comes from the analysis of the JKR equations [20] when comparing different material softness. We use these equations in the following non-dimensional form:

$$\frac{F}{\pi\gamma R} = \frac{4}{3} m \left(\frac{a}{R}\right)^3 - 2\sqrt{2m}\left(\frac{a}{R}\right)^{3/2} , \tag{5.1.1}$$

$$\frac{\delta}{R} = \left(\frac{a}{R}\right)^2 - \sqrt{\frac{2}{m}}\left(\frac{a}{R}\right)^{1/2} , \tag{5.1.2}$$

where the non-dimensional parameter appearing in each equation is $m = \frac{E^*R}{\pi\gamma}$, the ratio of elastic rigidity to adhesion. The non-dimensional indentation force $F/\pi\gamma R$ is plotted in figure (5.1(a)) as a function of the non-dimensional displacement δ/R for various values of $m = \frac{E^*R}{\pi\gamma}$. We observe that the detachment force, the minimal force and the force at the moment of null indentation are independent of parameter m (figure 5.1(a)). Note that the force is non-dimensionalized by the typical adhesion force $\gamma\pi R$. This means that the minimal force, for instance, could give us a measure of the adhesion energy, a priori, no matter what is the rigidity of the body.
In practice however, one has to use a the force captor with a range adapted to the measuring force. However, the force captor has also to be able to support the forces encountered during the experiment. If the maximal expected force in the experiment is large, in general this is accompanied with a rougher resolution that may not be able to capture the effect of adhesion, which is in general of the order of few mN. For rigid materials, the compression force increases very sharply with indentation (figure 5.1(a)), so that a very high precision in displacement is required.
In addition, even if the pull-off force does not depend on the stiffness of the material, the pull-off displacement and contact radius does. This presents again a practical problem of resolution versus absolute value measured, maybe even worse, since the pull-off displacement may be about three orders of magnitude smaller than the radius of the spherical probe. In figure 5.1(c), we can see how quickly the detachment indentation displacement and contact area decrease.

As a conclusion, we expect highly compliant structures, such as shells, to be particularly suitable to assess low systems displaying low adhesion energy.

5.1.1. Advantage of using shells

Another way to work with a compliant system is to use a hollow sphere, i.e. a shell, rather than a full sphere. In case of a spherical shell, the local strains may be small, but large displacements

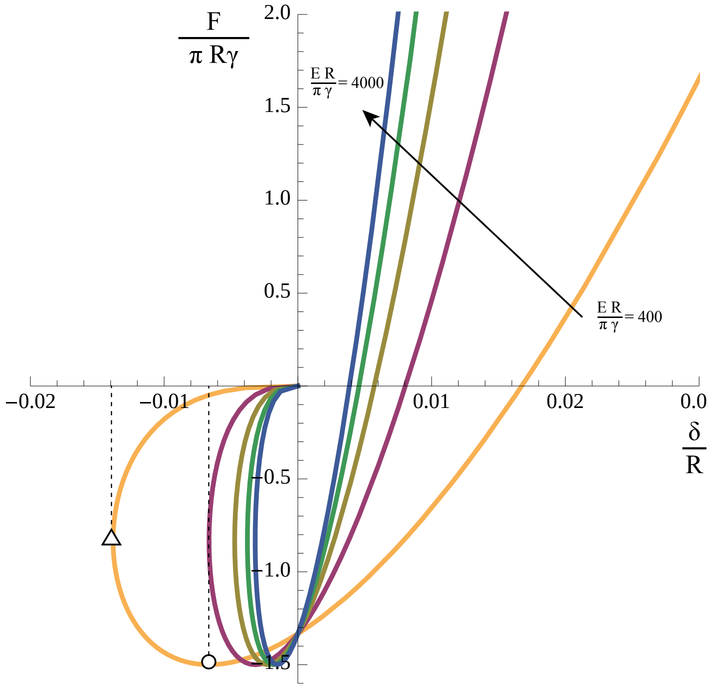

(a) Non-dimensional indentation force *vs* displacement

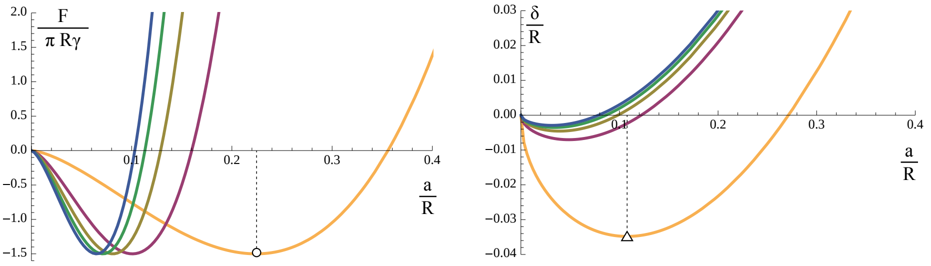

(b) Non-dimensional indentation force *vs* Contact radius

(c) Non-dimensional indentation displacement *vs* Contact radius

Figure 5.1.: *Theoretical curves of the non-dimensional variables showing the relations of equations (5.1.1) and (5.1.2). Different colors represent different values of the ratio* $m = \frac{E^*R}{\pi\gamma}$*, from 400 to 4000. (These values are in the same order of magnitude than in the experiments we will present in chapter 5)*

and changes of shape can be observed for relatively low forces.

We now consider an elastic hollow sphere of radius of curvature R, thickness h and Young modulus E, has a stiffness $K_s = 4\sqrt{(1-\nu^2)/3}\frac{E^*h^2}{R}$ [75, 76, 77], with $\nu = 0.5$. As an analogous to the non-dimensional parameter from the standard JKR case ($m = \frac{E^*R}{\pi\gamma}$), we propose to analyze the ratio between the elasticity of a shell and its adhesion. We define the non-dimensional ratio α_{hs} as

$$\alpha_{hs} = \frac{K_s}{\pi\gamma} = 2\frac{E^*R}{\pi\gamma}\left(\frac{h}{R}\right)^2 \tag{5.1.3}$$

We see that the analogous of parameter m, the ratio of elastic to adhesive stiffness is amplified by the ratio between the thickness and the radius of curvature to the square. The $(h/R)^2$ factor could decrease this ratio in four orders of magnitude considering a reliable example $h \sim 100\mu$m and $R \sim 1$ cm. This results in an effect of amplifying the effect of adhesion on the deformation of the shell. For a non-axisymmetric shell, an analogous version of this parameter can be defined [77]. In general terms, the stiffness of a shell is

$$K_{shell} = \frac{8}{3} E h^2 \kappa_M,$$

with κ_M the mean curvature of the shell around its apex and Poisson's coefficient $\nu = 0.5$.
- For a sphere: $\kappa_M = 1/R$, with R the radius of the sphere.
- For an ellipse: $\kappa_M = a/b^2$, with a and b the semi-major and semi-minor axes of the ellipse, respectively.
- For a non-axisymmetric shell: $\kappa_M = (\kappa_1 + \kappa_2)/2$, with *1* and *2* the principal directions around the apex of the shell.

5.1.2. A theoretical approach to the indentation of sticky shells?

The hard question is now to provide the equivalent of the JKR formula to the case of hollow shells. We can however build-on some interesting theoretical development that help generalize the JKR result to other geometries.

Small strain - small displacement : a linear approach

A first approach [33, 34, 78, 79], is really a generalization of the JKR initial argument and is based on small strains and small displacements (linear elasticity). The key point is that all these systems (JKR, or Hertz contact) are indeed essentially linear once the geometry is fixed, and the geometry of the problem is fixed once the contact area is fixed. There has been some interesting theoretical development that help to generalize the JKR result to other geometries. In fact, the force-displacement relation is non-linear because the contact area increases with loading. In other words, if the contact area would be maintained, then the force would be proportional to the displacement.
The clever idea from Hui *et al.* is then to estimate the elastic energy for the adhesive case (a given area of contact A for a given force F) starting from a configuration without adhesion, but with the same area of contact (and a different indentation force F_H). This last configuration is assumed to be known from the study of the non-adhesive case (Hertz contact in the case of an elastic sphere). The energy of the adhesive state is obtained using the linearity of the load-displacement response along path with constant contact area. Finally, the general expression for the energy released rate can be derived:

$$G(A) = -\frac{1}{2}\frac{dC}{dA}(F - F_H)^2, \tag{5.1.4}$$

where $C(A)$ is the compliance of the system for a fixed area A, or in other words $C(A) = \frac{\partial \delta}{\partial F}(A)$.

Another trick due to linearity is that $C(A)$ can be found from the study of the load-displacement curve for the non-adhesive experiment $C(A) = \frac{\partial \delta_H}{\partial F_H}$. For example, in the JKR case of an adhesive sphere, we start from Hertz' law:

$$F_H = \frac{4}{3}\frac{E^*}{R}a^3, \qquad \text{so that} \qquad C = \frac{\partial \delta_H}{\partial F_H} = \frac{1}{2E^* a} = \frac{\sqrt{\pi}}{2E^*\sqrt{A}}$$

In which case, using the relation 5.1.4 with $\frac{dC}{dA} = -\frac{\sqrt{pi}}{4E^*}A^{-3/2}$ and $A = \pi a^2$, we can reobtain the JKR force prediction:

$$F = F_H + 2\sqrt{2\pi E^* \gamma} a^{3/2}.$$

With the energy release rate equal to the energy adhesion $G = \gamma$.

The conclusion is that if the strains are small (material with linear stress-strain) and if all states with the same contact area have very similar geometries, then the knowledge of the non-adhesive case allows to predict the adhesive case. This is very appealing as the non-adhesive force-displacement curve can be measured experimentally even if the geometry is very complex.
Experimentally, the conditions to use this method can be translated into: *i*) axisymmetric body,
ii) made of a linear elastic material,
iii) geometrically linear [80, 81], so it deforms without large displacements,
iv) from which we know the force versus contact radius behavior for the non-adhesive case and
v) measure the force-indentation and force-contact area curves of the adhesive case, then we can deduce the adhesion energy.

Fully non-linear problem

Hui and coworkers studied theoretically the large deformation regime of detaching a inflated plane hyperelastic membrane in adhesive contact to a rigid substrate [82, 83] and applied their results in order to measure the energy release rate [78] through the compliance method. They have improved this method in order to measure the adhesion energy even if elasticity is non-linear. That includes material non-linearity (non-linear stress-strain relation) and slightly non-linear geometry changes due to adhesion (with respect to the non-adhesive case). The derivation is more complicated and leads to the final expression:

$$G(A) = \int_{F_H}^{F} \frac{\partial C(f,A)}{\partial A}(f - F_H)df \tag{5.1.5}$$

where F and A are the load and area at any point in the adhesive load versus contact area curve and F_H is the load in the non-adhesive curve to have a contact area A. The compliance $C(F,A) = d\delta/dF$ is now a function of the area and loading. Note that $C(F,A)$ does not depend only on the non-adhesive curve, but needs here to be evaluated at every state of the process. We will present later a nice geometrical interpretation of this rather difficult relation (provided in [78]), which we believe is very useful.

In this chapter, we will start by roughly studying the elastic-geometric behavior of a non-adhesive shell in order to determine if the compliance method can be applied to these non-pressurized hollow spheres. In the second part, we present our experiments on adhesive shells and present our results on measuring the adhesion energy by a simple method. In a third part, we present a mostly exploratory study of the dependence of the adhesion energy value on the shape of the shell, for non-axisymmetric shells.

5.2. Experimental setup

The experiment consists in indenting an hemispherical shell on a glass plate, as shown in figure 5.2. This movement is made in a carefully controlled fashion, so the force and indentation displacement is well controlled. A constant displacement is imposed to a shell of thickness h and radius of curvature R. Once the shell is in contact to the glass plate, there is a circular area of contact of diameter $2a$ for a given indentation[1] δ.

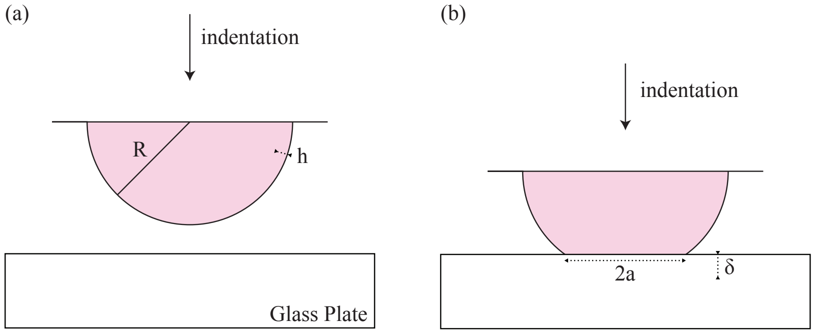

Figure 5.2.: *Schema of an experiment. (a) A shell is approached at a constant displacement to a glass plate. (b) Once in contact is observe how does the contact area change by changing the indentation.*

The shells are elastic and are generally made of PVS, though PDMS shells were also tested. We can choose the shell's rigidity between 250 kPa and about 1.2 MPa. To make the shells we use a steel sphere supported over two acrylic plates with a hole with an slightly different diameter, as shown in figure 5.3(a)(1). We make a liquid mixture of catalyst and base parts of the PVS. When it is still liquid, we pour the mixture on top of the steel ball. The liquid falls and coats the ball, creating an homogeneous layer and a planar part adhered to the annular plate A on figure 5.3(a)(1).

The plate A is the one we attach to the traction machine and the plate B is removed in order to be able to take off the steel ball from below the cast shell, as shown in figure 5.3(a)(2). This is the best technique we found to avoid any remanent stress due to taking on and off the shell from a different substrate. In order to avoid the effect of the meniscus we lift the ball 1 mm above the equator of the steel ball. This lifting distance can be changed, wether by changing the thickness of the plate A or the diameter of the hole on plate B.

Shells mounted on a traction machine (INSTRON©5865) are displaced controlling its indentation velocity, its resolution in displacement[2] is about 10-100 nm. At the same time we can measure the instantaneous force applied to the shell. This force can be tensile (negative) or compressive (positive).

The principal axis of the traction machine (see figure 5.4) is aligned to a glass plate, supported over an acrylic structure. Below this structure we have aligned a camera looking above to take pictures (or videos) of the contact of the shell to the glass plate. Another camera is installed on the horizontal axis, parallel to the glass plate to take images of the side view.

The basic experimental test that we perform is an indentation cycle. It consists on:

---

[1] The indentation δ is measured with respect to the moment of first contact.

[2] Could depend on the displacement velocity, being less accurate for faster movements, due to the inertia of the machine.

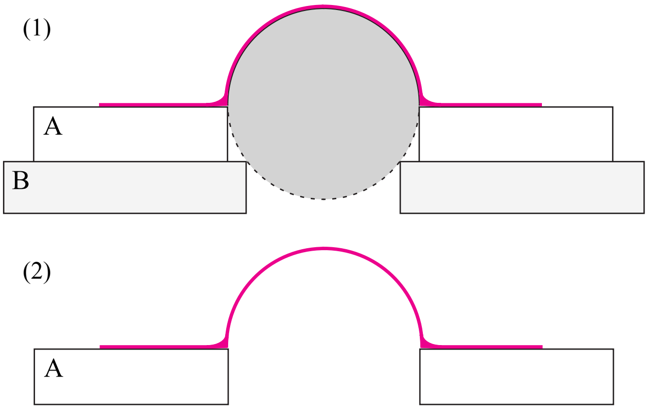

(a) Casting technique

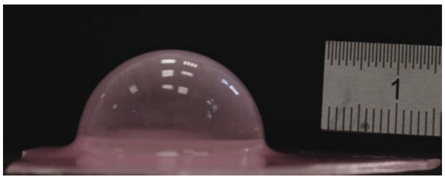

(b) Close-up of a shell

Figure 5.3.: *(a) Side view of the device used to cast the shells. (1) While casting, two concentric annular plates supporting a steel sphere. (2) Casted shell, the plate B has been removed as well the moulding sphere ready to test. (b) A photo of a typical shell used for the experiments.*

- Starting from a certain distance between the apex of the shell and the flat rigid surface, the shell is approached at a controlled velocity into contact to the surface.
- Once the desired maximal indentation is reached, during a dwell time, the shell does not move.
- After a dwell time, the shell is pulled off, up until to the initial distance.

To avoid any perturbation on the force signal, the experiments are performed during the night, so the room temperature is stable. The forces measured are of the order of a fraction of mN. To make a non-adhesive shell, we just put some talc on its surface. We put one layer of talc, then with crystal scotch© we cleaned the surface, we repeat two more times the process. At the end we had a shell that did not adhered to a glass plate.

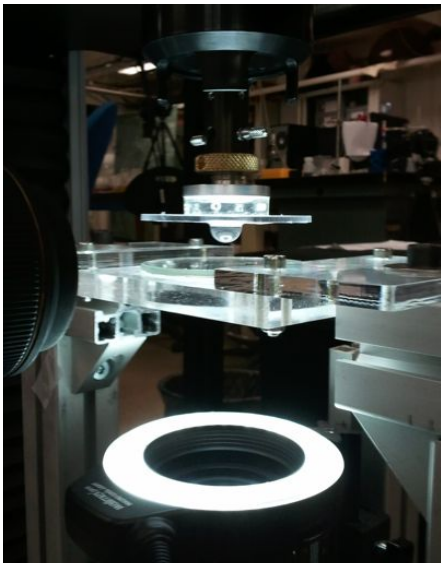

Figure 5.4.: *Experimental setup. In the center of the image, we can see a hemispherical shell sticked to an acrylic support, it is sustained over a glass plate which is above an annular lightning.*

5.3. Non-adhesive shells

We start by studying the purely elastic (non-adhesive) behavior of the shell, performing indentation cycles for a non-adhesive shell on a glass plate. The indentation of a non-pressurized spherical shell was studied before in different contexts.

Pogorelov in the 60's [84, 13], was mostly interested on the buckling of an spherical shell by indenting with a punctual punch. Pauchard and Rica at the end of the last century [85, 86], showed some experimental measurements of a spherical shell indented by a plane, and observed two regimes: a flattening of the shell against the wall and the inversion of the cap after a certain indentation. They also show results on punctual indentation where they are able to describe the formation of s-cones after the cap inversion. Their further theoretical approach is a bit intricate, but they arrive to qualitatively describe the two regimes.

More recently, Audoly and Pomeau [12] have found an analytical expression describing the shape of the shell before and after the buckling transition. They also present numerical simulations that show a good agreement with the experiments of Pauchard *et al.* [85, 86]. Lazarus *et al.* [77] have studied the change in the effective elastic stiffness of a shell when changing the local curvature around the indentation point pressurized and non-pressurized. Nasto *et al.* [87, 88] have generalized this studies by systematically changing the roundness of the indenting rigid surface, from a point to a plane for indenting a spherical shell.

5.3.1. Observations

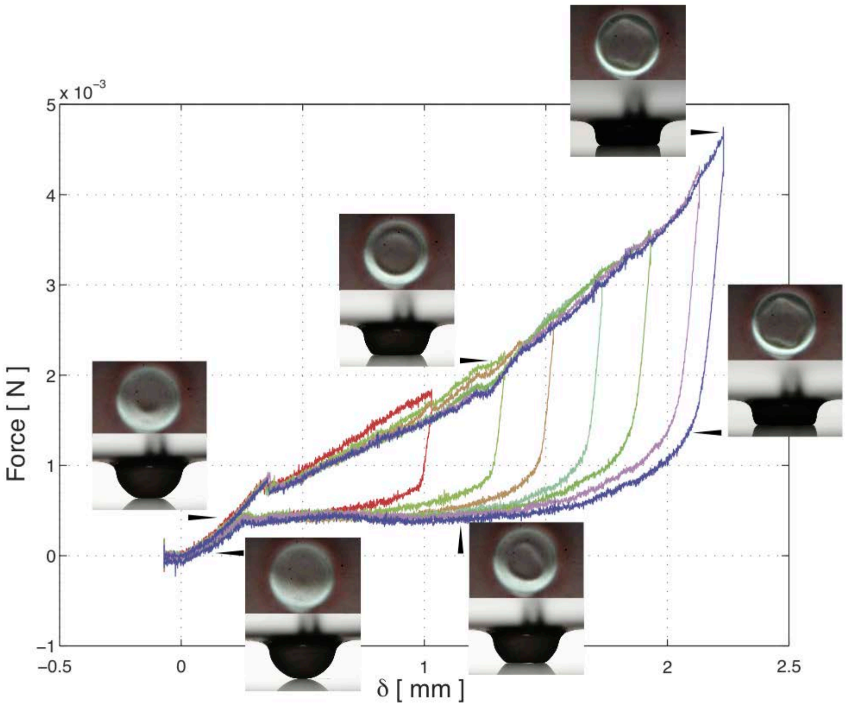

Figure 5.5.: *Set of indentation cycles for a non adhesive spherical shell. PVS, E = 250 kPa, R = 5 mm, h* $\sim 50\,\mu m$*. The photos correspond to the side and from below views of the shell and correspond to the instant indicated by the black arrows.*

We performed experiments with non-adhesive shells, at controlled displacement measuring the instantaneous indentation force. In figure 5.5, we show a set of indentation cycles varying the maximal indentation for an hemisphere of radius $R = 5$ mm and thickness $h \sim 50\mu$m . We can observe that initially the force increases monotonically and there a circular area of contact. For an indentation of approximately $\delta = 0.4$ mm, the shell buckles up forming an annular contact to the glass plate. For even larger indentation, the buckled surface changes its form, localizing the deformation on some points, it forms a pentagon-like inner fold.
When indentation is reduced, the shell quickly relaxes diminishing rapidly the indentation force without apparently changing its form, then it begins to unfold keeping the compression force at a fairly constant level. Finally, when the shell has unfolded, the annular ridge vanishes and it recovers a circular area of contact and the force follows approximatively the same ”path” as for indenting at small displacement. Then, we can say that the process is reversible, though there is a dissipation, which is probably due to friction between the talc covered shell and the glass plate. With the images taken from below we are not able to measure the contact area, because the images are not enough contrasted.
In this work we do not pretend to developp a detailed theoretical description of the elastic behavior of the shells, not for the adhesive nor the non-adhesive shells. To do it, a finite elements (FE) description should be done. The stretching and bending energies may focused in a non trivial way. Though, we could show that, before the cap inversion, Rica and Pauchard’s model [85, 86] fits our experimental data, with two free parameters.

$$\mathscr{E}_{el} = C_o \frac{Eh^{5/2}}{R} \delta^{3/2} + C_1 \frac{Eh}{R} \delta^3 \qquad (5.3.1)$$

The first term of the equation above quantifies the bending and stretching energies concentrated on the circular ridge formation around the contact area (the corner). The second term quantifies the stretching energy due to compression of the flattened (parabollic) surface.

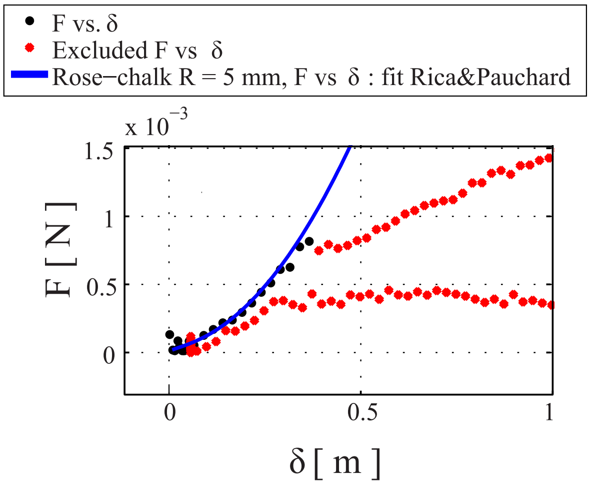

Figure 5.6.: *Last indentation cycle in figure 5.5. PVS, E = 250 kPa, R = 5 mm, h ∼ 50 µm. Rica and Pauchard’s model is fitted (in blue) to our data (black dots) showing a good agreement.*

In figure 5.6, we show how this model (eq. 5.3.1) fits our experimental data, with two fitting parameters (C_o and C_1) for the last indentation cycle on figure 5.5. The model captures the concavity of the curve and quantitatively fits the data. We obtain C_o = 5.2± 2.2 and C_1 = 2.5± 0.3 (the errors are computed from the confidence range of the fit), with an R^2 = 0.9776 for a sample with parameters: $E = 250$ kPa, $R = 5$ mm, $h \sim 50\,\mu$m. We note however that for a similar shell (same radius and thickness) made of a harder material ($E \sim 1$ MPa), the best fit was obtained with different values for $C_o \sim 17$ and $C_1 \sim 1.34$, suggesting that we cannot really trust this model.

We can see that the non-adhesive, mechanical behavior of an indented elastic spherical shell is very complex. In the following section we will present our experiments on adhesive shells and we will show how to measure the adhesion energy without need of knowing in very detail the mechanical response of the shell.

5.4. Adhesive shells

We now turn to experiments with adhesive shells. Two sequences of photos are shown in figure 5.7: the side view (fig. 5.7(a)) and the view from below (fig. 5.7(b)) where the white line shows the scale of 1 mm in both cases. The images correspond to a shell with $E = 250$ kPa, $R = 5$ mm and $h \sim 50\mu$m. The white dotted reflections on the surface of the shell are due to the annular array of LEDs we are using. These reflection can be qualitatively used to observe the deformation of the shell on the non-adhering part.

In the side view (fig. 5.7(a)), from top to bottom the indentation δ increases. For small indentations, the shell keeps its spherical form, whereas for larger indentations the shell is "flattened" into a conical frustum.

In the view from below (fig. 5.7(b)), for small indentation (top left) the contact area is seen as the darker circular area in the center of the image, whereas the annular arrange of spots is wide. Increasing the indentation (from the top and left to right) the contact area increases and the encircling bright annulus becomes thinner. This is due to the fact that the shell's surface is every time more "perpendicular" to the light source plane. In the bottom right image we superposed a black circle to show the edge of the contact.

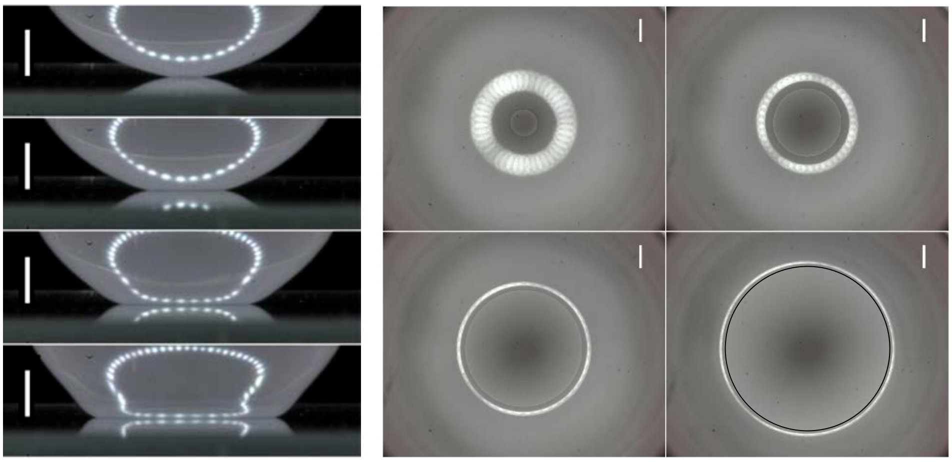

(a) Side view (b) View from below

Figure 5.7.: *Side and below view during an experiment. The contact area can be seen a clearer circular area in the views from below. The white bar scale is 1 mm.*

5.4.1. Indentation cycle

In figure (5.8), we show a typical cycle of indentation to show its characteristic behavior, for a shell with parameters $E = 250$ kPa, $R = 7$ mm and $h \sim 90\mu$m. Zero indentation is considered as the point where the shell makes contact to the glass plate while approaching, point A in the figure. Before the point A, negative indentation means that the shell is approaching to the glass plate, without contact while the traction machine goes down. When there is no contact, the force is zero. Once there is contact, the force increases (positive force is due to compression). The maximal indentation here is about 1.25 mm, point B. After a dwell time, the machine begins to go up, diminishing the indentation displacement. Initially the force decreases mostly relaxing the elastic energy of deformation, then it begins to detach the shell about point C. The force decreases to zero, then the shell passes to be in tension (negative forces). A local peeling process along the perimeter of the contact area is observed. Once the shell is completely detached from the plate (point D), the force value jumps back to zero.

The shown cycle describes the basic behavior for small and moderate indentations. We will give more details on this concern and on large indentations in section 5.4.4.

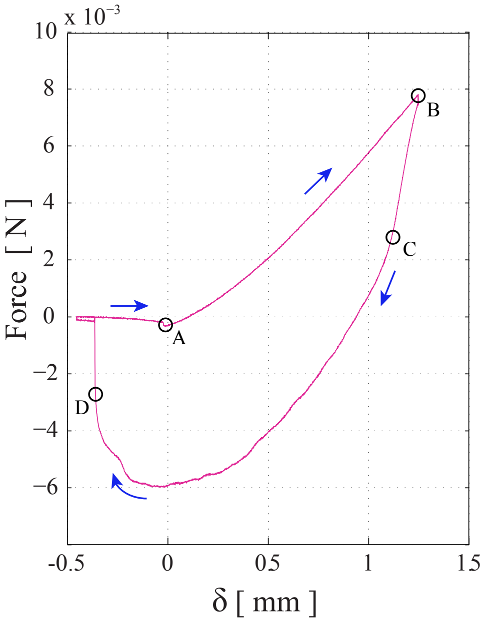

Figure 5.8.: *One cycle: force* vs. *indentation displacement. E = 250 kPa, R = 7 mm, $t \approx 90\ \mu m$.*

With adhesive materials it is important to check that we are not exciting any dynamical behavior due to the viscoelastic properties of the elastomer and that it behaves in a quasi-static manner (see discussion on section 2.2.3). In order to study this question, we performed various experiments varying the indentation velocity.

5.4.2. Dependence on velocity

In figure 5.9, we show various indentation cycles made at different indentation velocities (shell with $E = 250$ kPa, $R = 2.5$ mm, $t \approx 50\mu$m), keeping the maximal indentation nominally constant for all cycles.

A large range of indentation velocities (from 0.001 and 10 mm/min) was tested. Almost the whole range of velocities show a fairly equivalent behavior, i.e. the same hysteresis loop, which is quantitatively related to the adhesion energy. The fastest test of 10 mm/min does not seem to allow a precise control of the displacement of the traction machine. This effect can be observed in the fact that the final indentation δ_{max} of the fastest cycles is different from the slowest ones, though the final indentation was supposed to be imposed equally for all cycles. The hysteresis seems larger too, probably because the velocity is larger and it may change the adhesion energy value, if we are exciting some viscous behavior on the material.

The range where the adhesion energy is almost the same[3] is between 0.001 and 1 mm/min. Since we want to avoid the effects of velocity on the adhesion energy (which constitutes another problem), we choose to work at a fixed indentation velocity for all experiments shown in this chapter. The indentation velocity of 0.1 mm/min, seems to be a good choice, as it allows to stay in the quasi-static regime without taking too long for each experiment.

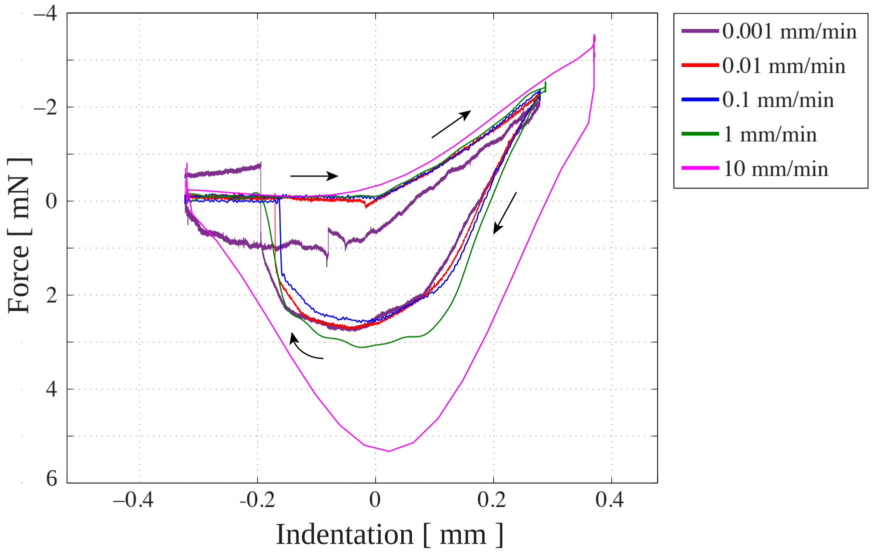

Figure 5.9.: *Various cycles varying indentation velocity. Force* vs. *indentation curves. E = 250 kPa, R = 2.5 mm, $t \approx 50$ μm.*

5.4.3. Contact area

To measure the contact area we used the images taken at a regular interval of time, as those shown in figure 5.7(b). Increasing the contrast on the image we can separate the area "in-contact" and "out-of-contact".

We used two different techniques: first, the old and beloved "by-hand", just with the ImageJ software we draw a circle (or another suitable form) over the edge and measure the area in the scaled images and second, trying to do it in an informatics era fashion, automatically detecting the edge using the contrast of the images. The latter technique was much more complicated because of the lightning reflections disturbing the edge detection.

Another way to measure the contact was to use the side view images (if well aligned to the axis of symmetry of the shell). This method has a larger error because the resolution of the images is not as good, and because of parallax effect.

5.4.4. Varying maximal indentation

In figure 5.10, we show various cycles of indentation of an adhesive shell. Here, we tested a soft spherical shell in a large range of indentation distances, the largest indentation being of the order of half the radius of the shell.

---

[3] Seen from the minimal indentation force value, which is analogous to the pull-off force as it was discussed for the JKR model in section 2.4.2.

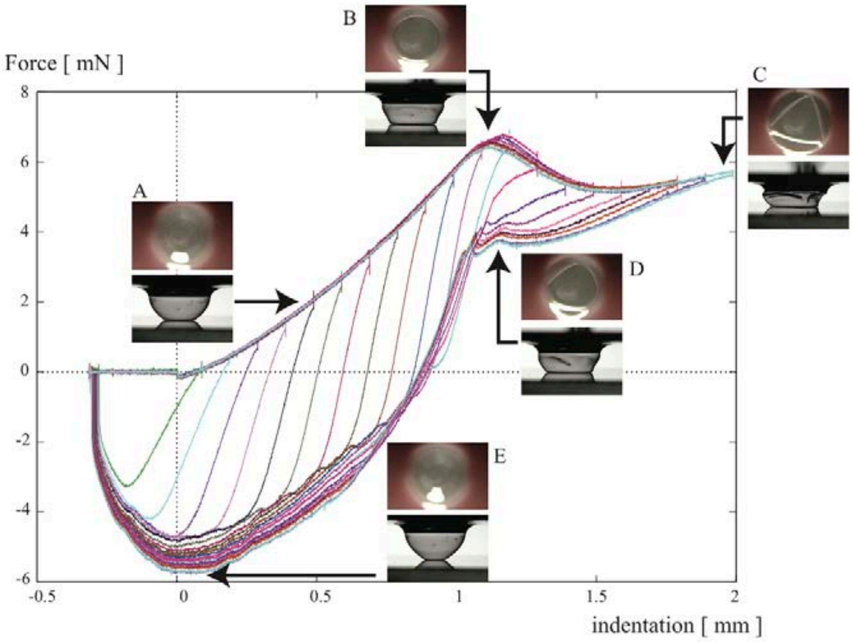

Figure 5.10.: *Various indentation cycles: Force* vs. *indentation. Adhesive shell: E = 250 kPa, R = 5 mm, h* $\approx 50\mu m$. *Images are below and side views.*

Initial contact and small indentations When the shell is not in contact with the glass plate, the force is null. If the shell is soft enough (by means of its Young modulus or its thickness), once it is close enough to the plate, there is a jump in the force[4], showing a little moment when the shell is in tension. The approximate distance between the glass plate and an ideally non-deformed shell is less than 50 μm. Nevertheless, the jump in the force value is due to adhesion that could come from a large range interaction, considering that 50 μm is much greater than the intermolecular scale length.

In figure 5.11, we show two consecutive photos of the sideview of a shell. This shell has parameters: $E = 100$ kPa, $R = 5$ mm and $h \sim 50\mu$m. We approach the shell up to a certain distance (200 μm), and wait (left side photo). After a couple of seconds, if the shell is soft enough, it will deform in order to stick to the surface (right side photo). We stress that the indentation has not changed in the interval between the two photos. This tensile deformation is the reason why there is a little jump on the force while approaching to the plate.

When indentation is increased, the shell passes from being in tension to being in compression, then for moderate indentations, the force increases monotonically with the indentation.

In figure 5.10 we also present some snapshots of the experiment (side and below views) at different points of the indentation cycle. Here, the photos correspond to the last cycle, but they are representative of each cycle. At small indentations (photo A) the contact area is circular and the shell does not loose its spherical form on the non-adhering zone. At another point of small indentation during the detaching process (photo E), the form of the shell is very similar to a sphere, nevertheless the shell is in tension and it is being detached from the plate. This means that close to the contact the shell is deformed and forms a conical frustum close to the adhering

---

[4] Look close to (0,0) in figure 5.10.

area.

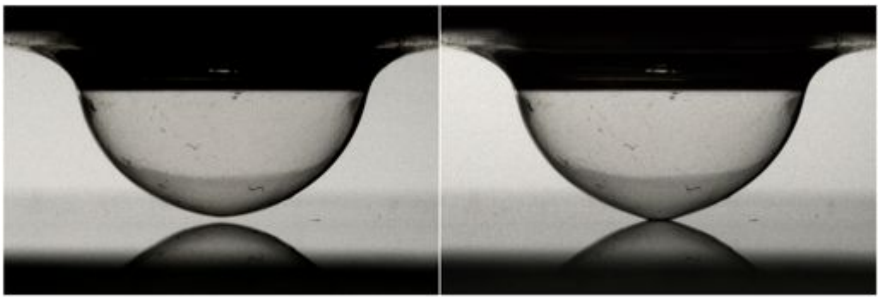

Figure 5.11.: *RTV silicone rubber. E = 100 kPa, R = 5 mm,* $h \sim 30 - 50 \mu m$.

Large indentations Once a certain compressive indentation is reached, about 1mm (20 % of the shell's radius) in this experiment, the non-adhered part of the shell begins to buckle. Note that this is very different from the buckling of the contact area leading to the inverting cap observed in non-adhesive spherical shells. Here, it is the non-contacting part of the shell that buckles. In figure 5.10 (photo B), we can indeed observe that the sides of the shell are not quasi-spherical anymore. It looses its axial symmetry, for instance when increasing the indentation, the shell buckles in forming three folds going inwards. Moreover, we observe that the contact zone changes from a disk to a triangular contact (photo C).
When folding begins to occur (point B) the compressive force diminishes. This is often the case in shell buckling.
In the second part of the cycle, when the indentation is decreased, the triangular contact area begins change its shape by curving around vertices (photo D). At the same time the non-adhering buckled part of the shell unfolds progressively. A little after the photo D, there is a bump on the force: this marks the point where the shell has unfolded completely and its shape is spherical again. The shell is now still in compression but its contact area turns to be circular again. Once the force turns negative, the shell begins to be in tension with the contact area still circular (photo E). A peeling process is observed along the contact line and the force diminishes to zero when the shell is completely detached from the glass plate.

A central characteristic is that we can say the force-indentation curves are placed on top of each other for the increasing δ on one curve and for the decreasing δ on another one. Separated by a short transit curve along which the contact area is roughly constant. This means the elastic energy on the shell, at a given force-indentation point, is the same on every cycle (within a margin of error). So that at a given instant the state of the shell do not depend on the maximal contact area reached during the cycle. This is less exact for large indentation cycles when the shell has buckled (the trajectories are slightly displaced towards lower forces).

5.5. Discussion

5.5.1. Adhesion energy

Trying to apply the compliance method (mention above 5.1) to this experiments, we found many complications:

- difficulty/impossibility to measure the contact radius with precision in the non-adhesive case,
- if we took the Rica-Pauchard's description of a non-adhesive shell, the resultant force for an adhesive experiment diverges for small indentations,
- very complex adhesive force-indentation behavior,
- the behavior of the adhesive shells is geometrically non-linear, due to the very large displacement, though the strains are small.

We now propose a method to measure the adhesion energy using several cycles of indentation. We suppose that there is no dissipation other than adhesion in the hysteresis cycle, in particular we assume that friction is not relevant[5]. This method is a geometrical application of what Hui and coworkers proposed [78] for non-linear systems (see section 5.1.2). Here we a give a very simple derivation of this result (which is quite otherwise involved in the article).

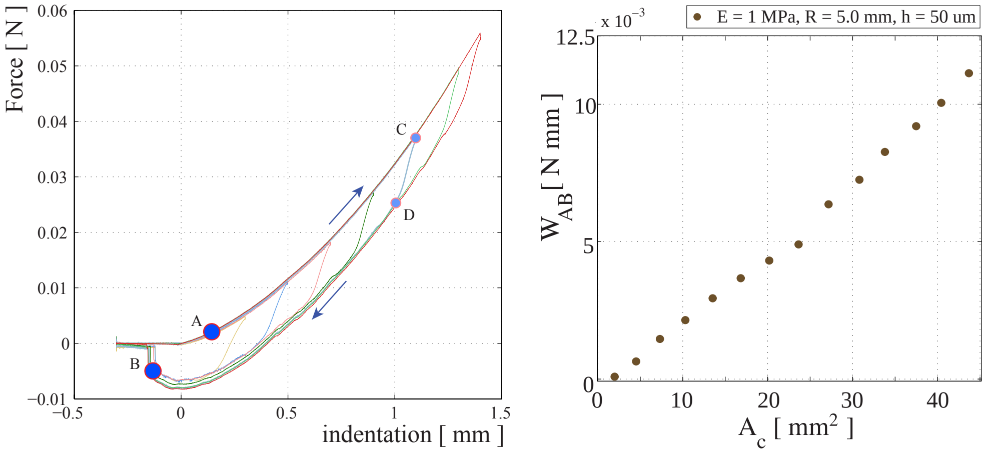

(a) Various indentation cycles

(b) Work of every cycle versus maximal contact area

Figure 5.12.: *PVS. $E = 1$ MPa, $R = 5$ mm, $h \approx 50\mu m$. Indentation velocity $v = 0.1$ mm/min. (a) Indentation force versus displacement curve for various consecutive indentation cycles. The points A and B are arbitrary. (b) Work on every cycle, measured as the integral under every cycle on fig. (a) between the points A and B. A linear regression gives us a adhesion energy $\gamma = 0.26$ N/m.*

Consider a set of indentation cycles as shown in figure 5.12(a). The idea is to measure the work furnished to the system in the interval between two fixed points, on every cycle. In the example figure, we marked them as A and B. The total work furnished to the system between A and B is the area of the cycle between the points A and B,

$$W_{AB} = \int_A^B F(\delta)d\delta$$

with δ the indentation. This work will compensate the elastic energy ($\mathscr{E}_{el}$) and adhesion energy ($\mathscr{E}_{adh}$) difference between the states A and B, plus the adhesion energy dissipated in the cycle $A \rightarrow B$. Let us take as an example one cycle as the one marked with the letters (A,C,D,B) in

---

[5] This hypothesis is fairly valid considering that the peeling of the shell is made at large angles.

figure 5.12(a). In a first phase the shell is advancing, sticking to the plate, with an adhesion energy $\gamma_{advancing}$. The shell reaches the maximal indentation point δ_{max} (point C), with a contact area A_c. Then, the shell recedes, initially the contact area is constant $A_D = A_c$ and the shell is just being elastically deformed. From the point D to B the shell detaches with a dissipation cost in adhesion energy $\gamma_{receding}$ (sec. 2.4.2). The work can be divided in three sections:

$$\begin{cases} W_{AC} &= (\mathscr{E}_{el}(C) - \gamma_{advancing} A_c) - (\mathscr{E}_{el}(A) - \gamma_{advancing} A_A); \\ \\ W_{CD} &= \mathscr{E}_{el}(D) - \mathscr{E}_{el}(C); \quad \text{since the contact area is the same in both states.} \\ \\ W_{DB} &= (\mathscr{E}_{el}(B) - \gamma_{receding} A_B) - (\mathscr{E}_{el}(D) - \gamma_{receding} A_D). \end{cases} \tag{5.5.1}$$

But the adhesion when installing the contact is much less than the receding value, $\gamma_{advancing} \ll \gamma_{receding}$, and we can make the approximation $\gamma_{receding} - \gamma_{advancing} \approx \gamma_{receding} = \gamma$.

Consequently, adding the work during the named three stages (in eqs. 5.5.2), we can rewrite the equation as

$$W_{AB} = \gamma A_c + E(A,B), \tag{5.5.2}$$

with γ the adhesion energy of the elastomer-glass interface and A_c the maximal contact area of the cycle and $E(A,B)$ is a "function" of the points A and B (its elastic and adhesive energies), but it is a constant for every cycle.

This equation is valid for every cycle separately, the only condition is to choose wisely points A and B. The condition is that the elastic energy and adhesion energy (its contact radius) in the point A would be the same for each cycle (and equivalently for point B). Because we have no plasticity or viscoelastic effect, this is equivalent to checking that the force and indentation at point A (and B) are the same at every cycle.

In experiments, we therefore vary the maximal indentation of the cycle, measure the work between A and B from the load-displacement curve and optically determine the maximal contact area A_c for each cycle. In figure 5.12(b), we show W_{AB}, the work between A and B (from experimental data presented on fig. 5.12(a)), as a function of the contact area at the maximal indentation A_c for each cycle[6]. We can see that W_{AB} and A_c increase linearly up to the point where buckling is observed, as expected from (5.5.2). A linear fit for these points gives the adhesion energy $\gamma = 0.26$ N/m.

We repeated the experiment with different material rigidity (and for PDMS) and and geometrical dimensions (different thickness h and radius R). We show on figure 5.13 the dissipation along the cycle W_{AB} as a funciton of the A_c curves for various samples with different Young modulus[7].

In figure 5.13(a), we present data for different geometries with the softest PVS material that we tested. As expected the slopes of the curves (before buckling) are fairly the same for all of the samples, (i.e. their adhesion energy is almost the same). In the case of the smallest shell with a radius of curvature $R = 2.5$ mm the estimated adhesion energy is a little larger (0.214 N/m) than for $R = 5$ mm (0.18 N/m), about a 15% difference.

In figure 5.13(b), the material (PDMS) is the stiffest tested and the adhesion energy is almost the same for both samples 0.090 and 0.081 N/m with a difference of about 10%.

---

[6] Every point represents the integral of a different cycle.

[7] They are separated, because they do not have the same adhesion energy.

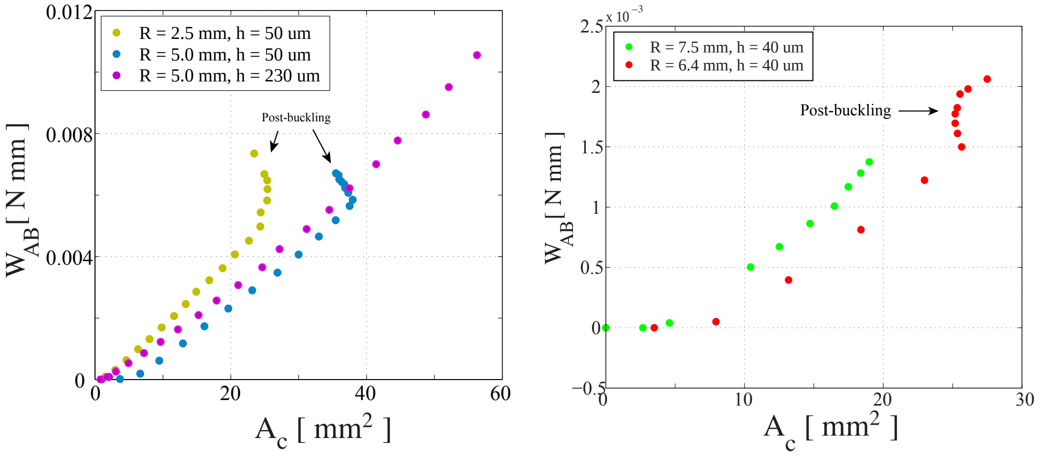

(a) PVS E = 250 kPa (b) PDMS E = 1.2 MPa

Figure 5.13.: *Work done during the indentation cycles including post-buckled cycles. Measured adhesion energy (average slope of the curve, without considering post-buckling cycles for the linear regression) are (a) ● 0.214 N/m, ● 0.186 N/m, ● 0.177 N/m. (b) ● 0.090 N/m, ● 0.081 N/m.*

5.5.2. Post-buckling cycles

We note that the points corresponding to post-buckling do not lie on the straight line in the curves of W_{AB} versus A_c (see figure 5.13). In fact, we do not include these post buckling cycles to estimate the adhesion energy.

This change in behavior is due to the fact that once the shell has buckled, another source of dissipation takes place. This could could be due to the strongly non-linear geometric behavior of the shell (very large displacement) or from self-contact of the shell during the process.

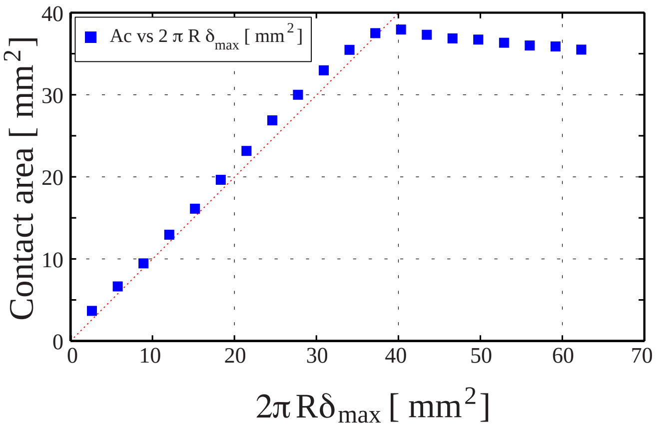

Figure 5.14.: *Maximal contact area as a function of the maximal indentation reached during every cycle. PVS E = 250 kPa, R = 5 mm, h* $\sim 50\mu m$*. Dotted red line is the* $y(x) = x$ *line.*

In figure 5.14, we show the contact area measure at the maximum indentation point as a function of $2\pi R\delta_{max}$, where δ_{max} is the maximal indentation for each cycle (every point in the plot represents a cycle). Before buckling, the maximal contact area of every cycle increases linearly with the maximal indentation. This can be seen in a simple geometrical relation, valid in the range of small contact radius $a \ll R$, *and null adhesion*, which is the case when the shell is advancing and sticking to the glass plate (we neglect $\gamma_{advancing}$):

$$\delta = R\left(1-\sqrt{1-\left(\frac{a}{R}\right)^2}\right) \sim \frac{a^2}{2R}.$$

The contact area increases $A_c = \pi a^2 \sim 2\pi R\delta_{max}$ increases in a fairly linear manner (red dotted line) with the maximal indentation δ_{max} as observed in the first regime in figure 5.14.

After buckling, the contact area does not increase with the maximal indentation but keeps a constant value (slightly decreases as δ_{max} increases). In fact, the contact changes its shape (into a triangular form see insets in figure 5.10), at the cost of some points advancing and other ones receding. We cannot trust anymore our assumption of constantly advancing front up to the maximum indentation $\delta = \delta_{max}$ and our approach cannot apply. The adhesion energy must be determined using experimental points before buckling.

5.5.3. Dependance on the shpae of the shell?

Note that the argument leading to equation (5.5.2) does not rely on any assumption on the geometry of the system. This is the great advantage of this approach.

We checked this using shells with non-axisymmetric shapes (and in fact non-uniform thickness). Two shells with an ellipsoidal-like form were tested. The first was made casting the polymer over a drug capsule (figs. 5.15(a), 5.15(b)), the resulting ellipsoid has semi-major and semi-minor axes of 1 and 0.5 cm, with 5 mm height. The second was casted over a M&M© (figs. 5.15(c), 5.15(d)) candy with semi-major and semi-minor axes of 0.95 and 0.75 cm and 7.5 mm height. Its local radius of curvature around the apex is 5 mm.

The capsule has a quasi-cylindrical form with rounded borders and the candy is irregular and pretty similar to an egg shape. The capsule shaped shell has some “imperfections” on the thickness (two white dots, view from below), they come from the casting mold.

The measurements of dissipation of a cycle as a function of the maximal contact area (measured on images) for both shapes are presented in figure 5.16. We can see that the slope of both curves is the same, and using all data at once to fit it, it gives an adhesion energy $\gamma = 0.073$N/m. The casting material for the shells are in fact the same as in figure 5.13(a), but here its adhesion energy is about three times smaller. We do not really understand what changes the value of the adhesion energy, since they are made from the same material. One possibility is that the waiting time before the experiment after casting was different. In experiments from figure 5.13(a) the shells were older (several days and the shells were tested many times) compared to the capsules (only few hours, not many tests were done before). In practice we have observed that the PVS elastomer ages on large timescales, changing its surface and stiffness properties. Also releasing silicon oil, and swelling it if in contact to another piece of polymer (PVS or PDMS).
More work on the dependance dependence of the energy release rate components on geometry are nevertheless necessary to provide a more grounded conclusion.

5.6. Measurement with a full sphere

How does our method work in the classical JKR geometry? We tested it on a full hemi-spherical probe indented on a glass plate. In figure 5.17(a), we show a set of various indentation cycles,

(a) Capsule contact view (b) Capsule sideview

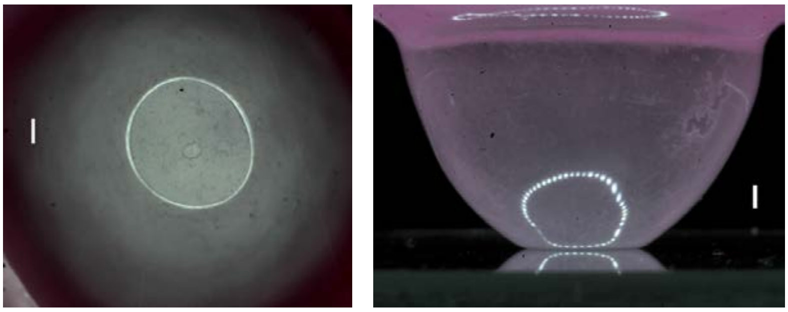

(c) Candy contact view (d) Candy sideview

Figure 5.15.: *Side and below view during an experiment. The contact area can be seen a clearer circular area in the views from below. The scale is 1 mm on every photo.*

and in figure 5.17(b), we show the work done over every whole cycle as a function of the contact area for a full spherical probe. We have chosen a range of indentation and of contact area similar to the case of shells. The measure of dissipation is very noisy, and a value for adhesion cannot be inferred from these data. The hysteresis cycles are so small compared to the maximal indentation force ($\sim$ 1 N), that the effect of adhesion becomes almost invisible to the eye in the force-indentation cycles in 5.17(a). This is why our method leads to very noisy measurements and fails to provide a measurement of adhesion.

We see that the method developed here is not adapted to a JKR test, but is very versatile in the case of compliant shells where large contact areas (necessary for a precise measurement of the dissipation in the cycle) are not associated with very large force.

To be sure that the geometrical conditions of the full hemi-sphere are appropriate to test our model, we probe our data with the JKR method, see figure 5.17(c). The theoretical prediction shows a good agreement to our experimental data, which corroborates the theory at the same time, it probes that the dimensions of the full shell are suitable to measure the adhesion[8].

---

[8] This sphere is quite large compare to the typical size (millimetric size) of spheres used to do JKR tests.

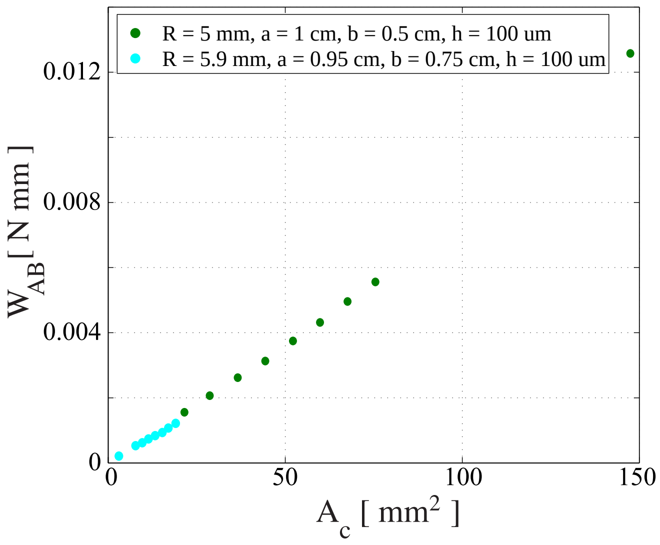

Figure 5.16.: *PVS E = 250 kPa. Capsule (●) and M&M© shape (●), $\gamma = 0.073$ N/m.*

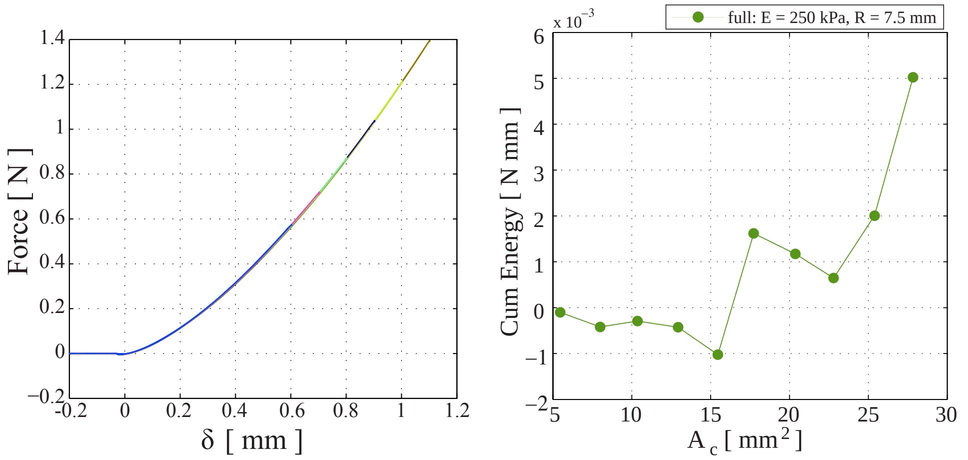

(a) Various indentation cycles for a full sphere (b) Work on every closed cycle *vs* maximal contact area

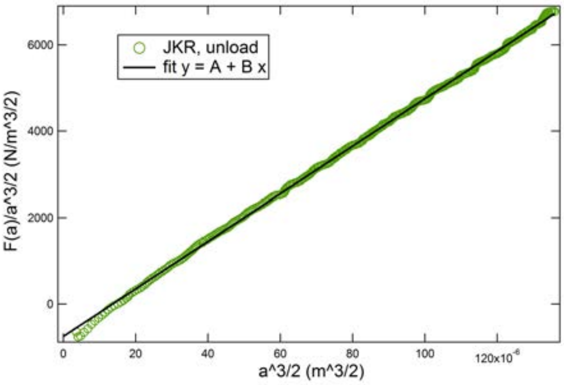

(c) Testing JKR theory on a full sphere

Figure 5.17.: *PVS E ∼ 250 kPa, R = 7.5 mm. Full hemisphere indented on a glass plate. (a) The hysteresis loop being very small does not allow our method to catch the adhesion energy value, as it is shown in (b), it measures just noise. (c) Measure of the adhesion energy using JKR theory, the fit parameters A and B are homogeneous to* $E = 220$ *kPa and* $\gamma = 0.1$ *N/m.*

5.7. Conclusions

In this chapter we show a new perspective for measuring the adhesion energy of a soft material on a rigid surface. We use a thin shell made of an elastomer and perform a set of indentation cycles with increasing contact area. We measure the work provided to the system on every cycle (from the force-displacement curve) and the maximal contact area reached during the indentation process (from image processing). These measurements allow to measure the adhesion energy without any knowledge of the non-linear elastic response of the shell, nor its material constitutive stress-strain law (possibly non-linear).
The assumptions for this method (applied from [89]) are:
- During the cycles, each point of the contact line continuously advances, up to the maximum indentation (the maximum area of contact A_c) and then (return part of the cycle) the contact line continuously recedes at each point.
- The surface energy gain in the advancing state is negligible in comparison to the adhesion energy in the receding phase. This is often the case in adhesion.
- The material response is elastic (no plasticity, no viscous dissipation) although it may be non-linear.

As a result of this last condition, all cycles are share the advancing and receding branch, this means that at a given indentation and force, the state of the shell resembles at each cycle, not matter if the shell had gone through a larger or smaller maximal area of contact at the point of maximal indentation. In our experiments, this method failed once the shell has buckled, because the contact area rearranges after that event, with simultaneous advancing and receding of different zone of the contact line.
In this method there are two features of interest, firstly we do not need to know in detail the mechanical behavior of the shell, which is complicated and involves non-linear geometric and elastic behaviors, and secondly the fact of using a slender material amplifies the adhesion-to-elasticity ratio. It means that the contact areas are larger than the ones reached in a standard JKR test for a given range of forces. This potentially allows to test adhesion on materials using a very gentle force.

6. Conclusion

In this manuscript, we have studied two classical configurations used in the measurement of adhesion, but with a focus on some original questions. We first presented a study of the role of friction during the peeling of an adhesive elastomeric strip and, in a second part, the indentation of an adhesive thin shell (viewed as a modified JKR test). In the first two chapters we have shown how frictional sliding may dramatically modify the peeling processes of an adhesive strip at low angle. In the particular case of particular at zero-angle (chapter 3), we have observed that the system never reaches the steady-state peeling expected from the classical study from Kendall. Instead, a catastrophic detachment occurs during a phase where the force was continuously increasing. This sudden detachment is reminiscent of the recent work from Crosby and collaborators based on an accumulation of elastic energy over the whole adhesion area. However, a decreasing portion of the strip remains at rest during this phase, while the complementary portion slides on the substrate without loosing contact. The sliding zone advances progressively, reducing the portion of the strip which is at rest. The sudden detachment occurs when the sliding front reaches the end of the strip. The sliding of such elastomers leads to a nearly constant shear stress τ on the interface, which we estimate by observing the gradient of deformation of the strip. The final detachment force is therefore $F = \tau w_o L_a$, where w_o, L_a are the strip width and initially adhering length. This phenomenon is very different from the extrapolation of Kendall's classical extensional peeling to a zero peeling angle, but also from the alternative frictionless catastrophic scenario from Crosby and colaborators. We discussed a possible explanation for this difference based on "adhesion rheology", which should be tested through more local tools. More generally, a physico-chemical description of the nature of friction of soft elastomer (which would predict the value of τ) would be valuable.

In chapter 4, we extended our observations to peeling at finite angle. We observe a steady state peeling (the force reached a plateau), but in many cases we measured unexpected high forces in comparison with the classical extensional model. These high values are due to the extra dissipation generated by frictional sliding, which becomes dominant for low peeling angles, and diverges when the angle vanishes. A model including this dissipation correctly describes the phenomena, with some peculiar properties. Curiously the peeling force predicted in the case of sliding is independent of the value of the sliding shear stress τ. As the peeling angles goes to zero, the extension of the sliding zone would increase infinity. In practice, the sliding front reaches the end of the strip before steady state is attained, and we therefore recover the zero-angle process even at finite angle.

This framework also includes conditions where the classical peeling law from Kendall should be obeyed even at very low angle. When the peeling force in the non-sliding hypothesis (classical peeling) is sufficiently small compared to friction, sliding should indeed never occur. This remark leads to an apparently paradoxical conclusion: classical "frictionless" description of peeling should actually be correct in the limit of very large friction, and not in the limit of zero friction. Friction is indeed necessary to balance the component of the peeling force parallel to the substrate. But this friction does not contribute to dissipation as long as peeling occurs without sliding (in the case of rather large friction). Coming back to geckos feet presented in the

introduction, we expect friction to play an important role in their adhesive properties.
In principle, frictional sliding should occur in all situations involving debonding of a soft polymer. For instance, stretchable electronic devices often involve electric circuits made of stiff thin films coated on soft substrates. Upon compression delamination blisters are formed [5]. Curiously, the shape of these blisters seems experimentally independent on the elastic properties of the substrates. Dissipation through friction may however cancel exactly the variation of the elastic energy of the substrate as we have predicted in several on several simplified configurations (annexe B). It would therefore be interesting to clarify this question in a general situation, and to provide an exhaustive review of the effect of frictional dissipation on soft adhesive structures.

In a second part of the thesis, we aimed at generalizing the JKR indentation test to shells. The point was to exploit the structural softness of shells to assess weak adhesion forces that may be difficult to measure through standard tests with plain spheres. The theoretical description of this strongly non-linear problem is however very challenging (even without adhesion). However here we take advantage of a very versatile and simple method to circumvent the complex mechanical response of the shell. We measured the dissipation in an indentation cycle and find that this dissipation is proportional to the maximal area of contact during the cycle. Indeed, dissipation is here only due to adhesion hysteresis, which we can therefore extract directly. This method allows us to measure adhesion energy without any calculation of the elastic response. We tested this idea with elastic sticky shells with different radii and thicknesses, and also with non-spherical shapes and of non-uniform thickness. Although our work is a first step towards demonstrating the validity of the method, it should be confirmed by more experiments (some discrepancies on the value of adhesion energies have still to be clarified). Since thin shells are much softer than a sphere, this powerful method may be useful to estimate weak adhesion energies or to probe delicate substrates such as biological tissues.

A. Materials characterization

A.1. Measurement of the Young modulus

To measure the Young modulus of a material we can use a simple uniaxial tensile test [90], with a strip of material clumped by the two extremes with a traction machine. We do several cycles of deformation to verity there is no plasticity in the material or damage of any sort.

In this work we focus in using elastomers, so the linear elastic deformations can be larger. A large strain study is presented on the chapter 3, where we show that, linear behavior is far too simple. A more realistic model is to consider a 5th order polynomial to describe the force-displacement relation. For more details, see section 3.6.1.

In figure A.1, we show the superposition of six experimental stress-strain curves. The curves are limited to small deformations (less than 10%) $\varepsilon_{xx} = \frac{d}{L}$, where d is the displacement with respect to the equilibrium length of the strip. Here, L is the length of the strip, h is its thickness and w its width. With a traction machine (Instron), we measure the tensile force, to compute then the tensile stress $\sigma_{xx} = \frac{F}{hw}$.

From linear elasticity, we know that the proportionality constant that relies the tensile stress to the strain is the Young modulus E,

$$\sigma_{xx} = E\varepsilon_{xx}.$$

We do a linear regression of the experimental data to obtain the Young modulus E.

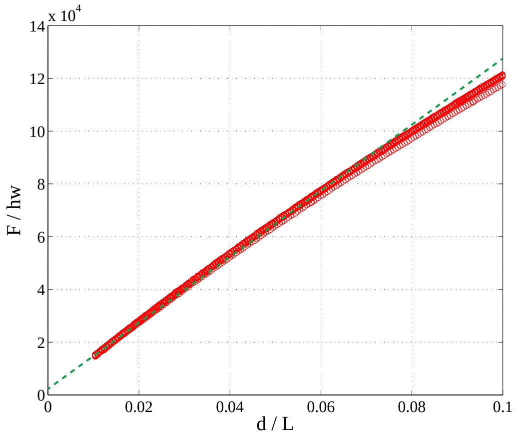

Figure A.1.: *Superposition of 6 stress-strain curves. The slope of the curve for small strains gives us the Young modulus of the material, E = 1.25 MPa in this case, linear regression shown in green dashed line.*

A.2. Viscoelasticity

The chosen material we are working with is an elastomer. Which being at room temperature is in rubbery state ($T_g \sim -100°\mathrm{C}$).

In figure A.2, a shear rheometry test of the casted elastomer (PVS shore A 08) is shown[1]. In red, we plot the shear modulus and in blue its viscosity as a function of the shear rate.

In the case of an incompressible elastomer, the shear modulus $G' = \mu$ is simply one third of the Young modulus, $\mu = E/3$. In the tested frequency range, $G' \sim 100$ kPa, which in agreement to the measures of Young modulus (around 250-300 kPa) made with traction tests. The loss modulus G'' changes slowly. The solicitation velocities we are using in experiments are out of range for the shown data here. The shear rates we excite are of the order or smaller than $5 \cdot 10^{-2}$ Hz

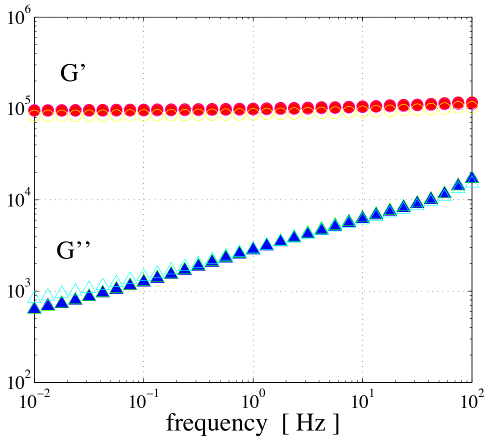

Figure A.2.: *Storage and loss modulus, G' and G'' respectively, as a function of the exciting frequency for a shore A 08 PVS sample.*

---

[1] Shear rheometer model: MCR 501 Anton Paar

B. Frictional sliding in toy models

Here we compute the dissipation due to frictional sliding in other situations than the peeling of a polymer strip from a rigid plate, and show how it modifies the energy. We thank Herbert Hui for suggesting and helping with these computations.

We consider simplified problems, where we can use the approximation where the sliding occurs on a very large distance ℓ compared to the shear-lag process zone ℓ_{lag}. Even more, we assume that the elastic medium is thin in comparison with the distances ℓ over which shear stresses are applied, so that we can use

$$h\frac{d\sigma_{xx}}{dx} = -\tau \tag{B.0.1}$$

We also assume that the substrate does not deform in the vertical direction.

B.1. Some examples

B.1.1. Peeling an inextensible (infinitely flexible) strip from a soft elastic (thin) substrate

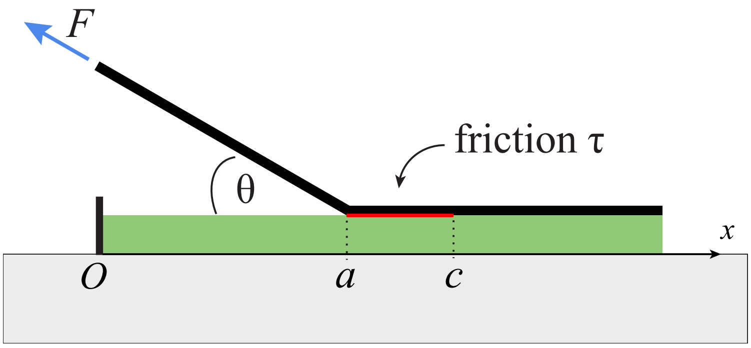

We assume that the substrate only deforms along x. This is due to some vertical forces (like a suction) which prevent vertical movements and bending of the substrate. This simplifying hypothesis would not be very easy to obtain in experiments, but it simplifies greatly the computation. Friction shear stress is τ applies between $x = a$ and $x = c$. Young modulus of substrate is E_s, and thickness h_s. The stress distribution in the substrate is due to the horizontal part of the force is

- $\sigma_{xx} = -\tau(c-a)/h_s$ for $x \leq a$,
- $\sigma_{xx} = \tau/h_s(x-c)$ for $a \leq x \leq c$,
- $\sigma_{xx} = 0$ under the part $x \geq c$ because the strip is assumed to be inextensible.

Because we have the horizontal displacement $u(x)$ obeys $du/dx = \sigma_{xx}/E_s$, we find

- $u(x) = -\tau x(c-a)/E_s h_s$ for $x \leq a$,
- $u(x) = \tau(x^2 - 2cx + a^2)/2E_s h_s$ for $a \leq x \leq c$ using continuity of u in $x = a$,
- $u(x) = -\tau(c^2 - a^2)/2E_s h_s$ for $x \geq c$.

We now compute the corresponding total elastic energy.

$$\mathscr{E}_s = \int_0^c h\sigma_{xx}^2/2E_s dx = \frac{\tau^2(c-a)^2}{E_s h_s}a + \frac{1}{2}\int_a^c h\sigma_{xx}\frac{du}{dx}dx$$

but we can integrate by part the integral and find, using (B.0.1)

$$\frac{1}{2}\int_a^c h\sigma_{xx}\frac{du}{dx} = [h\sigma_{xx}u]_a^c - \frac{1}{2}\int_a^c (-\tau)udx$$

and finally a nice simplification leads to

$$\mathscr{E}_s = \frac{1}{2}\int_a^c \tau u(x)dx \tag{B.1.1}$$

An interesting quantity is the variation of this energy when we imagine a general variation of the friction zone (i.e. when a and c are varied by δa and δc respectively).

$$\delta\mathscr{E}_s = \frac{1}{2}\left(\tau u(c)\delta c - \tau u(a)\delta a\right) + \int_a^c \tau\delta u dx$$

where we can use $\delta u = \tau(a\delta a - x\delta c)/E_s h_s$ by derivation the expression of $u(x)$ for $a \leq x \leq c$. we therefore find

$$\int_a^c \tau\delta u dx = \tau[a\delta a(c-a) - \delta c(c^2 - a^2)/2]/E_s h_s = \tau[u(c)\delta c - u(a)\delta a]$$

so that this term is equal to the other term so that finally we can rewrite the sum of the contributions into :

$$\delta\mathscr{E}_s = \int_a^c \tau(\delta u)dx = \tau[u(c)\delta c - u(a)\delta a] \tag{B.1.2}$$

where the equality is really only true for the displacement field $u(.)$ that we have computed.

We now consider a steady-state peeling configuration, at force F with an angle θ. Global horizontal force balance shows that $F\cos\theta = \tau(c-a)$, which implies that $a-c$ remains constant, as expected. Consider a displacement δ_a of the peeling front ($\delta a = \delta c$). The operator works an ammount $F(1-\cos\theta)\delta_a$, so that the energy balance reads :

$$\frac{F}{w}(1-\cos\theta) = \delta\mathscr{E}_s + \gamma\delta_a + \delta W_f$$

where W_f is the work dissipated by friction. Assuming sliding in the frictional zone with a shear stress τ, the sliding displacement is the difference between the displacement of the top layer and the substrate.

$$\delta W_f = \int_a^c -\tau(\delta u - \delta u_{top})$$

Now we use the fact that the strip is inextensible, so that $\delta u_{top} = 0$ and we find that

$$-\delta W_f = \int_a^c -\tau \delta u dx = \delta \mathscr{E}_s$$

In other words the variation of elastic energy during displacement is completely dissipated in frictional sliding.

This leads to

$$\frac{F}{w}(1-\cos\theta) = \gamma$$

which is equivalent to the case of a rigid substrate (with no friction). Frictional dissipation magically absorbs exactly the contribution of substrate elastic energy to the problem.

B.1.2. Blistering of an inextensible flexible strip from a soft (thin) substrate

We consider the blister of a thin inextensible flexible strip attached to a soft (but thin) substrate. The system is compressed. Similar stress distribution are found in the substrate, and equations (B.1.1) and (B.1.2) still hold.

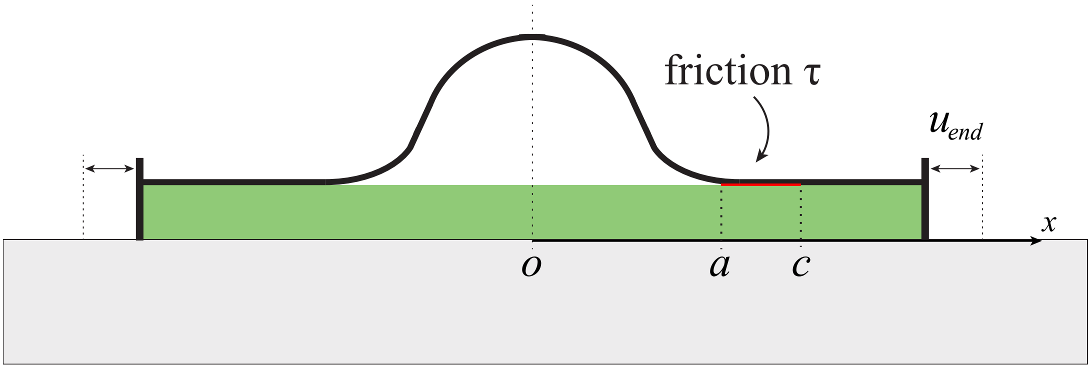

Here we wish to determine the amplitude A and width $2a$ of blister by minimizing the global energy. Consider a variation of the blister half width δa, for an imposed fixed (negative) displacement of the end of the strip

$$-u_{\text{end}} = \tau(c^2 - a^2)/2E_s h_s$$

The elastic energy variation now includes bending energy $\mathscr{E}_b$ in addition to the substrate energy, and writes

$$-\delta\mathscr{E}_b - \delta\mathscr{E}_s = \gamma\delta a + \delta W_f$$

But here again, we find that $\delta\mathscr{E}_s = \delta W_f = \int_a^c \tau\delta u dx$, so that we are lead to

$$\delta\mathscr{E}_b = \gamma\delta a$$

which expresses an energy balance between bending and adhesion energy.

In the limit of small amplitude blisters $A/a \ll 1$, we can compute $\mathscr{E}_b = \int_0^a dx B\kappa^2/2$, where κ is the curvature of the strip. Because in this limit the strip vertical displacement is $y = A[1+\cos(\pi x/a)]/2$, $\kappa = -A\pi^2/a^2\cos(\pi x/a)/2$ and the energy reads

$$\mathscr{E}_b = \frac{B}{2}\frac{\pi^4 A^2}{4a^4}\int_0^a \cos^2(\pi x/a)dx = B\frac{\pi^4 A^2}{16a^3}$$

Note that the curvature in $x = a$ is $\kappa_a = A\pi^2/2a^2$

The amplitude A is determined by the the fixed displacement condition, given the fact that the strip is inextensible :

$$u_{\text{end}} = \int_0^a -\frac{1}{2}(\frac{dy}{dx})^2 dx = -\frac{1}{2}\frac{\pi^2 A^2}{4a^2}\int_0^a \sin^2(\pi x/a)dx = -\frac{1}{16}\frac{\pi^2 A^2}{a}$$

and

$$A^2 = (-u_{\text{end}})\frac{16a}{\pi^2}$$

so that the bending energy is

$$\mathscr{E}_b = B\frac{\pi^2}{a^2}(-u_{\text{end}})$$

The energy variation becomes

$$2B\frac{\pi^2}{a^3}(-u_{\text{end}}) = \gamma$$

or equivalently, because $-u_{\text{end}} = a^3\kappa_a^2/4\pi^2$,

$$\frac{B}{2}\kappa_a^2 = \gamma \tag{B.1.3}$$

Here we have recovered the elasto-capillary condition, which is expected if the substrate is rigid (and frictionless).

B.1.3. Peeling a soft strip from a rigid substrate

Can we rephrase our result in term of friction leading to complete dissipation of the energy in the strip?

We have computed before the energy balance

$$f(1+\frac{f}{Eh} - \cos\theta) = \frac{\delta\mathscr{E}_s}{\delta a} + \gamma + \frac{\delta W_f}{\delta a}$$

where we have noted $f = F/w$, and found by direct computation of the sliding displacement

$$\frac{\delta W_f}{\delta a} = \frac{(f\cos\theta)^2}{2E_f h_f}$$

The elastic energy variation was found (in steady state) by simply the difference of section δ_a initially stress-free, moved into an area under force f.

$$\frac{\delta\mathscr{E}_s}{\delta a} = \frac{f^2}{2Eh}$$

Here we see that the energy release rate due to the stretching

$$\frac{\delta\mathscr{E}_s}{\delta a} - \frac{f^2}{Eh} = -\frac{f^2}{2Eh} \neq -\frac{\delta W_f}{\delta a}$$

of the strip is not entirely dissipated into friction, due to the $\cos\theta$ factor.

If it had been the case, we would have recovered the inextensible equation $f(1-\cos\theta) = \gamma$.

B.1.4. Half-blister of a soft and flexible strip from a rigid substrate

We consider a half blister with an imposed horizontal displacement with no rotation.

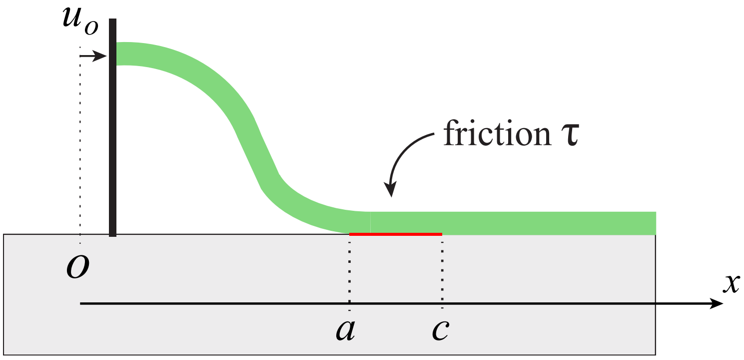

The compression elastic energy in the elastic strip also follows equation (B.1.1) with a uniform compression in the buckled part ($x \leq a$), decreasing in the frictional contact zone ($a \leq x \leq c$), and no compression for $x \geq c$.

The energy conservation writes :

$$0 = \gamma \delta a + \delta W_f + \delta \mathscr{E}_b + \delta \mathscr{E}_s$$

with here the exact cancellation $\delta W_f + \delta \mathscr{E}_s = 0$ because the substrate is infinitely rigid. So that we recover

$$-\frac{\delta \mathscr{E}_b}{\delta a} = \gamma$$

To obtain the shape of the blister, we must use the bending energy which also takes the form

$$\mathscr{E}_b = B \frac{\pi^4 A^2}{16 a^3}$$

But there are now some differences with the other blister problem. The plate equation for low angle imposes that the axial force depends on the blister size:

$$\tau(c-a)/B = \pi^2/a^2.$$

The imposed displacement at the begining of the strip is equal to the geometrical displacement $\frac{1}{16}\frac{\pi^2 A^2}{a}$ plus the global strain-induced displacement in the frictional zone:

$$u_0 = \tau \frac{(c^2-a^2)}{2Eh} + \frac{1}{16}\frac{\pi^2 A^2}{a}$$

In practice the first term is negligible in comparison to the second term. extracting $c = a + B\pi^2/(\tau a^2)$ leads to $c^2 - a^2 = 2B\pi^2/(\tau a) + B^2\pi^4/(\tau^2 a^4)$ and finally

$$u_0 = \frac{1}{2Eh}\left(\frac{2B\pi^2}{a} + \frac{B^2\pi^4}{\tau a^4}\right) + \frac{1}{16}\frac{\pi^2 A^2}{a}$$

from which we can extract the amplitude A, and get to

$$\mathscr{E}_b = \frac{B\pi^2}{a^2}\left(u_0 - \frac{B^2\pi^4}{2Eh\tau a^4} - \frac{B\pi^2}{Eha}\right)$$

The energy equation $-\frac{\delta\mathscr{E}_b}{\delta a} = \gamma$ at fixed u_0 is

$$-\frac{\delta\mathscr{E}_b}{\delta a} = \frac{B\pi^2}{a^3}\left(2u_0 - 6\frac{B^2\pi^4}{2Eh\tau a^4} - 3\frac{B\pi^2}{Eha}\right) = \gamma$$

We have found above that u_0 is related to amplitude and width a, so that

$$\frac{B\pi^2}{a^3}\left(\frac{1}{8}\frac{\pi^2A^2}{a} - 4\frac{B^2\pi^4}{2Eh\tau a^4} - \frac{B\pi^2}{Eha}\right) = \gamma$$

and because $\kappa_a = A\pi^2/2a^2$,

$$\frac{B}{2}\kappa_a^2 = \gamma + \frac{B\pi^2}{a^3}\left(4\frac{B^2\pi^4}{2Eh\tau a^4} + \frac{B\pi^2}{Eha}\right)$$

Comparison with equation (B.1.3) shows that this lead to a different solution here (not the bending elasto-capillary condition), because of the extra terms, even if the stretching energy was consumed in frictional dissipation. In practice these correctives terms are very small (on the order of $Eh^5/\tau a^3A^2$ and h^2/A^2) as soon as the amplitude A becomes larger than the thickness h of the strip.

B.2. A general approximation

The conclusion of previous examples is that in some case frictional sliding exactly balances extensional energy release rate, and in some cases only partially compensates for it. Here we give a general case where the balance is perfect. The typical case is that of an extensible substrate ion which is deposited a very flexible, but inextensible strip.

We consider two materials (1 and 2) initially bonded along an interface, and the propagation along that interface of a separating front. We consider that adhesion is represented as a cohesive zone (to prevent divergences), and that sliding may occur, possibly on a large scale.

We consider an extension by δa of the debonded zone, and write energy balance during that event: On the solid (1),

$$\delta W^{Op\to(1)} + \int_{\text{surface}(1)-(2)} \left[\tau_x^{(2)\to(1)}\delta u_x^{(1)} + \tau_y^{(2)\to(1)}\delta u_y(1)\right] = \delta\mathscr{E}_{(1)}$$

where $\tau^{(2)\to(1)}$ are the surface stresses applied at the interface, by medium (2) on medium (1). $\delta u_x^{(1)}$ is the displacement due to the movement of the debonding front by δa and $\delta W^{Op\to(1)}$ is the external work (by the Operator) directly on medium (1).

Symmetrically we can write

$$\delta W^{Op\to(2)} + \int_{\text{surface}(2)-(1)} \left[\tau_x^{(1)\to(2)}\delta u_x^{(2)} + \tau_y^{(1)\to(2)}\delta u_y^{(2)}\right] = \delta\mathscr{E}_{(2)}$$

But in general one proceeds to a global energy balance, which can be rewritten, using the fact that $\tau^{(1)\to(2)} = -\tau^{(2)\to(1)}$, and denoting $\delta W^{Op\to(1)} + \delta W^{Op\to(2)} = \delta W^{Op}$

$$\delta W^{Op} + \int_{\text{surface}(1)-(2)} \left[\tau_x^{(2)\to(1)}(\delta u_x^{(1)} - \delta u_x^{(2)}) + \tau_y^{(2)\to(1)}(\delta u_y^{(1)} - \delta u_y^{(2)})\right] = \delta\mathscr{E}_{(1)} + \delta\mathscr{E}_{(2)}$$

We note that the contribution to the integral is zero unless $\delta u_x^{(1)} \neq \delta u_x^{(2)}$, in other term sliding, or unless $\delta u_y^{(1)} \neq \delta u_y^{(2)}$ (in other term opening of the gap between the media).

Approximation

We suppose here that medium (2) is inextensible, but very flexible. We therefore can make the approximation that in parts where there is debonding,

$$\delta u_y^{(1)} \gg \delta u_y^{(2)}$$

and in the sliding part,

$$\delta u_x^{(1)} \ll \delta u_x^{(2)}$$

The interaction integral now becomes

$$\int_{\text{surface}(1)-(2)} \left[\tau_x^{(2)\to(1)}(\delta u_x^{(1)} - \delta u_x^{(2)}) + \tau_y^{(2)\to(1)}(\delta u_y^{(1)} - \delta u_y^{(2)})\right] =$$
$$\int_{\text{surface}(1)-(2)} \tau_x^{(2)\to(1)} \delta u_x^{(1)} + \int_{\text{surface}(1)-(2)} -\tau_y^{(2)\to(1)} \delta u_y^{(2)}$$

If we rewrite the energy balance on medium (1) :

$$\delta W^{Op\to(1)} + \int_{\text{surface}(1)-(2)} \left[\tau_x^{(2)\to(1)} \delta u_x^{(1)}\right] = \delta \mathscr{E}_{(1)}$$

This equality can be substracted to the global energy balance :

$$\delta W^{Op\to(2)} + \int_{\text{surface}(1)-(2)} \left[\tau_y^{(1)\to(2)} \delta u_y^{(2)}\right] = \delta \mathscr{E}_{(2)}$$

In this last equation the integral only contains work of forces perpendicular to the interface. These are the forces responsible for adhesion, so that

$$\int_{\text{surface}(1)-(2)} \left[\tau_y^{(1)\to(2)} \delta u_y^{(2)}\right] = -\gamma w \delta a,$$

where w is the width of the contact zone. Finally we are lead to the equation on energy release rate that one could have in absence of both frictional dissipation, and contribution to the energy release rate from medium (1).

$$\delta W^{Op\to(2)} - \delta \mathscr{E}_{(2)} = \gamma w \delta a$$

We have written a general approximation for which the frictional dissipation exactly balances the energy release rate due to the elastic energy of the substrate. This is based on the fact that one medium is very soft in the direction perpendicular to the interface, but very stiff parallel to the interface.

C. Paper published in *Soft Matter*

C.1. Effect of friction on the peeling test at zero-degrees

We describe the peeling of an elastomeric strip adhering to a glass plate through van der Waals interactions in the limit of zero peeling angle. In contrast with classical studies on adhesion that predict a saturation of the pulling force in this lap test configuration, the force continuously increases, while a sliding front propagates along the tape. The strip eventually detaches from the substrate when the front reaches its end. Although the evolution of the force is reminiscent of recent studies involving a compliant adhesive coupled with a rigid backing, the progression of a front does not follow the same mechanism. To interpret this behavior, we estimate the local shear stress at the interface by monitoring the deformation of the strip. Our results are consistent with a nearly constant friction stress in the sliding zone in agreement with other experimental observations where adhesion and friction are observed.

Reference [91]
Effect of friction on the peeling test at zero-degrees
Suomi Ponce, José Bico and Benoît Roman.
Soft Matter, 2015, Advance Article, DOI: 10.1039/C5SM01203A.
Received 19 May 2015, Accepted 17 Sep 2015. First published online 17 Sep 2015.

Effect of friction on the peeling test at zero-degrees[†]

Suomi Ponce, José Bico and Benoît Roman*

Received Xth XXXXXXXXXX 20XX, Accepted Xth XXXXXXXXX 20XX
First published on the web Xth XXXXXXXXXX 200X
DOI: 10.1039/C5SM01203A

[Ponce *et al., Soft Matter*, 2015, Advance Article, DOI: 10.1039/C5SM01203A.] We describe the peeling of an elastomeric strip adhering to a glass plate through van der Waals interactions in the limit of zero peeling angle. In contrast with classical studies that predict a saturation of the pulling force in this lap test configuration, the force continuously increases, while a sliding front propagates along the tape. The strip eventually detaches from the substrate when the front reaches its end. Although the evolution of the force is reminiscent of recent studies involving a compliant adhesive coupled with a rigid backing, the progression of a front is in contradiction with such mechanism. To interpret this behavior, we estimate the local shear stress at the interface by monitoring the deformation of the strip. Our results are consistent with a nearly constant friction stress in the sliding zone in agreement with other experimental observations where adhesion and friction are observed.

1 Introduction

Significant efforts have been recently dedicated to develop adhesives inspired by gecko feet. Indeed, these animals rely on "dry" and reversible adhesion based on van der Waals interactions[1]. However this adhesion is not limited to forces normal to surfaces: geckos not only stand on horizontal ceilings, but may also climb along vertical walls. Friction has been shown to play a major role in the amazing sticking properties of geckos or other animal such as tree frogs[2–4].

The design of such biomimetic adhesives tapes has motivated investigations of adhesion in lap-shear configuration (force applied in the direction of the tape) with apparently conflicting approaches. In a recent description, adhesion energy is coupled with the compliance of the system[5–7]. This mechanism leads to the sudden detachment beyond a critical strain. Although this mechanism has been validated experimentally, it challenges the asymptotic limit of a classical model to vanishing peeling angles, where a debonding front progressively propagates as the tape is pulled away[8–11]. However, none of these scenarios involves dissipation through friction. Other studies involving soft adhesive tapes have nevertheless put in evidence a significant effect of friction in a macroscopic region close to the debonding front[12–17]. Other works finally consider the dissipation induced by the propagation of kinetic waves along the interface[18].

In this paper, we wish to study the role of friction in the lap-shear geometry. We are here interested in the pulling of a single strip of silicone rubber adhering on a glass plate through molecular forces. We first clarify in section 2 the differences and apparent contradictions between the main failure mechanisms described in the literature. We present in section 3 our experiments conducted with silicone rubber adhering on a glass plate. We put in evidence the propagation of a friction front as the free end of the strip is pulled away. We propose a simple procedure to estimate the characteristic frictional shear stress acting under the elastomeric strip. We finally discuss this friction stress in the light of other studies involving friction with similar materials.

2 Lap shear geometry: failure mechanisms

We start by presenting two different scenarios from the literature describing the detachment of a strip adhering on a rigid substrate, when the peeling force is parallel to the substrate (lap shear geometry). In this basic configuration (Figure 1), a strip of width w_o adheres to the substrate over a length L_a, and a force F is applied to the free end of the strip of length L in a direction parallel to the plate.

A first classical approach assumes the propagation of a steady peeling front corresponding to a constant force proportional to the width of the strip and independent from the total adhesion area. Conversely, a second approach assumes unstable propagation, where detachment takes place in a single dynamical step. In this scenario, the maximum force before detachment depends explicitly on the total adhesive area Fig. 2. We wish here to clarify the conditions leading to each scenario.

[†] Electronic Supplementary Information (ESI) available: Movie evidencing the progressive deformation of a strip in shear-lap loading. See DOI: 10.1039/C5SM01203A/

PMMH, CNRS UMR 7636, UPMC Université Paris 6, and Université Paris Diderot Paris 7, ESPCI-Paristech, 10 rue Vauquelin - 75005 Paris, France. E-mail: benoit.roman@espci.fr

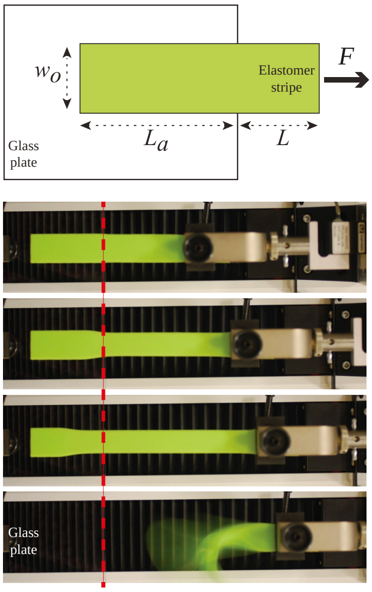

Fig. 1 Top: sketch of the experimental setup in an initial stage, i.e. before any deformation is applied (top view). A long strip of elastomer (in green) of width w_o adheres on a glass plate along a length L_a. The pulling force F at the free end of the strip of length L at a constant speed v is monitored with a force displacement machine
Bottom: snapshots of an actual experiment. The free end is clamped between the moving jaws of the force displacement machine while the glass plate is fixed to the frame. In the last image, the strip has just detached.

2.1 Steady detachment front

In a classical derivation, Kendall[10] considered the steady peeling of an elastic strip of width w_o, thickness h and Young modulus E, adhering on a rigid substrate with an adhesion energy γ (note that γ does not correspond to the thermodynamical adhesion but may depend on the dynamics and on the details of the loading at the debonding front). Friction is not considered in this calculation, *i.e* γ is assumed to be independent of the detachment mode (neglecting *mode mixity* in classical fracture terminology[19]). In a steady regime, the operator applies a constant pulling force $F = Ehw_o\epsilon$, which stretches the strip to a strain ϵ. The elastic energy stored in the strip is then $F^2/2Ehw_o$ per unit length. In the limit of vanishing peeling angle, the operator displaces the free end of the strip by a quantity $\epsilon \mathrm{d}x$ as the delamination front advances by a distance $\mathrm{d}x$ and thus provides a work $\delta W = F\epsilon \mathrm{d}x$. This work is transformed into adhesion energy $\gamma w_o \mathrm{d}x$ but also increases the strechting energy stored in the elastic strip $(F^2/2Ehw_o)\mathrm{d}x$.

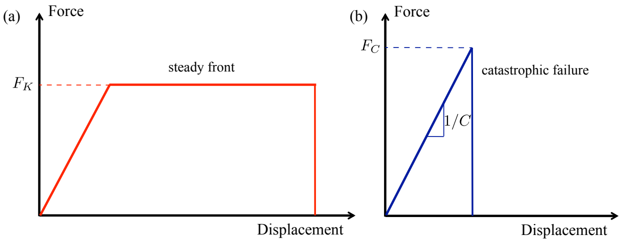

Fig. 2 Complementary scenarios for the failure of an adhesive strip in a lap test configuration. (a) Following the mechanism described by Kendall for a soft strip, a debonding front steadily propagates as the free end of the strip is progressively pulled away (red line). The corresponding plateau force F_K is independent from the length of the strip. (b) In the scenario proposed by Crosby *et al.*, elastic energy is first stored in the system of compliance C and suddenly released as it reaches the critical debonding energy (blue line). The critical load F_C is in this case dependent on the length of the adhering strip.

Energy conservation leads to the steady pulling force:

$$F_K = \sqrt{2Eh\gamma}\, w_o \tag{1}$$

This expression is in agreement with the experiments presented in Kendall's study for angles as low as 10° conducted with ethylene propylene rubber strips adhering on glass through molecular forces[10]. Since the stretching of the strip is important for low peeling angles, standards for testing tapes usually involve large angles of 90° or 180° for which the peeling force is simply proportional to the adhesion energy. As a consequence, studies testing the same lap shear regime with different systems are rather scarce in the traditional literature on adhesion.

2.2 A scenario for catastrophic debonding

Motivated by the design of biomimetic adhesives, Crosby and coworkers developed a different concept based on catastrophic detachment to predict the adhesive force capacity in a general configuration[5,6]. The main argument is that the system of compliance C stores an elastic energy on the order of CF^2 as it is loaded with a force F. This energy is compared with the cost $\gamma_s A$ for debonding an area A. Note that γ_s corresponds to the critical energy release rate under shear (fracture mode mode II). As the the force is progressively increased, the elastic energy eventually reaches the energy required for a total debonding. The situation becomes unstable even if the load is applied through an imposed displacement and the adhesive suddenly detaches beyond the critical load:

$$F_C \sim \sqrt{\gamma_s A/C}. \tag{2}$$

Although neither friction nor the kinetic energy generated by the propagation of the fracture are considered in this approach, this relation is nicely verified on a wide range of experiments involving a compliant elastomer coated with a stiff fabric backing. Interestingly, the failure load obtained in such experiments yields an shear debonding energy γ_s about one order of magnitude greater than the adhesion energy γ obtained in a peeling test at 90 degrees[20].

The scaling relation (2) is a general result for the case of catastrophic debonding. Examples of its application to different geometries involving a backing and a soft adhesive are reviewed by Bartlett *et al.*[6]. We present here as an illustration the case of an adhesive elastomer (of thickness h and width w_o) covered with an inextensible backing in the same geometry as in figure 1. If a load F parallel to the strip is applied, the backing is translated as a rigid body along a distance δ, which induces a uniform shear strain δ/h in the portion of the elastomer adhering to the rigid substrate. The elastic energy stored in the system is therefore $\mu h(\delta/h)^2/2$ per unit of bonded area, where μ is the shear modulus (in the case of an incompressible elastomer, μ is simply one third of the Young modulus, $\mu = E/3$). In a steady state propagation, an advance of a debonding front over a distance $\mathrm{d}x$ will release $\mu h(\delta/h)^2 w_o \mathrm{d}x/2$ of elastic energy, with a cost $\gamma w_o \mathrm{d}x$ of fracture energy. As a consequence, the front will propagate in a single step along the whole extent of the sample if the imposed displacement δ is larger than $\delta_c = \sqrt{2\gamma h/\mu}$. This threshold corresponds to a shear stress on the adhesive $\mu\delta_c/h$ and results into a critical load $F_C = \mu L_a w_o \delta_c/h$. Equation (2) is finally recovered:

$$F_C = \sqrt{2\gamma_s A/C} = A\sqrt{2\mu\gamma_s/h} \tag{3}$$

where $A = wL_a$ is the adhesion area and $C = h/\mu w L_a$ the compliance of the system.

However if we apply directly equation (2) to the first system (strip without backing), we do not recover equation (1). Indeed, the compliance of the system before detachment is given by $C = L/(Ehw)$, where L is the length of the free portion of the strip since the adhering part of the strip first remains undeformed. Equation (2) would thus lead to a different result* $F_C = \sqrt{2Eh\gamma_s}\, w_o \sqrt{L_a/L}$. This is not surprising, since the basic assumptions on the failure mode are different (steady progressive detachment versus a catastrophic single event).

2.3 Reconciling contradictory mechanisms

Which mode of failure occurs in the case of a strip of soft elastomer covered with a rigid backing? Considering the finite stiffness of the backing can reconcile both approaches.

The strain in the strip is uniform in the detached side, and vanishes in the adhered part after a progressive transition of extension ℓ_{lag} (see figure 3). We now estimate ℓ_{lag} as a function of the mechanical properties of the backing tape and the elastic strip (in the absence of backing ℓ_{lag} should be on the order of the thickness of the strip h). We assume that the backing is much stiffer than the elastomer, i.e. $Eh \ll E_b h_b$, where E_b and h_b are the Young modulus and the thickness of the backing material. Within this limit, the elastic strip is mainly submitted to a simple shear, whereas the stiff backing undergoes stretching. A simple force balance on a short portion of the strip leads to

$$\frac{E}{3h}u + E_b h_b \frac{\partial^2 u}{\partial x^2} = 0,$$

where $u(x)$ is the local displacement of the tape at position x. As described by Kaelble[9], the integration of this equation leads to an exponential decay of the strain of the strip over a distance:

$$\ell_{lag} \sim h\sqrt{\frac{E_b h_b}{Eh}}. \tag{4}$$

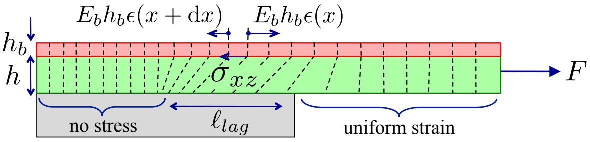

Fig. 3 Case of a strip coated with a backing of finite rigidity. The coupling between the tensile strain in the backing and the shear in the soft adhering strip results into the decay of the local strain along a length scale ℓ_{lag}.

Comparing L_a with ℓ_{lag} indicates which debonding mechanism we should expect. If $\ell_{lag} \gg L_a$, the whole adhesive layer is under uniform shear. We recover a situation similar to the case of inextensible backing and the strip should suddenly detach beyond the critical load F_C.

Conversely, in the case $\ell_{lag} \ll L_a$, a small fraction of the strip adhering on the substrate is subject to the applied load. The remaining of the strip remains at rest in agreement with Kendall's steady scenario, leading to a steady load F_K (Eq. 1). This would for instance be the case in the absence of a backing layer, where $\ell_{lag} \sim h$.

As a conclusion, the mode of failure is selected by the length of the adhered zone L_a compared to the shear elastic decay length ℓ_{lag}. Longer adhered areas will eventually reach Kendall's plateau (eq.1), whereas shorter ones (or very stiff backing) will follow a catastrophic scenario (eq. 2).

However, although friction obviously prevents the tape from sliding, none of these mechanisms accounts for a possible energy dissipation through friction. The effects of friction

---

* We note however that in many cases L and L_a are of the same order of magnitude so that the scaling relation (2) applies again.

in peeling configurations have nevertheless been evidenced and described at both local [12–14] and global scales [15–17].

In the following section, we present experiments with a strip made with a single material where friction plays a major role. Curiously, we observe a propagating front reminiscent from Kendall's mechanism but the force leading to the detachment of the strip is proportional to the initial adhesion area, as in the catastrophic scenario.

3 Experiments with silicone rubber adhering on glass

3.1 Experimental methods

Our experiments were performed on smooth glass plates carefully cleaned with ethanol. The strips made in PolyVinylSiloxane (Elite Double 16, 22 and 32 from Zhermack) were prepared by mixing equal quantities of "base" and "catalist" liquids. The strips were elaborated with an initial length of 250 mm, a width w_o ranging from 7.5 to 60 mm, and a thickness h of 1 or 2 mm. The Young modulus could be selected between 400 and 1200 kPa. Accidental dust particles were removed with standard adhesive tape. The strips spontaneously adhere on glass through intermolecular interactions.

The adhesion energy was measured for each sample through a standard 90° peeling test [21] carried at a velocity of 0.5 mm/s with an Instron 5865 force-displacement machine. Depending on the polymer selected, γ could vary between 0.5 and 1.5 N/m. Following the procedure described by Crosby *et al.*, we finally performed some experiments with strips covered with a stiff backing, in which case the debonding is catastrophic. We obtained a shear debonding energy γ_s ranging from 1.4 to 5.4 N/m (the experimental procedure is described in section 3.6.2).

Before starting a lap-test experiment, a length of the strip L_a is deposited on the glass plate. After a waiting time on the order of 5 min, the extremity of the free portion of the strip was clamped between the jaws of the force displacement machine and was pulled at a constant velocity v ranging from 10 to 50 mm/min, while the glass plate is held at a fixed position (see figure 1). The alignment with the glass plate was verified with a laser sheet projected on the strip with a low incidence. A finite peeling angle would result into a deflection of the projected line. This setup ensured that the peeling angle was less than $0.7°$. Moreover, supplementary experiments conducted at low but finite peeling angles did not change significantly the results. The pulling force $F(t)$ and the displacement of the free end $\delta(t)$ are simultaneously monitored. For a given set of experiments, the compliance of the non-adhering portion of the strip was maintained constant. This means the initial length had a fixed value of $L = 40$ mm in most of our experiments, so in order to vary L_a, we vary the total length of the strip.

3.2 Peeling force.

Following the previous works described in section 2, we would expect to obtain a constant plateau for the peeling force since the strip is not covered with any backing ($L_a \gg \ell_{lag} \sim h$). However, our experimental results are in contradiction with this scenario. We indeed observe a continuous increase of the force as the free end is pulled away until the strip detaches (Fig. 4). In addition, the critical force for detachment increases with the adhered area (here with the the length L_a), and its value (up to 40 N) is much higher than the critical force predicted by Kendall $F_K = 1.5$ N for $\gamma \approx 1$ J/m^2 in equation (1). Note finally that prior to detachment, the force sometimes displays jumps as it is commonly observed in systems displaying stick-slip behaviors.

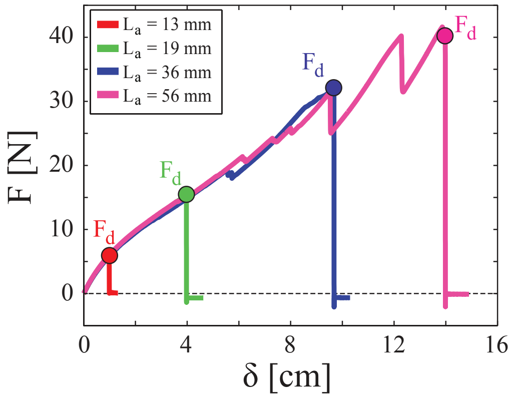

Fig. 4 Tensile force applied to the strip as a function of the imposed displacement. The material parameters for the strip are $E = 529\,(\pm 2)$ kPa, L = 49 mm, w_o = 30 mm, h = 2.3 mm. The detachment force is marked for each experience with a point of the same color of the corresponding adhering length.

At first glance, the evolution of the force is reminiscent of the mechanism described by Crosby and coworkers [5]. However, an estimate of the corresponding force as predicted from Eq.(2) leads to $F_C \approx 2\,$N, for an area $A = w_o L_a = 10^{-3}\,$m^2, a debonding energy of $\gamma_s \approx 5\,$J/m^2 and compliance $1/C \approx$ 300 N/m directly inferred from Fig. 4. This estimate is more than one order of magnitude lower than the detachment force actually measured ($F_d \sim 40\,$N), which would require an unrealistic value of $\gamma_s \sim$ 2kJ/m^2.

To gain further insight, we performed similar experiments with strips of different geometries and elastic rigidities. We represent in Fig. 5 the maximum load obtained for these experiments as a function of the initially adhering area. Both quantities are fairly proportional, independently from the width and the thickness of the strip or even from the Young modulus of the elastomer. Our data suggest that the detachment force obeys

$$F_d = \tau_{\text{eff}} w_o L_a = \tau_{\text{eff}} A, \tag{5}$$

where the prefactor τ_{eff} has the dimension of a stress and is on the order of 20-30 kPa in our system.

Nevertheless, monitoring the total force only provides a very limited analysis. In the following section we describe the local strain distribution in the strip through a simple imaging technique, and describe the propagation of a sliding front.

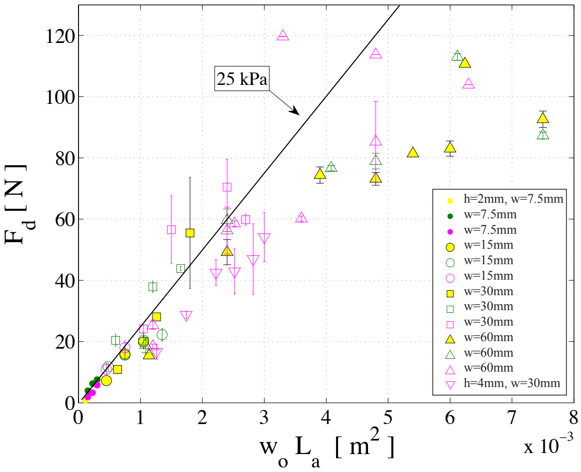

Fig. 5 Force at the detachment of the strip as a function of the initially adhering area, • for $w_o = 7.5$ mm, ∘ for $w_o = 15$ mm, □ for $w_o = 30$ mm, △ for $w_o = 60$ mm. The color code corresponds to the Young's modulus: $E_{magenta} = 520(\pm 50)$ kPa, $E_{yellow} = 730(\pm 160)$ kPa and $E_{green} = 1130(\pm 160)$ kPa (the variability in E is relative to different specimens).

3.3 Local friction

3.3.1 Front propagation. We present in Fig. 6 successive snapshots of a strip captured during an experiment (see also movie in Electronic Supplementary Information). When the strip is stretched, its width decreases as a consequence of the incompressibility of the elastomer (the Poisson coefficient is close to 0.5 for such materials).

Three different zones are clearly identified by following the local width w of the strip, see fig. 6 bottom. In zone 1, the strip adheres to the glass plate and does not experience any stress. Zone 3 is the part of the strip that is away from the plate. The width w_∞ is uniform in this zone, indicating a constant extension stress along the strip ($w_\infty < w_0$). Zone 2 corresponds to a transition between zones 1 and 3. The width $w(x)$ varies gradually along this region from w_o to w_∞. This evolution indicates that the tension in the strip progressively decays from zone 3 to zone 1.

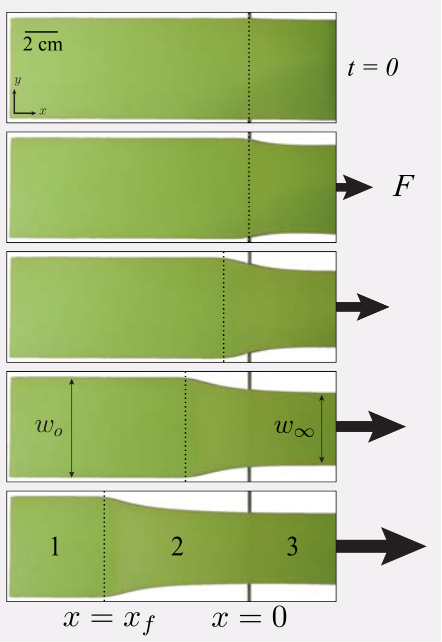

Fig. 6 Experimental snapshots of the strip during successive instants of an experiment (a movie of the experiment is available as Electronic Supplementary Information). A transition region 2 can be clearly identified between region 1, where the strip is at rest and region 3 where the strip is away from the glass plate and uniformly stretched. The deformation front which is separating regions 1 and 2 advances towards region 1 as the strip is continuously pulled away. Here, $w_o = 60$ mm.

A sliding front delimits zones 1 and 2. This front of position x_F propagates towards zone 1 as the end of the strip is continuously pulled away. The strip eventually detaches when this front gets close to its end, and the whole strip coils back.

3.3.2 Friction stress along the strip. As the deformation front propagates, we observe that in zone 2 the strip remains in contact with the glass plate, sliding over it, which indicates that the adhering material is subject to friction. We propose in this section to estimate directly the shear stress acting on the strip by measuring its lateral deformation.

Due to the symmetry of the deformation profile and the horizotal direction of the pulling force, the global force $F(x)$ acting on a transverse slice of the material is also horizontal and directed along the x axis. Zone 1 of the strip is free from any stress, while zone 3 is under uniform axial stress, $\sigma_{xx} = F_\infty / w_o h$. In zone 2, $F(x)$ varies from 0 to F_∞ and we assume that the strip is submitted to a shear stress as a result of frictional sliding. We refer to $\tau(x)$ as the value of this shear stress averaged over the local width $w(x)$. If we neglect stresses and strains in the y direction, a simple force balance connects τ to the evolution of the global force $F(x)$ acting on a slice of the strip:

$$\frac{\partial F}{\partial x} = w(x)\,\tau(x). \tag{6}$$

In order to estimate the local force $F(x)$, we extract the corresponding local width $w(x)$ from image processing, and compare it with a calibration curve determined through a standard force *vs.* displacement test implemented with a synchronized imaging of the strip. In this approach, we assume the relation between $F(x)$ and $w(x)$ to be locally the same as in a uniform tensile test although the strain varies spatially. Neglecting two dimensional effects is in principle valid for slowly varying loads, an assumption which can be questioned in our experiments, especially in the vicinity of the sliding front. The elastomer follows a Hookean behavior for moderate strains up to $\epsilon_w = (w - w_o)/w_o \sim 0.2$ and hardens for higher strains (Fig. 7). We used a 5^{th} order polynomial fit to account for this non-linear behavior. By simply following the evolution of $w(x)$ we thus infer the local tension $F(x)$, and using eq.(6) the shear stress $\tau(x)$ acting on the strip is computed.

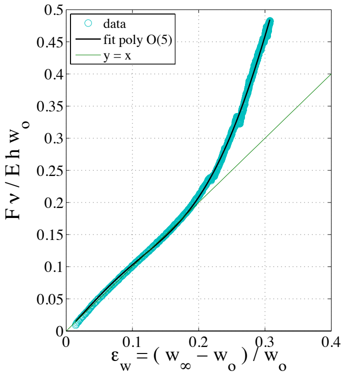

Fig. 7 Calibration curve of the force as a function of the width of the strip. The initial linear dependence provides the Young modulus of the material (in the current case, 1 MPa). The black solid curve corresponds to a 5^{th} order polynomial fit and the green solid line is the reference of a linear curve with unit slope.

Figure 8 represents, at a given time, the spatial dependence of the width of the strip, the local force deduced from the calibration and the frictional shear stress estimated from eq. 6. As expected, $\tau(x)$ starts from zero in zone 3, increases in zone 2 and eventually vanishes again in zone 1[†].

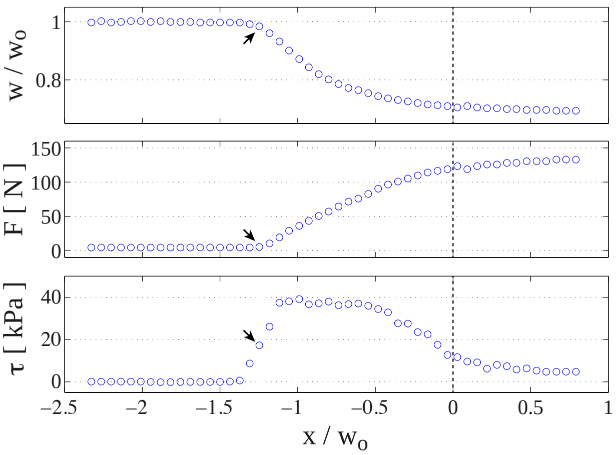

Fig. 8 Measurement of the local width and estimation of the corresponding force and shear stress acting on the strip at a given time (the applied dispalcement corresponds to $d/w_o = 2.33$ in fig.9). In the x coordinate, zero corresponds to the edge of the glass plate, while positive coordinates represent the side of the strip that is away from the plate, i.e. zone 3. The arrows indicate the position of the sliding front x_F. This front is defined as the location where local width has decreased by 1% from its initial value. Experimental parameters are: $E = 1055\,\text{kPa}$, $h = 2.2\,\text{mm}$ and $w_o = 60\,\text{mm}$.

Interestingly, the shear stress reaches a constant value on the order of 40 kPa. The same procedure can be repeated at successive moments of the experiment. The global evolution of the stress distribution $\tau(x)$ is best visualised using a space-stress diagram (Fig. 9). The imposed displacement is measured directly by the traction machine and is proportional to time, since the displacement speed is imposed to 0.5 mm/s in the presented experiments. This particular experiment has been conducted with $E = 1055\,\text{Pa}$, $L_a = 140\,\text{mm}$, $w_o = 60\,\text{mm}$, $h = 2.2\,\text{mm}$. Nevertheless, similar qualitative features were obtained with other specimens. In particular, we found a plateau shear stress in the range 20 to 40 kPa for all the strips.

Recent works have been specifically dedicated to the friction between soft polydimethyl siloxane (PDMS) and rigid materials (glass with different molecular coatings). In these experiments, a spherical cap made of PDMS is slid over a glass plate[22,23]. Conversely, a glass spherical cap can also be put in contact with a flat substrate of PDMS with a fixed normal load and submitted to a given torsional stress[24–28]. Peeling configurations closer to the present study have also been explored through the the tracking of markers embedded in the tape[13,14]. As a salient result, sliding involves a constant frictional shear stress independent of pressure in the case of smooth contact, in contrast with the common Ammonton-

---

[†] Note that our technique leads to a non-zero value of $\tau(x)$ in zone 3 in the vicinity of the edge of the glass plate. We interpret this artefact as a consequence of strains in the y direction that we have neglected.

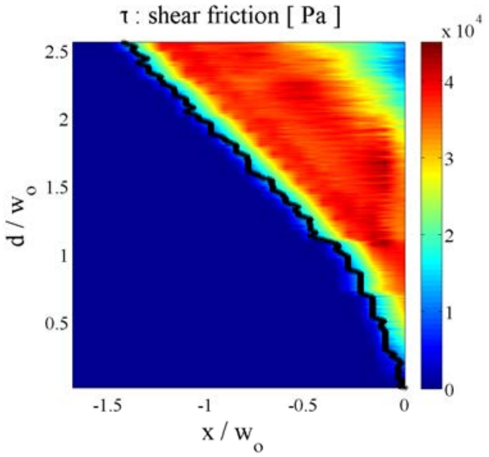

Fig. 9 Space-displacement diagram representing the estimated shear stress acting on the strip as its free end is pulled at a constant velocity. Experimantal parameters: $E = 1055\,\mathrm{kPa}$, h = 2.2 mm and $w_o = 60\,\mathrm{mm}$. The sliding front represented by the black line progressively propagates through the strip. Data in fig. 8 correspond to $d/w_0 \sim 2.33$ in the space-displacement diagram.

Coulomb law. Friction stresses were found to depend significantly on the chemical treatment of the interface and, to a lower extent, on the sliding velocity. Nevertheless their values all range between 10 and 500 kPa. Although the chemical nature of the PolyVinylSiloxane rubber used in our experiments is slightly different from PDMS, our data are compatible with previous studies.

In order to test the possible influence of the chemical nature of the substrate, we conducted two additional series of experiments with glass plates grafted with trichloro-perfluorooctylsilane and with adsorbed polydimethylsiloxane molecules (PDMS, viscosity of 200 cSt). Both treatments are indeed commonly used to modify surface energies and are described in detail by Mettu and Chaudhury[29]. Lap-test experiments exhibited the same qualitative behavior as in the case of a clean glass plate. The different values for the adhesion energy γ, the shear debonding energy γ_s and the friction stress τ obtained with the same polymer ($E = 1300\,\mathrm{kPa}$) and with the same pulling velocity ($0.5\,\mathrm{m/s}$) are reported in table 1. As a general trend, both treatments decrease significantly adhesion energies and more moderately the friction stress. Stronger effects are obtained with the plate coated with PDMS. A deeper interpretation of this comparison is however beyond the scope of the present work.

surface	γ [N/m]	γ_s [N/m]	τ [kPa]
plain glass	0.8 ± 0.1	5.3 ± 0.5	65 ± 5
perfluorosilane	0.54 ± 0.08	4.7 ± 0.5	48 ± 2
PDMS	0.36 ± 0.04	2.6 ± 0.5	39 ± 4

Table 1 Adhesions energies and friction stresses obtained with the same polymer ($E = 1300\,\mathrm{kPa}$) on different substrates. Clean glass is compared with glass grafted with trichloroperfluorooctilsilane and with adsorbed polydimethylsiloxane molecules (PDMS, viscosity of 200 cSt).

3.4 From local friction to the global peeling force

The integration of the local friction stress described in the previous paragraph provides the global pulling force, $F = \int_0^{x_F} \tau(x) w(x) \mathrm{d}x$. In the previous section, the friction stress was found to quickly reach a plateau value as the sliding front progresses. Multiplying this plateau value by the contact area should thus provide a good estimate for the force. As a fist order approximation, the contact area is equal to $x_F w_o$ with an error below 20%, leading to a pulling force proportional to the displacement of the sliding front. This linear variation is approximately observed in our experiments and corresponds to an average friction stress of 30 kPa (Fig. 10a). The detachment force follows the same evolution, which indicates that the band detaches when the front reaches its extremity (Fig. 10b). In practice, the strip actually detaches before the front reaches the free end of the strip, probably because this front is not perfectly straight.

However, the detail of the evolution of the pulling force with the position is in reality more subtle than a linear relation relying on a fixed value of the friction stress. We indeed observe a threshold of the force below which the front does not move. Stick-slip motion of the front is also observed for high strains. In this case the force tends to saturate, especialy for wide strips. We describe both effects in the following section.

3.5 Before and beyond steady sliding

3.5.1 Sliding threshold. In our experiments, the sliding front is only observed to move beyond a critical pulling force F_{th}, in Fig. 10a. The critical force is approximately proportional to w_o, which corresponds to a critical tension F_{th}/w_o on the order of 330 N/m (Fig. 11a). This threshold is not included in our description involving a sliding front. In this model, the strip is indeed expected to start sliding for any finite pulling load.

This critical tension could be intuitively compared with the law predicted by Kendall (eq. 1), where the peeling front is

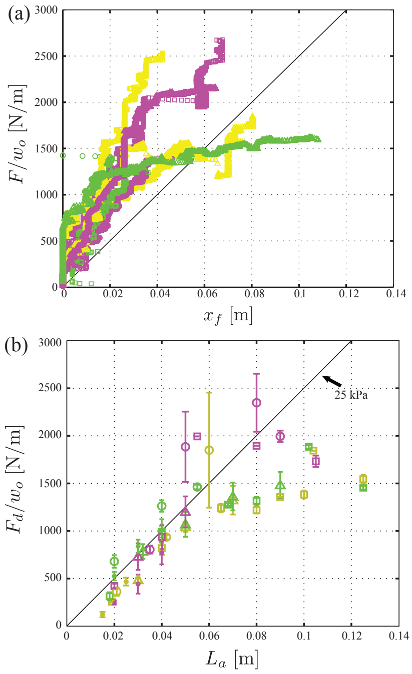

Fig. 10 (a) Instantaneous applied force normalized by the initial strip width as a function of the detachment front position. (b) Final detachment force normalized by the strip width as a function of the initially adhered length. The legend for both figures is the same as in figure 5, except curves for $w_o = 7.5$ mm are not presented. The solid black line represents a stress of 25 kPa.

also expect to move beyond a critical load. However, the numerical estimates of $\sqrt{2Eh\gamma}$ lay within the range 30 to 50 N/m for our configuration, which is low in comparison with the tension F_{th}/w_o we measure in our experiments. Using the shear debonding energy γ_s may be more relevant than the adhesion energy γ. Nevertheless, it would increase the estimate to a maximum value of 100 N/m, which remains too low compared to the expected 330 N/m.

Another candidate for the threshold would be the product $\tau\ell$ of the friction stress with a length scale ℓ. In our simplified approach, the detail of the shear across the thickness of the strip was indeed not considered. However, we expect the strain distribution to evolve from a uniform axial strain to a uniform shear in the vicinity of the edge of the plate. Due to the Laplacian nature of elasticity equations, the length scale involved is set by the thickness of the strip h. Nevertheless, the product τh is on the order of 50 N/m. This value also appears too low, even if a numerical prefactor might increase the actual effective length scale.

Two-dimensional effects were finally neglected in our simplified approach. However, the sides of the strip tend to slide toward the center line as the strip is stretched. In more pronounced situations this lateral displacement leads to the evolution of the peeling front into a V shape[18]. The coupling of the shear in both directions may also explain the premature detachment of the strip before the friction front reaches L_a. The consequence of such 2D effects would lead to a length scale ℓ proportional to w_o. Numerically the product τw_o varies in the range 300 to 1800 N/m in our experiments, which now tends to be too high. Besides we would then expect a quadratic variation of the critical force with the width, which contradicts our observation (although the actual data is scattered).
To conclude, although the detail of the critical force remains an open question, its value should rely on a combination between the detail of shear strain and 2D effects.

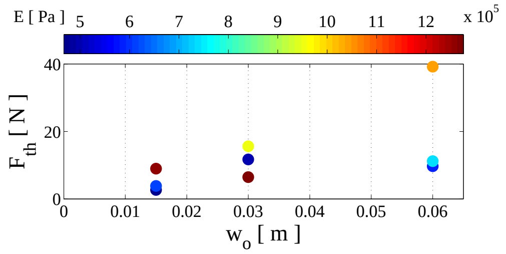

(a) Threshold force

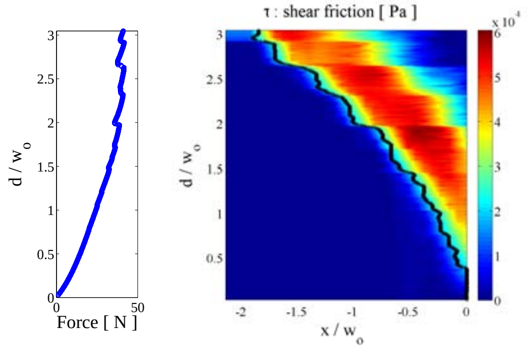

(b) Tensile force (c) Shear Stress

Fig. 11 (a) Threshold force as a function of the width of the strip. The colorbar represents the Young modulus of each sample in units of Pa. (b) Evolution of the tensile force as a function of the imposed displacement in an experiment displaying stick slip behavior (upwards). (c) Space-stress diagram quantifying the corresponding shear stress on a strip, the black line represents the sliding front position. Sample's parameters for diadrams (b) and (c): $E = 1055$ kPa, h = 2.2 mm and $w_o = 30$ mm.

3.5.2 Stick slip. We represent in fig. 11 b & c, a force-displacement curve and the corresponding space-stress diagram where jumps are clearly evidenced. Interestingly, the whole sliding zone is globally shifted for major jumps. This shift leads to the development of a secondary front in the rear part of the strip remaining in apparent contact with the rigid plate. The shear stress significantly decreases and almost vanishes in this region. As a consequence, the force tends to saturate as observed in Fig. 10 for high pulling forces. The observed stick-slip behavior, also noticed by Lake and Stevenson[18] in a peeling configuration, is reminiscent of Schallamach waves[30,31]. Qualitatively, stick-slip appears for high strains and is very sensitive to minute air bubbles trapped between the strip and the plate. A quantitative description of the phenomenon is beyond the scope of the current study. Understanding stick-slip is nevertheless crucial for practical applications since it may lead to a premature detachment of the band.

3.6 Comparison with other experiments.

3.6.1 Towards adhesion rheology?Although the experimental procedure is very close to the study by Kendall[10], the results are significantly different. Both situations indeed involve the propagation of a front, but the case of Kendall does not include friction, which leads to a steady peeling force even in the limit of a vanishing peeling angle. Conversely, the propagation of a sliding front results into an increasing force in our experiments. If the specimens are long enough, the detachment force is orders of magnitude higher than the prediction by Kendall. Recent experiments conducted with strips of polydimethylsiloxane adhering on glass also involve important frictional dissipation at low peeling angles[15]. Similar large effects of friction for low angles are also observed in our system[32]. However, the reason why frictional dissipation plays a role in some cases and can be neglected in others remains an open question.

The answer probably relies on the different nature of the polymers used in the experiments. Kendall's experiments were performed with vulcanized ethylene propylene rubber while we used Poly Vinyl Siloxane rubber. Although macroscopic Young moduli and adhesion energies (corresponding to debonding) are comparable, the dynamics of adhesion may be totally different. Indeed Kendall's procedure required a contact time of 1h before running a test. The adhesion of PVS on glass seems much faster and our experiments were performed within a few minutes after depositing the polymer on the glass plate. Although the detail of the bonding / debonding dynamics is beyond the scope of the present study, our observations suggest that the "bonding" time plays a crucial role in friction[33]. If the adhesion dynamics are slow in comparison with the velocity of the imposed displacement, the elastomer may not re-adhere behind the front, which would lead to scenario described by Kendall. Conversely, fast re-adhesion would lead to the important friction we observe in our experiments. Capturing all the ingredients involved in the coupling between friction and adhesion will require additional significant efforts. Nevertheless we hope that our study will motivate further studies in the field.

3.6.2 From catastrophic debonding to friction We described in section 2.3 the theoretical transition between steady peeling to catastrophic debonding in the case of a strip coated with a stiffer backing. This transition is related to the finite stiffness of the backing, which results into shear-lag and a corresponding length scale ℓ_{lag} (Eq. 4). The comparison of ℓ_{lag} with the length of the adhered strip L_a determines which scenario is expected.

In order to estimate numerical values of the debonding energy γ_s, we conducted a series of experiments with two different strips covered with a stiffer backing. These strips were covered with a thin mesh of nylon before curing. The imbibition of the mesh assures its firm ancoring to the strip. The effective stiffness $E_b h_b + Eh$ was measured with a standard traction test and it is of the order of $E_b h_b$ compared to the stiffness Eh of a plain strip of the same thickness. We verified the condition for shear-lag $Eh \ll E_b h_b$. With strips of thickness $h = 2\,\mathrm{mm}$, we obtained $\ell_{lag} \simeq 20\,\mathrm{mm}$ and $30\,\mathrm{mm}$ for elastomers of $E = 1300$ and 225 kPa, respectively.

We followed the lap-shear procedure described by Crosby and collaborators. Force *vs.* displacement tests were carried on strips adhering over an area $A = L_a w_o$. We measured the critical pulling force F_C and deduced the compliance of the system from the slope of the corresponding curve (see sketch in Fig. 2a). We represent in figure 12 the critical load F_C as a function of $\sqrt{A/C}$. We obtain the expected linear dependence between both quantities for short lengths of adhesion (linear fits in the figure, which provide estimates of the debonding energy γ_s). However, we observe a clear transition to a different regime for long strips. In this second regime the maximum load increases in a dramatic manner with a value compatible with friction stresses measured independently with plain strips. Interestingly, we find that the transition occurs for $L_a \simeq 2\ell_{lag}$. The description in terms of shear lag is thus also relevant to describe the transition from the regime of catastrophic debonding reported by Crobsy *et al.* to a regime dominated by friction, which is the focus of the present study.

4 Conclusion

To summarize, the comparison of our experimental results with other studies from the literature put in evidence three different failure modes for a tape adhering on a rigid substrate though molecular interactions.

A first mode involves the coupling between a compliant adhesive and a stiff backing. In this configuration, the whole tape reacts to the load and suddenly detaches if the pulling force exceeds a critical value. This maximum load is proportional to

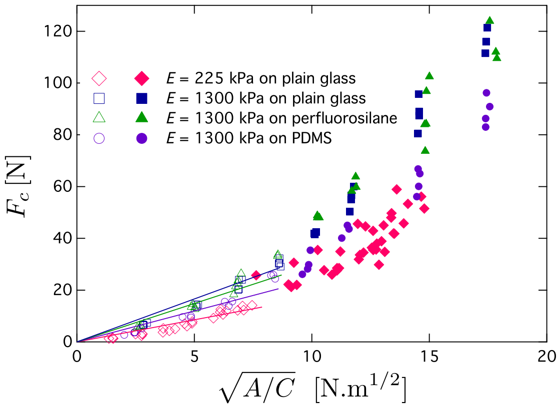

Fig. 12 Experiments with a backing. Critical load F_C as a function of $\sqrt{A/C}$. We observe a transition from catastrophic debonding to the regime dominated by friction as L_a is progressively increased: open symbols $L_a < 2\ell_{lag}$, filled symbols $L_a > 2\ell_{lag}$. In the first regime, F_C is nearly proportional to $\sqrt{A/C}$. The slope of the corresponding linear fits provides an estimate of the shear debonding energy γ_s from Eq. 2.

the area of adhesion and to a characteristic stress accounting for both adhesion energy and compliance of the system.

A second mode corresponds to tapes consisting in a single compliant strip with slow adhesion dynamics (and consequently low friction). In this case, the peeling force is steady during the peeling process and exhibits a plateau value as the peeling angle vanishes. This force is proportional to the width of the strip and to a tension accounting for the adhesion energy and the material stretching modulus. A comparison of the shear lag distance ℓ_{lag} to the length of the strip discriminates between this progressive front propagation and the catastrophic debonding.

Our experiments involve a third scenario where friction plays a crucial role in the peeling process. A sliding front propagates along the adhering part of the strip beyond a threshold, as the other end is progressively pulled away. We developed a simple technique based on monitoring the deformation of the strip to estimate the corresponding friction stress. As a crude approximation, the shear stress is uniform and steady in the zone of friction. The global friction force thus increases linearly with the advance of the sliding front. The strip suddenly detaches when the front eventually reaches its end. The order of magnitude of friction stress estimated for the polyvinylsiloxane elastomers used in our experiences, $\tau \sim 30$ kPa, is in agreement with measurements from the literature conducted with other silicone rubbers. In the presence of backing, the criterion based on shear-lag is also relevant to describe the transition from catastrophic debonding to a regime dominated by friction. Although commercial adhesive tapes display more complex behaviors due to the rheology of the adhesive layer[34] or of the plasticity of the backing, the current study should be relevant for designing future soft adhesives.

These observations on the role of friction in shear debonding could be interpreted as *mode mixity* within the traditional frame of fracture mechanics. However, we believe that this terminology might be misleading in our case. Here friction takes place on a very large scale (the whole specimen) and the underlying assumption of a very small process zone where mode mixity take place is not valid.

Several fundamental questions remain open. The origin of the threshold force remains unclear and should be probed systematically in other configurations. In particular, the implication of friction in the propagation of the front remains to be elucidated. This selection may involve dynamics of the adhesion process at a molecular scale or, more macroscopically at the scale of the roughness of the materials. To investigate this last effect, it would be interesting to carry experiments on surfaces with patterned geometries such as pillars[27] or wrinkles[35]. Finally our study focuses on the particular lap test configuration. To address most practical applications, it would be interesting to generalize this work to finite peeling angles.

Acknowledgements

We are grateful to Miguel Trejo, Manoj Chaudhury, Alfred Crosby, Frédéric Restagno, Christophe Poulard, Chung-Yuen Hui for stimulating discussions on friction of soft polymers. This research has been partially funded by the Interuniversity Attraction Poles Programme (IAP 7/38 MicroMAST) initiated by the Belgian Science Policy Office. S. P. thanks the *Becas Chile* program.

References

1 K. Autumn, M. Sitti, Y. Liang, A. Peattie, W. Hansen, S. Sponberg, T. Kenny, R. Fearing, J. Israelachvili and R. Full, *Proceedings of the National Academy of Sciences*, 2002, **99**, 12252–12256.
2 K. Autumn, A. Dittmore, D. Santos, M. Spenko and M. Cutkosky, *Journal of Experimental Biology*, 2006, **209**, 3569–3579.
3 N. Gravish, M. Wilkinson and K. Autumn, *Journal of The Royal Society Interface*, 2008, **5**, 339–348.
4 T. Endlein, A. Ji, D. Samuel, N. Yao, Z. Wang, W. Barnes, W. Federle, M. Kappl and Z. Dai, *Journal of The Royal Society Interface*, 2013, **10**,.
5 M. Bartlett, A. Croll, D. King, B. Paret, D. Irschick and A. Crosby, *Advanced Materials*, 2012, **24**, 1078–1083.
6 M. Bartlett, A. Croll and A. Crosby, *Advanced Functional Materials*, 2012, **22**, 4985–4992.
7 J. Risan, A. Croll and F. Azarmi, *Journal of Polymer Science Part B: Polymer Physics*, 2015, **53**, 48–57.
8 D. Kaelble, *Trans. Soc. Rheology*, 1959, **III**, 161–180.
9 D. Kaelble, *Trans. Soc. Rheology*, 1960, **IV**, 45–73.
10 K. Kendall, *Journal of Physics D: Applied Physics*, 1975, **8**, 1449–1452.
11 K. Kendall, *Journal of Physics D: Applied Physics*, 1975, **8**, 512–522.
12 B. Newby and M. Chaudhury, *Langmuir*, 1997, **13**, 1805–1809.

13 B. Newby and M. K. Chaudhury, *Langmuir*, 1998, **14**, 4865–4872.

14 N. Amouroux, J. Petit and L. Léger, *Langmuir*, 2001, **17**, 6510–6517.

15 R. Collino, N. Philips, M. Rossol, R. McMeeking and M. Begley, *J. R. Soc. Interface*, 2014, **11**, 20140453.

16 A. Jagota and C. Hui, *Materials Science and Engineering: R: Reports*, 2011, **72**, 253 – 292.

17 M. Begley, R. Collino, J. Israelachvili and R. McMeeking, *Journal of the Mechanics and Physics of Solids*, 2013, **61**, 1265 – 1279.

18 G. Lake and A. Stevenson, *J. Adhesion*, 1981, **12**, 13–22.

19 J. Hutchinson and Z. Suo, *Adv. Appl. Mech.*, 1992, **29**, 64–191.

20 D. King, M. Bartlett, A. Crosby, C. A. Gilman and D. Irschick, *Adv. Mater.*, 2014, **26**, 4345–4351.

21 A. Gent and S. Kaang, *J. Adhesion*, 1987, **24**, 173–181.

22 H. Brown, *Science*, 1994, **263**, 1411–1413.

23 L. Bureau and L. Léger, *Langmuir*, 2004, **20**, 4523–4529.

24 A. Chateauminois and C. Fretigny, *Eur. Phys. J. E*, 2008, **27**, 221–227.

25 A. Chateauminois, C. Fretigny and L. Olanier, *Phys. Rev. E*, 2010, **81**, 026106.

26 D. Nguyen, *PhD thesis*, Université Pierre et Marie Curie, 2012.

27 E. Degrandi-Contraires, C. Poulard, F. Restagno and L. Leger, *Faraday Discuss.*, 2012, **156**, 255–265.

28 M. Trejo, C. Fretigny and A. Chateauminois, *Phys. Rev. E*, 2013, **88**, 052401.

29 S. Mettu and M. Chaudhury, *Langmuir*, 2011, **27**, 10327–10333.

30 M. Barquins, *Materials Science and Engineering*, 1985, **73**, 45 – 63.

31 C. Rand and J. Crosby, *Appl. Phys. Lett.*, 2006, **89**, 261907.

32 S.Ponce, B.Roman, J.Bico and C.-Y. Hui, *in preparation*, 2015.

33 A. Filippov, J. Klafter and M. Urbakh, *Phys. Rev. Lett.*, 2004, **92**, 135503.

34 R. Villey, C. Creton, P.-P. Cortet, M.-J. Dalbe, T. Jet, B. Saintyves, S. Santucci, L. Vanel, D. Yarusso and M. Ciccotti, *Soft Matter*, 2015, **11**, 3480–3491.

35 C. Rand and A. Crosby, *J. Appl. Phys.*, 2008, **106**, 064913.

Bibliography

[1] C. Py, P. Reverdy, L. Doppler, J. Bico, B. Roman, and C. N. Baroud, “Capillary origami: Spontaneous wrapping of a droplet with an elastic sheet,” *Physical Review Letters*, vol. 98, p. 156103, Apr 2007.

[2] M. Piñeirua, J. Bico, and B. Roman, “Capillary origami controlled by an electric field,” *Soft Matter*, vol. 6, p. 4491, Jan 2010.

[3] J. Hure, B. Roman, and J. Bico, “Wrapping an adhesive sphere with an elastic sheet,” *Physical Review Letters*, vol. 106, p. 174301, Apr 2011.

[4] E. Hamm, P. Reis, M. Leblanc, B. Roman, and E. Cerda, “Tearing as a test for mechanical characterization of thin adhesive films,” *Nature Materials*, vol. 7, pp. 386–390, May 2008.

[5] D. Vella, J. Bico, A. Boudaoud, B. Roman, and P. M. Reis, “From the cover: The macroscopic delamination of thin films from elastic substrates,” *Proceedings of the National Academy of Sciences*, vol. 106, p. 10901, Jun 2009.

[6] K. Autumn, Y. A. Liang, S. T. Hsieh, W. Zesch, W. P. Chan, T. W. Kenny, R. Fearing, and R. J. Full, “Adhesive force of a single gecko foot-hair,” *Nature*, vol. 405, pp. 681–684, Jun 2000.

[7] K. Kendall, “The adhesion and surface energy of elastic solids,” *J. Phys. D : Appl. Phys.*, vol. 4, pp. 1186–1195, 1971.

[8] K. Kendall, “Thin-film peeling-the elastic term,” *Journal of Physics D: Applied Physics*, vol. 8, p. 1449, 1975.

[9] B. min Zhang Newby, M. K. Chaudhury, and H. R. Brown, “Macroscopic evidence of the effect of interfacial slippage on adhesion,” *Science, New Series*, vol. 269, pp. 1407–109, Apr 1995.

[10] B. min Zhang Newby and M. K. Chaudhury, “Friction in adhesion,” *Langmuir*, vol. 14, pp. 4865–4872, Oct 1998.

[11] N. Amouroux, J. Petit, and L. Leger, “Role of interfacial resistance to shear stress on adhesive peel strength,” *Langmuir*, vol. 17, pp. 6510–6517, Jan 2001.

[12] B. Audoly and Y. Pomeau, *Elasticity and Geometry: From hair curls to the non-linear response of shells*. Oxford University Press, 1st ed., 2010.

[13] L. D. Landau, L. P. Pitaevskii, E. M. Lifshitz, and A. M. Kosevich, *Theory of Elasticity*. Butterworth-Heinemann, 3rd ed., 1986.

[14] F. London, “The general theory of molecular forces,” *Trans. Faraday Soc.*, vol. 33, pp. 8b–26, 1937.

[15] A. W. Adamson, A. P. Gast, *et al.*, *Physical chemistry of surfaces*. Interscience publishers New York, 1967.

[16] A. Stone, *The theory of intermolecular forces*. Oxford University Press, 2013.

[17] J. N. Israelachvili, *Intermolecular and surface forces: revised third edition*. Academic press, 2011.

[18] G. Petitet and M. Barquins, *Matérieux Caoutchouteux*. Presses Polytechniques et universitaires romandes, 1st ed., 2008.

[19] A. A. Griffith, "The phenomenon of rupture and flow in solids," *Philosofical Transactions of the Royal Society of London. Series A*, vol. 221, pp. 163–198, Apr 1921.

[20] K. L. Johnson, K. Kendall, and A. D. Roberts, "Surface energy and the contact of elastic solids," *Proceedings of the Royal Society of London. Series A, Mathematical and Physical Sciences*, vol. 324, pp. 301–313, Jan 1971.

[21] D. Maugis and M. Barquins, "Fracture mechanics and adherence of viscoelastic solids," in *Adhesion and adsorption of polymers*, pp. 203–277, Springer, 1980.

[22] D. Ahn and K. R. Shull, "Jkr studies of acrylic elastomer adhesion to glassy polymer substrates," *Macromolecules*, vol. 29, no. 12, pp. 4381–4390, 1996.

[23] M. Deruelle, H. Hervet, G. Jandeau, and L. Leger, "Some remarks on jkr experiments," *Journal of adhesion science and technology*, vol. 12, no. 2, pp. 225–247, 1998.

[24] C. Creton and M. Ciccotti, "Fracture and adhesion of soft materials: a review," *Reports on Progress in Physics*, vol. 00, pp. 1–56, Oct 2015.

[25] P. P. Cortet, M. J. Dalbe, C. Guerra, C. Cohen, M. Ciccotti, S. Santucci, and L. Vanel, "Intermittent stick-slip dynamics during the peeling of an adhesive tape from a roller," *Physical Review E*, vol. 87, no. 022601, pp. 1–8, 2013.

[26] R. Villey, C. Creton, P.-P. Cortet, M.-J. Dalbe, T. Jet, B. Saintyves, S. Santucci, L. Vanel, D. J. Yarusso, and M. Ciccotti, "Rate-dependent elastic hysteresis during the peeling of pressure sensitive adhesives," *Soft Matter*, vol. 11, pp. 3480–3491, Jan 2015.

[27] A. Gent and J. Schultz, "Effect of wetting liquids on the strength of adhesion of viscoelastic material," *The Journal of Adhesion*, vol. 3, no. 4, pp. 281–294, 1972.

[28] E. Barthel and S. Roux, "Velocity-dependent adherence: an analytical approach for the jkr and dmt models," *Langmuir*, vol. 16, no. 21, pp. 8134–8138, 2000.

[29] R. S. Rivlin, "The effective work of adhesion," *Paint Technology*, vol. IX, no. 106, pp. 2611—2614, 1944.

[30] B. Roman and J. Bico, "Elasto-capillarity: deforming an elastic structure with a liquid droplet," *J. Phys.: Condens. Matter*, vol. 22, pp. 1–16, Nov 2010.

[31] A. C. Fischer-Cripps, "The hertzian contact surface," *Journal of Materials Science*, vol. 34, pp. 129–137, Jan 1999.

[32] H. R. Hertz, “Uber die beruhrung feste elastischer korper (on the contact of elastic bodies),” *J. reine und angewandte mathematiik*, vol. 92, pp. 156–171, 1882.

[33] K. R. Shull, “Contact mechanics and the adhesion of soft solids,” *Materials Science and Engineering R*, vol. 36, pp. 1–45, Jan 2002.

[34] E. Barthel, “Adhesive elastic contacts: Jkr and more,” *Journal of Physics D: Applied Physics*, vol. 41, no. 163001, 2008.

[35] R. S. Bradley, “The cohesive force between solid surfaces and the surface energy of solids,” *The London, Edinburgh, and Dublin Philosophical Magazine and Journal of Science*, vol. 13, no. 86, pp. 853–862, 1932.

[36] B. V. Derjaguin, V. M. Muller, and Y. P. Toporov, “Effect of contact deformations on the adhesion of particles,” *Progress in Surface Science*, vol. 53, pp. 314–326, Nov 1975.

[37] D. Tabor, “Surface forces and surface interactions,” *Journal of Colloid and Interface Science*, vol. 58, pp. 2–13, Jan 1977.

[38] D. Maugis, “Adhesion of spheres: The jkr-dmt transition using a dugdale model,” *Journal of Colloid and Interface Science*, vol. 150, pp. 243–269, Jul 1992.

[39] J. Greenwood, “Adhesion of elastic spheres,” in *Proceedings of the Royal Society of London A: Mathematical, Physical and Engineering Sciences*, vol. 453, pp. 1277–1297, The Royal Society, 1997.

[40] D. Dugdale, “Yielding of steel sheets containing slits,” *Journal of the Mechanics and Physics of Solids*, vol. 8, no. 2, pp. 100–104, 1960.

[41] D. Maugis, *Contact Adhesion and Rupture of Elastic Solids*. Springer, 2000.

[42] B. Bhushan, *Springer handbook of nanotechnology*. Springer Science & Business Media, 2010.

[43] F. P. Bowden and D. Tabor, *The friction and lubrication of solids*, vol. 2. Wiley Online Library, 1964.

[44] D. Nguyen, S. Ramakrishna, C. Fretigny, N. Spencer, Y. Le Chenadec, and A. Chateauminois, “Friction of rubber with surfaces patterned with rigid spherical asperities,” *Tribology Letters*, vol. 49, no. 1, pp. 135–144, 2013.

[45] M. Trejo, C. Fretigny, and A. Chateauminois, “Friction of viscoelastic elastomers with rough surfaces under torsional contact conditions,” *Phys. Rev. E*, vol. 88, p. 052401, Nov 2013.

[46] L. Bureau and L. Léger, “Sliding friction at a rubber/brush interface,” *Langmuir*, vol. 20, no. 11, pp. 4523–4529, 2004.

[47] K. A. Grosch, “The relation between the friction and visco-elastic properties of rubber,” in *Proceedings of the Royal Society of London A: Mathematical, Physical and Engineering Sciences*, vol. 274, pp. 21–39, The Royal Society, 1963.

[48] J. Greenwood and D. Tabor, "The friction of hard sliders on lubricated rubber: the importance of deformation losses," *Proceedings of the Physical Society*, vol. 71, no. 6, p. 989, 1958.

[49] D. T. Nguyen, P. Paolino, M. Audry, A. Chateauminois, C. Fretigny, Y. Le Chenadec, M. Portigliatti, and E. Barthel, "Surface pressure and shear stress fields within a frictional contact on rubber," *The Journal of Adhesion*, vol. 87, no. 3, pp. 235–250, 2011.

[50] D. T. Nguyen, E. Wandersman, A. Prevost, Y. Le Chenadec, C. Fretigny, and A. Chateauminois, "Non–amontons-coulomb local friction law of randomly rough contact interfaces with rubber," *EPL (Europhysics Letters)*, vol. 104, no. 6, p. 64001, 2013.

[51] B. min Zhang Newby and M. K. Chaudhury, "Effect of interfacial slippage on viscoelastic adhesion," *Langmuir*, vol. 13, pp. 1805–1809, Aug 1997.

[52] R. R. Collino, N. R. Philips, M. N. Rossol, R. M. McMeeking, and M. R. Begley, "Detachment of compliant films adhered to stiff substrates via van der waals interactions: role of frictional sliding during peeling," *J. R. Soc. Interface*, vol. 11, pp. 1–11, Jun 2014.

[53] A. Chateauminois and C. Fretigny, "Local friction at a sliding interface between an elastomer and a rigid spherical probe," *Eur. Phys. J. E*, vol. 27, pp. 221–227, Oct 2008.

[54] A. Chateauminois, C. Fretigny, and L. Olanier, "Friction and shear fracture of an adhesive contact under torsion," *Physical Review E*, vol. 81, no. 2, p. 026106, 2010.

[55] A. Schallamach, "A theory of dynamic rubber friction," *Wear*, vol. 6, no. 5, pp. 375–382, 1963.

[56] Y. B. Chernyak and A. Leonov, "On the theory of the adhesive friction of elastomers," *Wear*, vol. 108, no. 2, pp. 105–138, 1986.

[57] K. Vorvolakos and M. K. Chaudhury, "The effects of molecular weight and temperature on the kinetic friction of silicone rubbers," *Langmuir*, vol. 19, no. 17, pp. 6778–6787, 2003.

[58] D. H. Kaelble, "Theory and analysis of peel adhesion: Mechanisms and mechanics," *TRANSACTIONS OF THE SOCIETY OF RHEOLOGY*, vol. III, pp. 161–180, Feb 1959.

[59] M. R. Begley, R. R. Collino, J. N. Israelachvili, and R. M. McMeeking, "Peeling of a tape with large deformations and frictional sliding," *Journal of the Mechanics and Physics of Solids*, vol. 61, pp. 1265–1279, Jul 2013.

[60] M. D. Bartlett, A. B. Croll, D. R. King, B. M. Paret, D. J. Irschick, and A. J. Crosby, "Looking beyond fibrillar features to scale gecko-like adhesion," *Adv. Mater.*, vol. 24, no. 8, pp. 1078–1083, 2012.

[61] M. D. Bartlett, A. B. Croll, and A. J. Crosby, "Designing bio-inspired adhesives for shear loading: From simple structures to complex patterns," *Adv. Funct. Mater.*, pp. 1–8, 2012.

[62] D. H. Kaelble, "Theory and analysis of peel adhesion: Bond stresses and distributions," *TRANSACTIONS OF THE SOCIETY OF RHEOLOGY*, vol. IV, pp. 45–73, Feb 1960.

[63] A. N. Gent and S. Y. Kaang, "Effect of peel angle upon peel force," *The Journal of Adhesion*, vol. 24, pp. 173–181, Nov 1987.

[64] J. W. Obreimoff, “The splitting strength of mica,” *Proceedings of the Royal Society of London. Series A, Containing Papers of a Mathematical and Physical Character*, vol. 127, pp. 290–297, Dec 1930.

[65] A. Ghatak, L. Mahadevan, and M. K. Chaudhury, “Measuring the work of adhesion between a soft confined film and a flexible plate,” *Langmuir*, vol. 21, pp. 1277–1281, Apr 2005.

[66] G. Lake and A. Stevenson, “Wave phenomena in low angle peeling,” *Journal of Adhesion*, vol. 12, pp. 13–22, 1981.

[67] A. Schallamach, “How does rubber slide?,” *Wear*, vol. 17, pp. 301–312, Jun 1971.

[68] C. Rand and J. Crosby, “Insight into the periodicity of schallamach waves in soft material friction,” *Appl. Phys. Lett.*, vol. 89, p. 261907, 2006.

[69] M. Barquins, “Sliding friciton of rubber and schallamach waves - a review,” *Materials Science and Engineering*, vol. 73, pp. 45–63, Dec 1985.

[70] S.Ponce, B.Roman, J.Bico, and C.-Y. Hui, “Frictional peeling,” *in preparation*, 2015.

[71] A. Filippov, J. Klafter, and M. Urbakh, “Friction through dynamical formation and rupture of molecular bonds,” *Phys. Rev. Lett.*, vol. 92, p. 135503, 2004.

[72] E. Degrandi-Contraires, C. Poulard, F. Restagno, and L. Leger”, “Sliding friction at soft micropatterned elastomer interfaces,” *Faraday Discuss.*, vol. 156, pp. 255–265, 2012.

[73] C. Rand and A. Crosby, “Friction of soft elastomeric wrinkled surfaces,” *J. Appl. Phys.*, vol. 106, p. 064913, 2008.

[74] A. Jagota and C.-Y. Hui, “Adhesion, friction, and compliance of bio-mimetic and bio-inspired structured interfaces,” *Materials Science & Engineering R*, vol. 72, pp. 253–292, Dec 2011.

[75] E. Reissner, “Stresses and small displacements of shallow spherical shells. i,” *Journal Math. Phys. (Cambridge, Mass.)*, vol. 25, pp. 80–85, 1946.

[76] E. Reissner, “Stresses and small displacements of shallow spherical shells. ii,” *Journal Math. Phys. (Cambridge, Mass.)*, vol. 25, pp. 279–300, 1947.

[77] A. Lazarus, H. C. B. Florijn, and P. M. Reis, “Geometry-induced rigidity in nonspherical pressurized elastic shells,” *Physical Review Letters*, vol. 109, p. 144301, Oct 2012.

[78] C.-Y. Hui and R. Long, “Direct extraction of work of adhesion from contact experiments: Generalization of jkr theory to flexible structures and large deformation,” *The Journal of Adhesion*, vol. 88, pp. 70–85, Dec 2012.

[79] F. M. Borodich, B. A. Galanov, S. N. Gorb, M. Y. Prostov, Y. I. Prostov, and M. M. Suarez-Alvarez, “Evaluation of adhesive and elastic properties of polymers by the bg method,” *Macromol. React. Eng.*, vol. 7, pp. 555–563, Aug 2013.

[80] "Nonlinear finite elements/nonlinearities in solid mechanics: http://en.wikiversity.org/wiki/Nonlinear_finite_elements/Nonlinearities_in_solid_mechanics." Accessed: 2015-09-23.

[81] "Nonlinear structural analysis: http://mostreal.sk/html/guide_55/g-str/gstr8.htm." Accessed: 2015-09-23.

[82] R. Long, K. R. Shull, and C.-Y. Hui, "Large deformation adhesive contact mechanics of circular membranes with a flat rigid substrate," *Journal of the Mechanics and Physics of Solids*, vol. 58, pp. 1225–1242, Sep 2010.

[83] R. Long and C.-Y. Hui, "Axisymmetric membrane in adhesive contact with rigid substrates: Analytical solutions under large deformation," *International Journal of Solids and Structures*, vol. 49, pp. 672–683, Feb 2012.

[84] A. Pogorelov, *Bending of surfaces and stability of shells*. American Mathematical Society, 1988.

[85] L. Pauchard, Y. Pomeau, and S. Rica, "Déformation des coques élastiques," *C. R. Academie des Sciences de Paris*, vol. 324, no. Série II b, pp. 411–418, 1997.

[86] L. Pauchard and S. Rica, "Contact and compression of elastic spherical shells: the physics of a 'ping-pong' ball," *Philosophical Magazine B*, vol. 78, no. 2, pp. 225–233, 1998.

[87] A. Nasto, A. Ajdari, A. Lazarus, A. Vaziri, and P. M. Reis, "Localization of deformation in thin shells under indentation," *Soft Matter*, vol. 9, p. 6796, Jan 2013.

[88] A. Nasto and P. M. Reis, "Localized structures in indented shells: A numerical investigation," *Journal of Applied Mechanics*, vol. 81, p. 121008, Oct 2014.

[89] C.-Y. Hui, T. Liu, T. Salez, E. Raphael, and A. Jagota, "Indentation of a rigid sphere into an elastic substrate with surface tension and adhesion," *Proceedings of the Royal Society of London A*, vol. 471, pp. 1–24, Jan 2015.

[90] J. D. Lord and R. M. Morrell, "Elastic modulus measurement—obtaining reliable data from the tensile test," *Metrologia*, vol. 47, pp. S41—S49, Mar 2010.

[91] S. Ponce, J. Bico, and B. Roman, "Effect of friction on the peeling test at zero-degrees," *Soft Matter*, pp. –, Oct 2015.